

Processing and creep resistance of short SiC fiber containing Ti_3SiC_2 MAX phase composites

Apurv Dash

Energie & Umwelt / Energy & Environment

Band / Volume 543

ISBN 978-3-95806-558-1

Forschungszentrum Jülich GmbH
Institut für Energie- und Klimaforschung
Werkstoffsynthese und Herstellungsverfahren (IEK-1)

Processing and creep resistance of short SiC fiber containing Ti_3SiC_2 MAX phase composites

Apurv Dash

Schriften des Forschungszentrums Jülich
Reihe Energie & Umwelt / Energy & Environment

Band / Volume 543

ISSN 1866-1793

ISBN 978-3-95806-558-1

Bibliografische Information der Deutschen Nationalbibliothek.
Die Deutsche Nationalbibliothek verzeichnet diese Publikation in der
Deutschen Nationalbibliografie; detaillierte Bibliografische Daten
sind im Internet über <http://dnb.d-nb.de> abrufbar.

Herausgeber
und Vertrieb: Forschungszentrum Jülich GmbH
Zentralbibliothek, Verlag
52425 Jülich
Tel.: +49 2461 61-5368
Fax: +49 2461 61-6103
zb-publikation@fz-juelich.de
www.fz-juelich.de/zb

Umschlaggestaltung: Grafische Medien, Forschungszentrum Jülich GmbH

Titelbild: Die falsch eingefärbte rasterelektronenmikroskopische Aufnahme zeigt die Bruchfläche von Ti_3SiC_2 MAX/SiC-Whisker-Verbundmaterial. Das Bild unterstreicht die perfekte Ablösung der Whisker, die einkristalline SiC-Hexagonalprismen sind von der Ti_3SiC_2 -Matrix. Das Schliffbild hebt auch die Delamination der MAX-Schichten hervor, die die Bruchspannung absorbieren. Das Schliffbild wurde von Dr. Doris Sebold aufgenommen und von Herrn Apurv Dash koloriert.

Druck: Grafische Medien, Forschungszentrum Jülich GmbH

Copyright: Forschungszentrum Jülich 2021

Schriften des Forschungszentrums Jülich
Reihe Energie & Umwelt / Energy & Environment, Band / Volume 543

D 82 (Diss. RWTH Aachen University, 2020)

ISSN 1866-1793
ISBN 978-3-95806-558-1

Vollständig frei verfügbar über das Publikationsportal des Forschungszentrums Jülich (JuSER)
unter www.fz-juelich.de/zb/openaccess.



This is an Open Access publication distributed under the terms of the [Creative Commons Attribution License 4.0](https://creativecommons.org/licenses/by/4.0/), which permits unrestricted use, distribution, and reproduction in any medium, provided the original work is properly cited.

CONTENTS

Abstract	iii
Zusammenfassung	v
Acknowledgements	vii
1 Introduction	1
1.1 History of materials	1
1.2 MAX phases.	2
1.3 Ti_3SiC_2 MAX phase	4
1.4 Mechanical properties of MAX phases	5
1.5 The need for a composite material	8
References	13
2 State of the art	17
2.1 Synthesis of Ti_3SiC_2 MAX phase.	17
2.2 Molten salt assisted synthesis of MAX phases	20
2.3 Composites with Ti_3SiC_2 as the matrix	21
2.3.1 Particle reinforced ceramic matrix composites.	21
2.3.2 Fiber reinforced ceramic matrix composites	22
2.4 Mechanical properties of MAX phases	22
2.4.1 Room temperature mechanical properties.	22
2.4.2 High temperature mechanical properties	23
2.4.3 High temperature creep of MAX phases	23
References	24
3 Materials & Methods	29
3.1 Synthesis of MAX phase powders	29
3.2 Powder characterization	30
3.3 Ti_3SiC_2 based ceramic matrix composite (CMCs)	32
3.4 High temperature compressive creep	33
4 Result & discussion I: Molten salt shielded synthesis (MS^3) of Ti_3SiC_2	35
4.1 Molten salt shielded synthesis (MS^3) process	35
4.2 Reaction mechanism for the formation of Ti_3SiC_2 in molten salt	40
4.3 Interfacial investigation of $\text{KBr-Ti}_3\text{SiC}_2$ with and without Al.	50
4.4 Milling study of synthesized Ti_3SiC_2	52
4.5 Synthesis of other non-oxide ceramic powders	54
4.6 Sintering of Ti by MS^3 process.	58
References	60

5	Result & discussion II: Processing of Ti_3SiC_2 composites containing SiC whiskers and short SiC fibers	67
5.1	Characterization of spark plasma sintered monolithic Ti_3SiC_2	68
5.2	Grain growth of textured Ti_3SiC_2 and its characterization	77
5.3	Characterization of spark plasma sintered short SiC_f / Ti_3SiC_2 composites	81
5.4	Characterization of spark plasma sintered SiC_w / Ti_3SiC_2 composites.	85
	References	89
6	Result & discussion III: Compressive creep resistance of short SiC fiber / Ti_3SiC_2 composites	91
6.1	Creep of textured Ti_3SiC_2	92
6.1.1	Steady state creep of fine grained textured Ti_3SiC_2	92
6.1.2	Steady state creep of coarse grained textured Ti_3SiC_2	93
6.1.3	Creep activation energy and stress exponent.	95
6.1.4	Post creep microstructural investigation	97
6.2	Creep of short SiC_f / Ti_3SiC_2 composites	99
6.2.1	Steady state creep of fine grained SiC_f / Ti_3SiC_2 CMC	99
6.2.2	Creep activation energy and stress exponent.	102
6.2.3	Post creep microstructural investigation	103
6.3	Creep of SiC_w / Ti_3SiC_2 composites	105
6.3.1	Steady state creep of fine grained SiC_w / Ti_3SiC_2 CMC	105
6.3.2	Creep activation energy and stress exponent.	108
6.3.3	Post creep microstructural investigation	110
6.4	Summary of different reinforcements on the creep of Ti_3SiC_2	114
	References	116
7	Conclusion	119
	Curriculum Vitae	123
	List of Publications	125

ABSTRACT

Alternative materials for high temperature applications might offer a solution to higher efficiency and low fuel consumption for jet engines. A possible candidate for such material is Ti_3SiC_2 which is a ceramic material with unique combination of mechanical properties at high temperature. Ceramics are brittle in nature and have a typically low Weibull modulus as compared to metals. Hence, monolithic ceramic parts cannot directly replace metal parts due to the lack of reliability. Ceramic matrix composites (CMCs) with bulk ceramic material as the matrix and a ceramic fiber as the reinforcement offers the possibility to have high strength at high temperature but present some limitations like high costs and very few applications despite the huge economical efforts in the last decade. The complex processing routes followed for the fabrication of CMC have limited the applications.

The present work is about the fabrication of a CMC with Ti_3SiC_2 as the matrix and short SiC fiber as the reinforcement material. Ti_3SiC_2 is a special ceramic material which is machinable at room temperature and has a certain degree of plasticity at high temperature ($\sim 1200^\circ\text{C}$). A novel molten salt-based process was developed to synthesize high purity Ti_3SiC_2 at a large scale (1kg/batch) in air. The method involved mixing of elemental precursor with KBr salt and high temperature treatment at 1250°C to obtain the desired Ti_3SiC_2 phase. Al was added to the reaction mixture to enhance the purity of Ti_3SiC_2 . The effect of different levels of Al addition on the evolution of the Ti_3SiC_2 phase was studied. The synthesis process itself was studied to understand the barrier of oxidation to the oxidation prone materials. Apart from Ti_3SiC_2 , a wide range of non-oxide ceramics like TiC, Ti_2AlC , Ti_3AlC_2 , Cr_2AlC , Ti_2AlN , MoAlB and many more were synthesized for the proof of concept. Metals like titanium were also sintered in dense and porous forms using the same process in air. The method was referred to as Molten Salt Shielded Synthesis/Sintering (MS^3). MS^3 process resulted in a reduction of the synthesis temperature of Ti_3SiC_2 along with other non-oxide ceramics. MS^3 process can be carried out in air without the need of expensive atmosphere-controlled furnaces. The dissolution of salt after MS^3 process results in micro-metric agglomerated powder which does not need to be milled unlike conventional solid-state reactions.

The synthesized Ti_3SiC_2 powder was sintered in spark plasma sintering (SPS) furnace at 1250°C with a uniaxial pressure of 80 MPa. Similarly, CMCs were also sintered in SPS by following a powder metallurgical process to mix the reinforcement with the synthesized Ti_3SiC_2 powder. The reinforcement of Ti_3SiC_2 was done in macroscale and microscale. The macroscale reinforcement was done by adding 10 and 20 vol.% chopped polycrystalline SiC fibers (1 mm) whereas the microscale reinforcement was done by adding 10 and 20 vol.% of single crystalline SiC whiskers.

The monolithic Ti_3SiC_2 had a prominent basal texture after sintering and so did the CMCs. Characterization were done to determine the degree of orientation of Ti_3SiC_2 crystals in the sintered material. The sintered Ti_3SiC_2 was annealed at 1500°C to induce

grain growth in an already textured Ti_3SiC_2 material. The alignment of SiC fibers and whiskers were also determined and were found to be dependent with respect to the direction of the application of the external pressure during sintering.

The sintered monolithic Ti_3SiC_2 and the composites were subjected to high temperature compressive creep in the temperature and stress range of 1000-1300 °C and 20-120 MPa respectively. As the sintered Ti_3SiC_2 was textured, the creep was measured in two different configurations with different crystallographic orientation with respect to the compression direction. Similar creep measurements were performed on the Ti_3SiC_2 composites with SiC fibers and whiskers. The specimens with coarse grains due to a high temperature annealing were also tested for high temperature compressive creep. Post-creep characterizations were done by SEM, EBSD and TEM to understand the deformation mechanisms along with the activation energy and stress exponent values obtained experimentally.

ZUSAMMENFASSUNG

Neuartige Werkstoffe für Hochtemperaturanwendungen könnten eine Verbesserung der Effizienz und einen niedrigeren Treibstoffverbrauch von Düsentriebwerken ermöglichen. Ein aussichtsreicher Kandidat hierfür ist Ti_3SiC_2 , ein keramisches Material mit einer einzigartigen Kombination von mechanischen Eigenschaften bei hohen Temperaturen. Keramiken sind von Natur aus spröde und haben im Vergleich zu Metallen einen niedrigen Weibull-Modul. Daher können monolithische Keramikteile aufgrund der mangelnden Zuverlässigkeit Metallteile nicht direkt ersetzen. Keramik-Matrix-Verbundwerkstoffe (CMCs) mit keramischer Matrix und einer Keramikfaser als Verstärkung bieten die Möglichkeit, eine hohe Festigkeit bei hohen Temperaturen zu erreichen. Sie weisen aber trotz der enormen wirtschaftlichen Anstrengungen in den letzten Jahrzehnten einige Einschränkungen wie hohe Kosten und sehr wenige Anwendungen auf. Die komplexen Herstellungsrouten, welche für die Synthese und Verarbeitung von CMCs nötig sind, haben eine breite Anwendung verhindert.

Die vorliegende Arbeit befasst sich mit der Herstellung von CMC Werkstoffen auf der Basis einer Ti_3SiC_2 -Matrix und kurzen SiC-Fasern als Verstärkungsmaterial. Ti_3SiC_2 ist ein spezieller keramischer Werkstoff, der bei Raumtemperatur mechanisch bearbeitbar ist und bei hoher Temperatur ($\sim 1200\text{ }^\circ\text{C}$) eine gewisse Plastizität aufweist. Es wurde ein neuartiges, auf Salzschnmelzen basierendes Verfahren entwickelt, um hochreines Ti_3SiC_2 in großem Maßstab (1kg/Batch) an Luft zu synthetisieren. Das Verfahren beinhaltet das Mischen der elementaren Ausgangsstoffe mit KBr-Salz und eine Hochtemperaturbehandlung bei $1250\text{ }^\circ\text{C}$, um die gewünschte Ti_3SiC_2 -Phase zu erhalten. Aluminium wurde der Reaktionszusatz hinzugefügt, um die Reinheit von Ti_3SiC_2 zu erhöhen. Die Auswirkung unterschiedlicher Mengen an Al-Zugabe auf die Entwicklung der Ti_3SiC_2 -Phase wurde untersucht. Der Syntheseprozess selbst wurde eingehend charakterisiert, um die Funktion der Oxidationsbarriere für die oxidationsanfälligen Materialien zu verstehen. Abgesehen von Ti_3SiC_2 wurde eine breite Palette von Nichtoxid-Keramiken wie TiC, Ti_2AlC , Ti_3AlC_2 , Cr_2AlC , Ti_2AlN , MoAlB und viele andere für den Proof-of-Concept dieses Verfahrens synthetisiert. Auch Metalle wie Titan wurden in dichter und poröser Form nach dem gleichen Verfahren an Luft gesintert. Das Verfahren wurde als Abgeschirmte Salzschnmelzesynthese bzw. Sintern (MS^3) bezeichnet. Das MS^3 -Verfahren führt zu einer Senkung der Synthesetemperatur von Ti_3SiC_2 und anderen Nichtoxidkeramiken. Zusätzlich kann der MS^3 -Prozess an Luft durchgeführt werden, ohne dass teure Inertgas-Öfen erforderlich sind. Die Lösung des zugemischten Salzes nach dem MS^3 -Prozess führt zu leicht agglomerierten Pulvern im Mikrometermaßstab, welche im Gegensatz zu herkömmlichen über Festkörperreaktionen hergestellten Pulvern nicht gemahlen werden müssen.

Das synthetisierte Ti_3SiC_2 -Pulver wurde in einem FAST/SPS-System (Field assisted sintering/Spark Plasma Sintering) bei $1250\text{ }^\circ\text{C}$ mit einem uniaxialen Druck von 80 MPa gesintert. In ähnlicher Weise wurden auch CMCs im FAST/SPS-System gesintert, indem die

Verstärkungsphase mit Hilfe eines pulvermetallurgischen Prozesses mit dem Ti_3SiC_2 -Pulver gemischt wurde. Die Verstärkung von Ti_3SiC_2 erfolgte im Makro- und Mikromaßstab. Im Makromaßstab erfolgte die Verstärkung durch Hinzufügen von 10 und 20 Vol.-% polykristalliner SiC-Fasern (1 mm), während die Verstärkung im Mikromaßstab durch Hinzufügen von 10 und 20 Vol. % einkristalliner SiC-Whisker erfolgte.

Monolithisches Ti_3SiC_2 zeigte nach dem Sintern eine ausgeprägte Basaltstruktur, ebenso wie die hergestellten CMCs. Die Charakterisierung wurde durchgeführt, um den Orientierungsgrad der Ti_3SiC_2 -Kristalle im gesinterten Material zu bestimmen. Das gesinterte Ti_3SiC_2 wurde bei 1500 °C geglüht, um Kornwachstum in dem bereits texturierten Ti_3SiC_2 -Werkstoff zu induzieren. Zusätzlich wurde die Ausrichtung der SiC-Fasern und Whiskern bestimmt und es wurde festgestellt, dass diese stark von der Aufbringung des uniaxialen Drucks während des Sinterns abhängen.

Das gesinterte monolithische Ti_3SiC_2 und die daraus hergestellten Verbundwerkstoffe wurden Kompressionskriechtests bei hohen Temperaturen im Temperatur- und Spannungsbereich von 1000-1300 °C bzw. 20-120 MPa ausgesetzt. Da das gesinterte Ti_3SiC_2 texturiert war, wurde das Kriechen in zwei verschiedenen Ausrichtungen mit unterschiedlicher kristallographischer Orientierung in Bezug auf die Druckrichtung gemessen. Ähnliche Kriechmessungen wurden an Ti_3SiC_2 -Verbundwerkstoffen mit SiC-Fasern und Whiskern durchgeführt. Zusätzlich wurden durch eine Wärmebehandlung künstlich vergrößerte Proben auf ihre Kriecheigenschaften unter uniaxialem Druck bei hoher Temperatur untersucht. Die Charakterisierung der Proben nach den Kriechexperimenten wurden mittels REM, EBSD und TEM durchgeführt, um die Verformungsmechanismen, die Aktivierungsenergie sowie die experimentell erhaltenen Spannungsexponenten zu diskutieren.

ACKNOWLEDGEMENTS

This work is a confluence of the efforts of many experts. It wouldn't have been possible if not for Prof. Jesus Gonzalez-Julian who was both a mentor and a friend in the three years journey of seeking something new and groundbreaking. We shared the ecstasies of unthinkable results.

I am grateful to Prof. Olivier Guillon to support me in all my unconventional endeavors. His open mindedness led to the exploration of many scientific extra-curricular activities apart from the PhD work frame. I would like to extend my gratitude to Prof. Robert Vaßen for his support. Dr. Jürgen Malzbender was the key person for studying the mechanics of Ti_3SiC_2 based composites, his support led the thesis to the present mode of perfection.

I would like to take the pleasure of thanking Dr. Egbert Wessel, Dr. Doris Sebold, Dr. Beatrix Göths and Dr. Marcin Rasinski for carrying out microscopy investigations on my specimens. I shared a mutual inquisitiveness with Mr. Volker Bader for the new synthesis method described in this thesis, his support for operating the furnaces led to uncountable heating cycles which resulted in ingenious findings. My sincere thanks to Mr. Marcel Turiaux for his help in creep measurements, he was pivotal to the high temperature mechanics of my specimen. Dr. Yoo Jung Sohn made the texture analysis of sintered Ti_3SiC_2 possible, I am indebted to her efforts.

My parents Mr. Laxmi Prasad Dash and Mrs. Swadhini Dash nurtured me and provided the emotional support to carry out research several thousand kilometers away from family. They strive not just to make me an outstanding scientist but a good human being as well. Words cannot describe my gratitude for them. I am thankful to my sister Dr. Khushbu Dash and my brother-in-law Prof. Nachiketa Mishra for the motivational dialogues we shared in moments of elation and apathy. I would like to thank Miss Magda Zygmontowska for being my family away from home and stand by my side throughout. I express my deep sense of gratitude to all the individuals whom I couldn't name and helped in the realization of this thesis. All inaccuracies and limitations in this thesis are mine and only mine.

*Apurv Dash
Jülich, June 2021*

1

INTRODUCTION

1.1. HISTORY OF MATERIALS

MATERIALS make the world we live in and the development of materials have led to the evolution of the human civilization and the advent of modern technology. After the stone age in the history of mankind, copper was the first metal to be discovered and used.[1] Similarly, the first man-made ceramic dates back to 28,000 BC and is a statuette of a woman named the Venus of Dolní Věstonice near Brno in Czech republic.[2] Mixing clay with water and firing was the earliest ceramic realized by humans. The same goes with the invention of the first polymer to replace ivory billiard balls with a substitute made from cotton fiber cellulose treated with camphor.[3] It was very soon that all the materials in this world were categorized into three major categories according to the chemical bonding and compositions: 1. Metals, 2. Ceramics and glass, 3. Polymers. A combination of two or more materials from the major categories are broadly referred to as composite materials. The usage of straw and mud together was done to make bricks to build walls is an example of such composite material used in the Mesopotamian civilization. These first materials were the foundation for ages of development in the material science, which certainly has supported our necessities during the human civilization. Currently, our society is facing other problems such as climate change, energy demand or equality. These problems have to be tackled from different directions, but clearly material science will play a big role with the development of new materials. The current limitation of high temperature materials is restricted by the operating temperature and the price. Hence there is a need for the development of economical composite materials with better mechanical properties which can operate at a higher temperature in aggressive environment and overcome the limitation of existing materials which melts at the aimed higher operating temperatures.

Some properties of materials in each category were believed to be exclusive. For eg. Metals are ductile and soft whereas ceramics are brittle and hard. There was no material which had a combination of properties of both metals and ceramics. The merger of machinability, damage tolerance, thermal and electrical conductivity of metal and chemical resistance with high temperature stability of ceramics was only realized after

the discovery of a special class of materials called as MAX phase.[4] MAX phase are an intriguing class of materials which are recently being discovered and intermediate of metals and ceramics.[5]

1.2. MAX PHASES

The terminology MAX refers to an empirical formula $M_{n+1}AX_n$ where “M” corresponds to an early transition element (group IIIB-VIB), “A” refers to the elements highlighted in the periodic table from group IIIA-VIA, “X” refers to either C or N or both, and n is to the number of M layers separating the A layers.

MAX phases have a hexagonal crystallography with the space group P63-mmc. Con-

$M_{n+1}AX_n$

Figure 1.1: Elements of the periodic table constituting MAX phase.

sidering the generic formula of $M_{n+1}AX_n$ n can vary between 1-3. The crystal structure constitutes of n layers of M_6X octahedra separated by one layer of A atoms. For example in Ti_2AlC there are two layers of Ti separating Al layers. Similarly, for Ti_3SiC_2 there are three layers of Ti separating the Si layer. Fig 1.1 shows the elements in the periodic table which can form a ternary carbide or nitride.

Since the beginning of research on MAX phase materials, there are up to more than 80 MAX phases synthesized. For e.g. Ti_2AlC , Cr_2AlC , Ti_2AlN which corresponds to the value of n as 1 in the empirical formula mentioned earlier. Similarly, Ti_3SiC_2 is one of the examples for $n=2$ and Nb_4AlC_3 for $n=3$. There are other MAX phases synthesized which contain more than 3 elements by forming a solid solution of the M, A or X element. $(Nb_xZr_{1-x})_4AlC_3$ and $(Cr_{2/3}Zr_{1/3})_2AlC$ are examples of solid solution in the M position, the properties of such MAX phases can be tuned and tailored.[6, 7] $Ti_2Al_{1-x}Sn_xC$ is a MAX phase with solid solution in A position and $Ti_2AlN_{0.5}C_{0.5}$ for X position.[8, 9] Double solid solutions like $(Zr,Nb)_2(Al,Sn)C$ are also synthesized and stabilized due to increase in the entropy of the system.[10] Ti_3SiC_2 is one of the first MAX phases synthesized and is widely studied for its thermal and mechanical properties.[11–13]

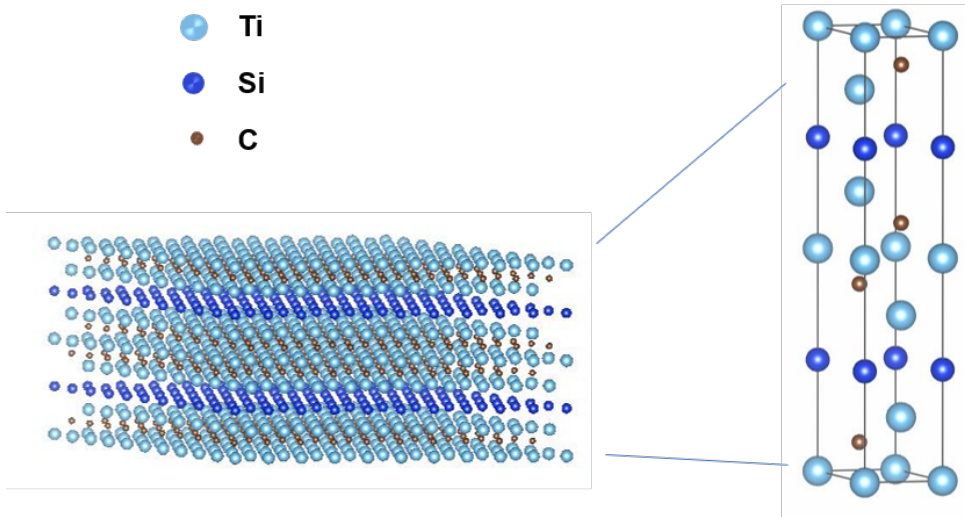


Figure 1.2: Atomic structure of Ti₃SiC₂ MAX phase, on the right is a single unit cell of Ti₃SiC₂.

The history of MAX phases dates to 1964 when Jeitschko et al. first synthesized the M₂AX type of ternary carbide followed by the synthesis of Ti₃SiC₂ in 1966.[14] The ternary carbides were referred to as Hägg phase or simply H-phase.[15, 16] The technological importance of these ternary carbides/nitrides were not realized until Michel W. Barsoum and his co-workers in Drexel University published the first paper on the synthesis of bulk Ti₃SiC₂. [17] It was demonstrated that it can be machined by turning. This marked the beginning of exploration of other MAX phases having a different chemistry with varied combination of properties like oxidation resistance, flexural strength and creep resistance.[11, 18–22] The uniqueness of MAX phase materials of being a ceramic and yet machinable comes from the fact that the material is nano-laminated with weak M-A bonds as compared to M-X bonds.[4] The damage tolerance and machinability of MAX phase materials are due to the presence of mobile dislocations along basal planes and formation of kink bands under stresses.[12, 23] MAX phases are also softer (3-4 GPa) than the corresponding binary carbide/nitride (MX, 15-20 GPa).[5] The unusual combination of properties like excellent machinability and good mechanical properties at high temperature (>1000 °C) can be correlated to the layered structure of MAX phases irrespective of the chemical composition.[23–26] Among all the different compositions, Ti₃SiC₂ has attracted a lot of attention due to their excellent mechanical response.

MAX phases, although having a combination of unique properties and attracting a lot of attention in the material science community, is difficult to synthesize. For scientific investigations which need low quantities – for example in the range of grams - the synthesis can be feasibly carried out in a lab scale, whereas for the manufacturing of a component would need a large quantity of MAX phase powder (at least kilograms). The commercial supplier of MAX phase powder is Sandvik® and provides Ti₃SiC₂ powder with the brand name of MAXthal 312. The drawback of this commercial powder is that it is only 80 wt.% phase pure and the final properties, particularly at high temperature, are detrimentally

controlled by the secondary phases.

Although a lot of research has been done in understanding the properties of Ti_3SiC_2 , the industrial application is limited because of the difficulty to produce phase pure powder in a large scale in an economic way. Despite Ti_3SiC_2 has excellent properties, the main bottle-neck is the availability of large-scale high purity powders. Currently MAX phase is synthesized by the reaction of elemental powders or compounds which has the elements required for the synthesis of the specific MAX phase. For eg. Ti_3SiC_2 can be synthesized by heat treating Ti, Si and C powder together or a mix of Ti, SiC and C. [12, 17] The aspects concerning the quality of ceramic powders are (i) phase purity and particle size of the targeted compound, (ii) scalability of powder production, the synthesis process should be easily up-scalable to obtain higher quantities of powder in one batch, (iii) the process should be economical considering the initial precursors used for the synthesis and the equipment used for the synthesis process, (iv) finally the synthesis process should be sustainable, reliable and, if possible, environment friendly. It is difficult to reach an ideal condition where all the criteria are met hence there is a continuous effort to a near ideal situation to have a high-quality ceramic powder for further ceramic processing.

Heating mixed elemental powder at high temperature (>1000 °C) is referred to as solid-state synthesis and usually results in a dense or porous block of the reacted product, which needs to be pulverized into fine powder for powder metallurgical operations. Co-munition of the dense MAX phase blocks possesses the problem of contamination of powder due to the abrasion resistance and hardness of ceramic media which leads to high wear and operating costs as well. In the present work, a molten salt-based process is developed for synthesizing Ti_3SiC_2 MAX phase in air at a relatively low temperature without the need of pulverization. The process, “Molten Salt Shielded Synthesis/Sintering”, is referred to by the acronym MS³. [27] Chapter 4 will throw more light on the process in detail. The reaction mechanism leading to the formation of Ti_3SiC_2 and the general applicability of the MS³ process for the synthesis of other MAX phases is also discussed in Chapter 4.

1.3. Ti_3SiC_2 MAX PHASE

Ti_3SiC_2 was one of the earliest MAX phases realized and hence it was investigated exhaustively. Although Ti_3SiC_2 started the era of MAX phases it was later realized that fine grained (3-5 μm) Ti_3SiC_2 has among the highest flexural strength (600 MPa) and density (4.55 g/cc) among the whole MAX phase family of materials. [28] It would not be inaccurate to say that Ti_3SiC_2 is one of the technologically important MAX phase in terms of mechanical properties as compared to other MAX phases. Ti_3SiC_2 also has a high temperature stability and does not decompose unlike other MAX phases. This makes Ti_3SiC_2 a potential candidate for high temperature load bearing applications. The physical properties of Ti_3SiC_2 including the mechanical properties are listed in Table 1.1.

The crystal structure of Ti_3SiC_2 is depicted in Fig.1.2. The Ti_3C octahedras are edge sharing and interleaved with layers of Si atoms. There are two types of Ti atoms present in the crystal structure, one which is bonded to C and the other which is bonded to Si. The cleavage energy of Ti-Si bond is lower than that of Ti-C hence the possibility of Ti-Si

Table 1.1: Physical properties of Ti_3SiC_2

Physical properties	Value
Elastic modulus	343 GPa [29]
Hardness	4-6 GPa [30, 31]
Flexural strength	300-600 MPa [17, 32]
Compressive strength	720-1050 MPa [28]
Tensile strength	200-300 MPa [33]
Fracture toughness	6-16 MPa.m ^{1/2} [34, 35]
Electrical resistivity	0.23 x 10 ⁻⁶ Ω.m [36]
Thermal conductivity	37 W m ⁻¹ .K ⁻¹ [13]
Coefficient of thermal expansion	9.1 x 10 ⁻⁶ K ⁻¹ [13]

breakage is higher.[37] The cleavage of Ti_3SiC_2 crystals are known to propagate in a direction parallel to the basal plane. The fracture toughness of Ti_3SiC_2 had been measured by various techniques including single-edge notched beam, chevron notched beam and compact tension methods. The fracture toughness (K_{IC}) of Ti_3SiC_2 is reported to lie between 6-16 MPa. \sqrt{m} . [34, 35] It was shown that coarse grained Ti_3SiC_2 yields a higher K_{IC} than the fine grain counterparts. [35] Ti_3SiC_2 also follows R-curve behavior which states that the material has an increasing K_{IC} with increasing crack length. [38]

1.4. MECHANICAL PROPERTIES OF MAX PHASES

The unique mechanical properties can be explained by different phenomena which might be responsible for the pseudo-ductility and toughening of the MAX phases in general. Although a polycrystalline material's response to deformation hugely depends on the grain size and the strain rate, the response of MAX phase is far simpler because instead of the formation of dislocation pile-up, twinning, work hardening or multiple kind of slips there is kinking of grains to dissipate the mechanical energy and only basal slip with dislocations travelling only in the basal plane. There is not the presence of five independent slip systems which is a pre-requisite for ductility. [5] The pseudo-ductility in MAX phases can be related to the formation of kink bands (KB), delamination of individual grains, formation of incipient kink bands (IKB) which can be fully recovered and shear band formation. [32, 39–43] When materials are subjected to stresses (tensile/compressive), the material tries to absorb the mechanical stress by deformation. For a multilayered material like MAX phase, if the strain rate is slow enough, the deformation takes place by the formation of folds of the layers transverse to the direction of the stress.

Fig.1.3 shows a schematic of the formation of kink band when a MAX phase crystal is subjected to stress with its basal plane parallel to the applied stress. The red ellipse refers to the formation of IKB when a certain stress is applied on a grain with the basal plane aligned with the axis of the applied stress. The initial bending of the grain results in a shear stress which when exceeds a certain critical value results in the formation of KB with dislocations of opposite signs moving apart from each other. The grain rotation in the KB region is so severe that it behaves as a separate grain with a different orientation

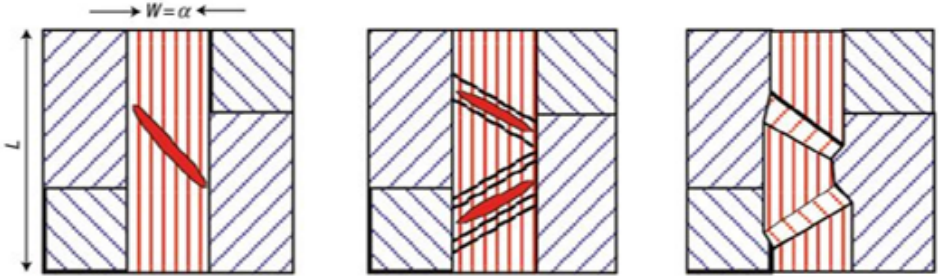


Figure 1.3: Schematic of the formation of incipient kink band to the formation of kink band after removal of stress.[43]

sandwiched by grains of same orientation. The grain boundaries of the kinked region are referred to as kink boundary. A cross-section of the kinked grain might create an illusion of three grains present but, the grain is continuous with a kink band region separated by kink boundaries which can be mistaken for grain boundaries. Being precise, the region between the two kink boundaries is known as a kink band.

Fig.1.4 shows a typical representation of a kink boundary. Orowan suggested that such

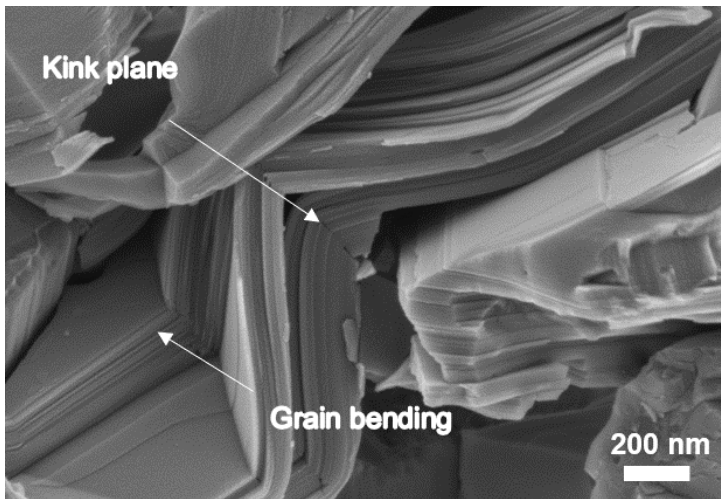


Figure 1.4: Kink boundary in Ti_3SiC_2 after deformation during compressive creep at 1300 °C.

kink planes contain excess of a single type of dislocations which can accommodate the strain.[44] It is this kind of phenomenon which makes MAX phase damage tolerant both at room and high temperature. Fig.1.5 shows an example of multiple kinking in one single grain of Ti_3SiC_2 .

Incipient kink band (IKB) are dislocations separated from each other which do not form separate mobile dislocation walls (MDWs), it is more of a metastable kink band which only exist under a certain load and disappears or recovers with the withdrawal of the

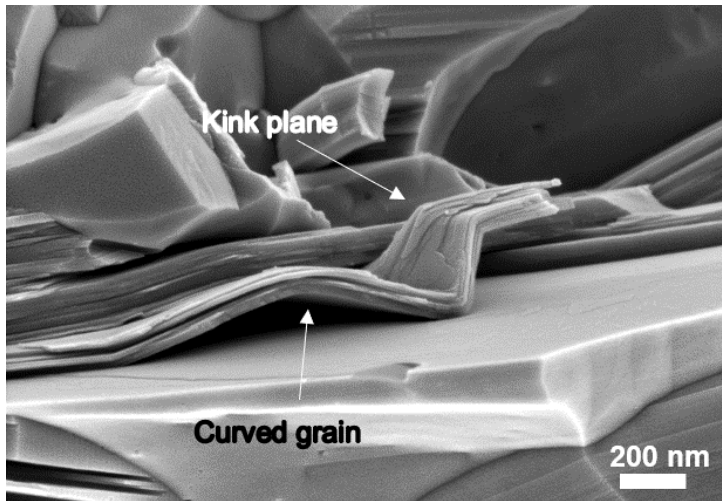


Figure 1.5: MAX phase snake of Ti_3SiC_2 layers with multiple kinks due to deformation.

load. In layered solids like MAX phase, IKB are responsible for the elastic deformation which is a completely reversible deformation. There are experimental evidences shown by Barsoum et al. where Ti_3SiC_2 fully recovers after the removal of a compressive stress of 1 GPa. The stress strain-hysteresis loops were closed at room temperature whereas open at high temperature.[43]

During the application of stress along a uniaxial axis, there are components of the stress which acts at an angle greater than 0 and less than 45 degrees more commonly known as shear stress. If the magnitude of the shear stress exceeds the value of critical resolved shear stress (CRSS) there is a shear of the MAX phase grain induced in a direction parallel to the basal plane. It depends on the grain size on how easy the shear band formation will take place because large grains are more prone to shear, and the inter-granular friction is lower in coarse grained MAX phase. Fig.1.6 shows the formation of shear bands which are parallel to each other. The formation of shear bands is easy at higher temperature since the CRSS reduces at higher temperatures.[29]

MAX phases also have a high fracture toughness as compared to other conventional ceramics. The factors contributing to the high toughness of MAX phases are multilayered nature of the material and partial metallic nature of the chemical bonds. Since the material is multilayered, crack propagates in a torturous path being deviated by the interfaces of the nano-laminates. The delamination of individual grains also aids in blunting the crack tip stress field. It is not a single factor which can be attributed for the unusual toughness and machinability of MAX phases because there are other layered materials like h-BN, MoS_2 and graphite which do not demonstrate the same combination of properties as MAX phase does.

The mechanical response of MAX phases at high temperature becomes complex because of brittle to plastic transition (BPT).[12] It was pointed out by Barsoum et al. that the increase in temperature does not result in the activation of extra slip systems, hence

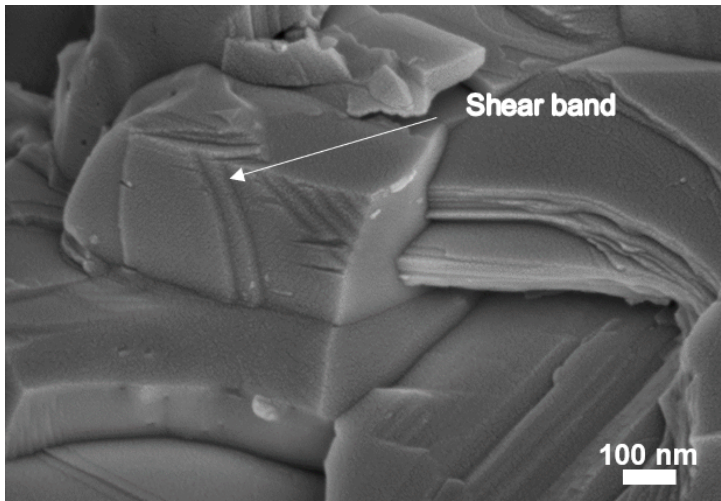


Figure 1.6: Shear band formation in Ti_3SiC_2 after uniaxial compression at 1300 °C and 80 MPa.

it is more appropriate to refer the transition as plastic and not ductile.[45] This was supported by demonstrating the reduction of K_{IC} with increasing temperature. The high temperature deformation is simply related to the rate of creation of internal stresses and the rate of annihilation of the internal stress. If the latter is higher or equal than the former, the deformation is plastic, in any other case the failure is brittle. The BPT is believed to be due to the softening of grain boundaries and the ease of grain delamination due to reduction in the surface energy of cleavage planes.[29]

The high temperature creep of MAX phase is unique with respect to the grain size and its corresponding creep resistance. Unlike metals and other conventional ceramics, MAX phases have higher creep resistance with finer grain size. Large grains tend to have higher tendency for delamination.[24] The main creep mechanism of Ti_3SiC_2 MAX phase is believed to be dislocation creep whereas for Ti_2AlC it is a combination of dislocation creep and grain boundary sliding.[18] Zhen et al. suggested that under high stress, the dislocation creep may have changed to sub-critical crack growth.[24] Although coarse microstructure has low creep resistance, it has a higher strain to failure as compared to the finer microstructure. It is also a function of how the load was applied (compressive/tension) which decides the mode of failure and whether the material fails by the formation of shear bands or linking of micro-cracks together.[24–26]

1.5. THE NEED FOR A COMPOSITE MATERIAL

We are in continuous look-out for better materials which can be a replacement for the currently used materials but with better properties and a better performance. In the initial stage of a material development the price of producing the material is not the foremost factor which is considered. Rather, the focus is more on what benefits the new material will provide as compared to the existing material in service. Since MAX phase is the

context, applications involving stresses at high temperature are considered as a possibility. The materials used in the jet engines have a requirement to maintain their structural integrity in harsh environmental conditions at high temperature with centrifugal force acting on the components. Currently, the jet engines use Ni based super-alloy which is considered as a standard material. The operation of an engine is always associated with the efficiency it runs with. The efficiency of an engine increases with the increment of the operating temperature and can be best described by Brayton cycle. Although the efficiency is given by the ratio of the difference in temperatures at isobaric and iso-entropic states, the ideal efficiency can be defined by:

$$\eta = 1 - \frac{T_a}{T_e} \quad (1.1)$$

where η is the theoretical efficiency, T_a is the atmospheric temperature and T_e is the compressor exit temperature of the engine.[46] But the maximum operating temperature of an engine is limited by the material properties. For e.g. the creep resistance of the turbine blades at high temperature. Nevertheless, other properties such as chemical stability, oxidation and corrosion resistance, damage tolerance, and interaction with other materials at high temperature have to be taken into consideration before replace any component. In the specific case of the transportation industry the introduction of new materials can take decades, as the case of SiC_f/SiC composites.

Recently General Electric aviation introduced SiC_f/SiC composites as the turbine blade material in its recently developed engine (GE9X).[47] The engine has a 10 % higher efficiency with 20 % less cooling required for the turbine blades as compared to the engines using single crystalline super alloys. The new engine design has certainly an edge advantage over the old engines in terms of efficiency, but in terms of initial cost, it is expensive in lieu of the complexity of the manufacturing process of continuous fiber ceramic matrix composites.[48] The fabrication methods involve coating of the SiC fiber with pyrolytic carbon or Boron Nitride (BN) as an interphase and chemical vapor infiltration of SiC into the woven fabric of SiC_f . [49, 50] This is a complex and expensive process. Hence an economic alternative can be to use discontinuous fiber instead of continuous ones and use a powder metallurgy route to manufacture components.

Composites enables the design of a material for a specific application. Although metals, ceramics and polymers are the three-foundation stone of material science, drawing clear boundaries between the three will not allow us to engineer the material with the desired combination of properties. Specifically, when we need a merger of properties from both metal and ceramics, i.e. strength, toughness and high temperature inertness. Composites are again categorized as three major classes: (i) metal matrix composites (MMCs), (ii) ceramic matrix composites (CMCs), (iii) polymer matrix composites (PMCs). Since the context of discussion relates to material performing at high temperature, CMC is the wisest choice to make. CMCs are again divided according to the shape of the second phase: (i) particulate reinforced, and (ii) fiber reinforced composites. Fiber reinforced composites are at the same time divided into two classes (i) continuous-aligned and (ii) discontinuous-aligned/random. In the present work only discontinuous fiber ceramic matrix composite has been the focus. The composites fabricated in the current work is somewhat between aligned and randomly distributed fibers. It would be precise to say

that the distribution was aligned in one plane whereas random in other two planes. Short fiber reinforced composites are highly interesting because of the ease of manufacturing and the properties they offer. We have been exploring ceramic materials like Al_2O_3 , ZrO_2 , SiC , Si_3N_4 and many more as the matrix phase for the CMC whereas non-oxide ceramics like C fiber, SiC whiskers, SiC fibers and oxide ceramics like Al_2O_3 , mullite or glass fiber the reinforcement phase. The reinforcement phase can be in the form of particle, whiskers, chopped fiber or continuous fibers. It is intriguing on how a material composed of two brittle phase results in a composite which is tough and resilient to catastrophic failures. The secret lies in the interface of the fiber and matrix. During failure or internal cracking, the matrix and the fiber act as a tribo-pair. The friction and adhesion between the two phases decide the fate of the composite material and the direction of the crack tip. The dissipation of the crack tip stress field is the most efficient way to arrest a crack. If the fiber-matrix adhesion is too strong there is no de-bonding of the fiber from the matrix and the crack travels through the fiber. A favorable configuration will be when the crack gets deviated along the interface of the matrix and the fiber. This is referred to as crack deflection by matrix-fiber de-cohesion. For a better control on the fiber-matrix interface de-cohesion, an inter-phase is used which does not have any chemical interaction either with the matrix or the fiber but have the right coefficient of friction with respect to matrix and fiber. It maintains the physical integrity and yet facilitate de-cohesion above a certain value of crack tip stress. On the other hand, a strong interface between fiber and matrix results in strengthening, hence an optimum interfacial strength is required to have a balance of strength and toughness. In continuous fiber CMCs, the load bearing components are both matrix and fiber whereas for discontinuous fiber CMC, it depends on the length (l_c), diameter (d), ultimate strength of the fiber (σ_f), and the interfacial strength (σ_i) of the fiber and matrix. The critical length of fiber for effective load transfer from matrix to fiber is given by[51]:

$$l_c = \frac{\sigma_f d}{2\sigma_i} \quad (1.2)$$

A critical length of 1 mm is typical for many fiber-matrix combinations.[51] The fiber ends are not efficient in load transfer, the load transfer is maximum in the central part of the fiber. Fig.1.7 shows a schematic shows the distribution of stress along the fiber during load application. If the fiber length is equal to the critical length then the maximum load transfer is on a point whereas if the fiber length is higher than the critical length, the maximum load transfer is across the whole length of the fiber which is helpful for strengthening of the composite.

Below the critical length of the fiber there is no strengthening effect observed. With an increase in the fiber length the flexural strength increases almost linearly and approaches a value which is the strength for the composite with continuous fibers corresponding to the same volume fraction of the fiber.[52] The reinforcement efficiency of a discontinuous fiber composite is lower than the continuous counterpart. The reinforcement efficiency further decreases for randomly distributed fiber than for the aligned discontinuous fiber. The advantage with randomly distributed discontinuous fiber composite is that it is isotropic but there is a significant compromise in the reinforcement efficiency which goes down to 0.2 as compared to the aligned discontinuous fiber com-

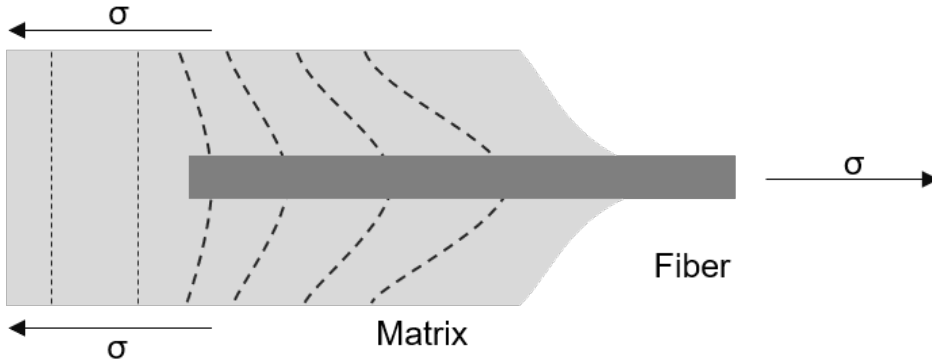


Figure 1.7: Stress distribution around the fiber during a fiber pullout phenomenon under tensile stress.

posite which is 1. The reinforcement efficiency of composites with fibers randomly distributed in one specific plane is 0.375 and so it is in the present case. The longitudinal strength (σ_{comp}) of the composite with a volume fraction (V_f) of aligned short fibers is given by:

$$\sigma_{comp} = \sigma_f V_f \left(1 - \frac{l_c}{2l} \right) + \sigma_m (1 - V_f) \quad (1.3)$$

Where σ_f and σ_m are the fracture strength of the fiber and matrix respectively. This expression holds valid when the length of the fiber (l) exceeds the critical length.[51] The toughening mechanism of the short fiber CMC is by deflection of crack by the presence of fiber or by fiber pullout in the vicinity of the crack tip. As compared to the continuous fiber counterpart, short fiber CMCs cannot undergo extensive fiber pullout because of the length constraint (Fig.1.8). Toughening requires a low shear strength of the fiber-matrix interface for the crack to deviate along the interface as shown in Fig.1.8. The coefficient of thermal expansion (CTE) of the composite follows the simple rule of mixture of matrix and fiber phases.[53] However, there are residual tensile stresses acting perpendicular to the fiber axis in the composite after sintering and cooling because of CTE mismatch of matrix and fiber phase. Circumferential cracks around the fibers indicate a mismatch of fiber/matrix CTE. There are different scenarios of CTE mismatch. The CTE of the matrix and fiber may match but the reaction between fiber and matrix might produce an interphase which has a different CTE and gives rise to residual stresses. Interphases with intermediate CTE are used to reduce the stresses arising from the CTE mismatch of fiber and matrix. The CTE has a vital role to play for the shear strength of the interface. It is required to minimize the matrix contraction as compared to the low contraction of the fiber after fabrication.[54]

For the usage of components at a high temperature for a prolonged time under a constant stress they should have good creep resistance at the operation temperature. Creep resistance is an important aspect which needs to be considered for thermo-mechanical applications.[48] MAX phases combined with fibers will provide a new avenue for the

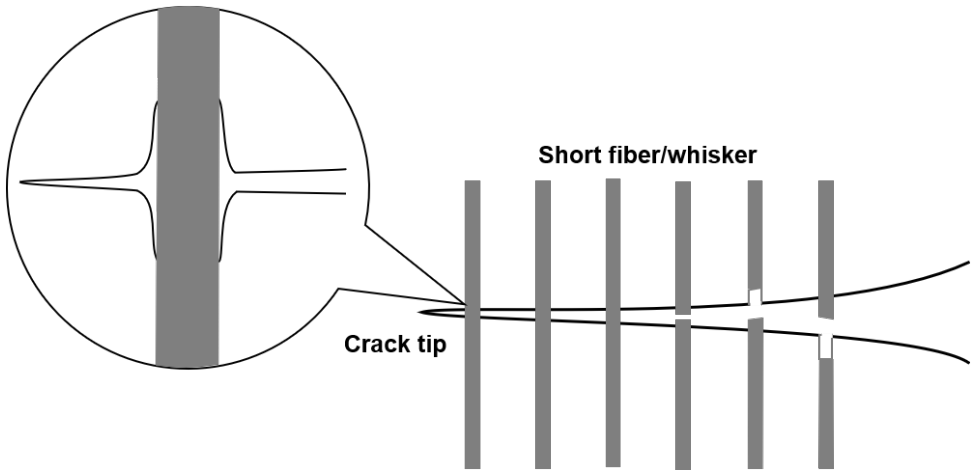


Figure 1.8: Schematic of minimizing crack tip stress intensity by fiber bridging.

exploration of new materials for thermo-mechanical application. Chapter 5 describes the fabrication of the monolithic Ti_3SiC_2 MAX phase alone and reinforced with short SiC fiber and whisker. The anisotropy of the material itself and the orientation of the reinforcement phase have been discussed. Chapter 6 deals with the creep resistance of the materials fabricated in Chapter 5. Compressive creep was performed on the monolithic materials as well as the composites with SiC fiber and whiskers. A detailed post creep microstructural analysis reveals the probable creep mechanisms of the composites.

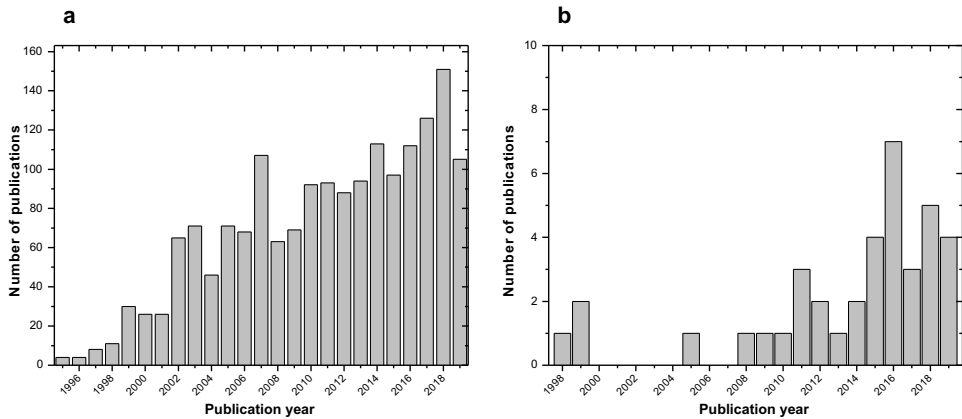


Figure 1.9: Number of papers published in the last two decades. **a** An estimate of papers on MAX phases when Ti_3SiC_2 , Ti_3AlC_2 , Cr_2AlC , Ti_2AlC was entered as the keyword, **b** shows the number of publications with a filter of 'fiber' and 'composites' applied to the result obtained in **a** from Web of Science (Source: Clarivate Analytics).

Although there has been an increasing interest in MAX phases which evident from

the number of papers published every year in the last two decades (Fig.1.9.a), investigation involving MAX phase based composites or reinforcing MAX phase with ceramic fibers have been very limited over the last 20 years (Fig.1.9). This thesis is an effort to bridge the gaps between MAX phase and ceramic matrix composites for high temperature applications.

REFERENCES

- [1] S. Omondi, *What was the first metal used by humans?* (2018).
- [2] *Brief history of ceramics and glass*, (2018).
- [3] *History and future of plastics*, (2019).
- [4] M. Radovic and M. W. Barsoum, *MAX phases: bridging the gap between metals and ceramics*, American Ceramics Society Bulletin **92**, 20 (2013).
- [5] M. W. Barsoum, *MAX phases: properties of machinable ternary carbides and nitrides* (John Wiley & Sons, 2013).
- [6] T. Lapauw, D. Tytko, K. Vanmeensel, S. Huang, P.-P. Choi, D. Raabe, E. N. Caspi, O. Ozeri, M. To Baben, J. M. Schneider, *et al.*, *(Nb_xZr_{1-x})₄AlC₃ MAX phase solid solutions: Processing, mechanical properties, and density functional theory calculations*, Inorganic chemistry **55**, 5445 (2016).
- [7] L. Chen, M. Dahlgvist, T. Lapauw, B. Tunca, F. Wang, J. Lu, R. Meshkian, K. Lambrinou, B. Blanpain, J. Vleugels, *et al.*, *Theoretical prediction and synthesis of (Cr_{2/3}Zr_{1/3})₂AlC i-MAX phase*, Inorganic chemistry **57**, 6237 (2018).
- [8] G. Bei, B.-J. Pedimonte, T. Fey, and P. Greil, *Oxidation behavior of MAX phase Ti₂Al_(1-x)Sn_xC solid solution*, Journal of the American Ceramic Society **96**, 1359 (2013).
- [9] M. Barsoum, T. El-Raghy, and M. Ali, *Processing and characterization of Ti₂AlC, Ti₂AlN and Ti₂AlC_{0.5}N_{0.5}*, Metallurgical and Materials Transactions A **31**, 1857 (2000).
- [10] T. Lapauw, B. Tunca, D. Potashnikov, A. Pesach, O. Ozeri, J. Vleugels, and K. Lambrinou, *The double solid solution (Zr,Nb)₂(Al,Sn)C MAX phase: a steric stability approach*, Scientific reports **8**, 1 (2018).
- [11] T. Okano, T. Yano, and T. Iseki, *Synthesis and mechanical properties of Ti₃SiC₂ ceramic*, in *Advanced Materials' 93* (Elsevier, 1994) pp. 597–600.
- [12] J.-F. Li, W. Pan, F. Sato, and R. Watanabe, *Mechanical properties of polycrystalline Ti₃SiC₂ at ambient and elevated temperatures*, Acta Materialia **49**, 937 (2001).
- [13] M. Barsoum, T. El-Raghy, C. Rawn, W. Porter, H. Wang, E. Payzant, and C. Hubbard, *Thermal properties of Ti₃SiC₂*, Journal of Physics and Chemistry of Solids **60**, 429 (1999).

- [14] W. Jeitschko, H. t. Nowotny, and F. Benesovsky, *Carbides of formula T_2MC* , Journal of the Less Common Metals **7**, 133 (1964).
- [15] W. Jeitschko, H. Nowotny, and F. Benesovsky, *Ti_2AlN , eine stickstoffhaltige H-phase*, Monatshefte für Chemie und verwandte Teile anderer Wissenschaften **94**, 1198 (1963).
- [16] W. Jeitschko and H. Nowotny, *Die kristallstruktur von Ti_3SiC_2 —ein neuer komplexcarbidgebiet*, Monatshefte für Chemie-Chemical Monthly **98**, 329 (1967).
- [17] M. W. Barsoum and T. El-Raghy, *Synthesis and characterization of a remarkable ceramic: Ti_3SiC_2* , Journal of the American Ceramic Society **79**, 1953 (1996).
- [18] D. J. Tallman, M. Naguib, B. Anasori, and M. W. Barsoum, *Tensile creep of Ti_2AlC in air in the temperature range 1000–1150 °C*, Scripta Materialia **66**, 805 (2012).
- [19] J. L. Smialek, *Environmental resistance of a Ti_2AlC -type MAX phase in a high pressure burner rig*, Journal of the European Ceramic Society **37**, 23 (2017).
- [20] G. Ying, X. He, M. Li, W. Han, F. He, and S. Du, *Synthesis and mechanical properties of high-purity Cr_2AlC ceramic*, Materials Science and Engineering: A **528**, 2635 (2011).
- [21] J. L. Smialek, *Oxygen diffusivity in alumina scales grown on Al-MAX phases*, Corrosion Science **91**, 281 (2015).
- [22] M. Haftani, M. S. Heydari, H. R. Baharvandi, and N. Ehsani, *Studying the oxidation of Ti_2AlC MAX phase in atmosphere: a review*, International Journal of Refractory Metals and Hard Materials **61**, 51 (2016).
- [23] M. Radovic, M. Barsoum, T. El-Raghy, J. Seidensticker, and S. Wiederhorn, *Tensile properties of Ti_3SiC_2 in the 25–1300 °C temperature range*, Acta materialia **48**, 453 (2000).
- [24] T. Zhen, M. Barsoum, S. Kalidindi, M. Radovic, Z. Sun, and T. El-Raghy, *Compressive creep of fine and coarse-grained Ti_3SiC_2 in air in the 1100–1300 °C temperature range*, Acta materialia **53**, 4963 (2005).
- [25] M. Radovic, M. Barsoum, T. El-Raghy, and S. Wiederhorn, *Tensile creep of coarse-grained Ti_3SiC_2 in the 1000–1200 °C temperature range*, Journal of Alloys and compounds **361**, 299 (2003).
- [26] M. Radovic, M. Barsoum, T. El-Raghy, and S. Wiederhorn, *Tensile creep of fine grained (3–5 μm) Ti_3SiC_2 in the 1000–1200 °C temperature range*, Acta materialia **49**, 4103 (2001).
- [27] A. Dash, R. Vaßen, O. Guillon, and J. Gonzalez-Julian, *Molten salt shielded synthesis of oxidation prone materials in air*, Nature materials **18**, 465 (2019).

- [28] T. El-Raghy, M. W. Barsoum, A. Zavaliangos, and S. R. Kalidindi, *Processing and mechanical properties of Ti_3SiC_2 : II, effect of grain size and deformation temperature*, Journal of the American ceramic society **82**, 2855 (1999).
- [29] M. W. Barsoum and M. Radovic, *Elastic and mechanical properties of the MAX phases*, Annual review of materials research **41**, 195 (2011).
- [30] T. Goto and T. Hirai, *Chemically vapor deposited Ti_3SiC_2* , Materials Research Bulletin **22**, 1195 (1987).
- [31] T. El-Raghy, A. Zavaliangos, M. W. Barsoum, and S. R. Kalidindi, *Damage mechanisms around hardness indentations in Ti_3SiC_2* , Journal of the American Ceramic Society **80**, 513 (1997).
- [32] M. Barsoum, L. Farber, and T. El-Raghy, *Dislocations, kink bands, and room-temperature plasticity of Ti_3SiC_2* , Metallurgical and Materials Transactions A **30**, 1727 (1999).
- [33] M. Radovic, M. Barsoum, T. El-Raghy, S. M. Wiederhorn, and W. E. Luecke, *Effect of temperature, strain rate and grain size on the mechanical response of Ti_3SiC_2 in tension*, Acta materialia **50**, 1297 (2002).
- [34] M. W. Barsoum, D. Brodtkin, and T. El-Raghy, *Layered machinable ceramics for high temperature applications*, Scripta Materialia **36** (1997).
- [35] C. J. Gilbert, D. Bloyer, M. Barsoum, T. El-Raghy, A. Tomsia, and R. Ritchie, *Fatigue-crack growth and fracture properties of coarse and fine-grained Ti_3SiC_2* , Scripta Materialia **42**, 761 (2000).
- [36] M. Barsoum, H.-I. Yoo, I. Polushina, V. Y. Rud, Y. V. Rud, and T. El-Raghy, *Electrical conductivity, thermopower, and hall effect of Ti_3AlC_2 , Ti_4AlN_3 , and Ti_3SiC_2* , Physical Review B **62**, 10194 (2000).
- [37] C. Fang, R. Ahuja, O. Eriksson, S. Li, U. Jansson, O. Wilhelmsson, and L. Hultman, *General trend of the mechanical properties of the ternary carbides M_3SiC_2 (M = transition metal)*, Physical Review B **74**, 054106 (2006).
- [38] D. Sarkar, B. Basu, M. C. Chu, and S. J. Cho, *R-curve behavior of Ti_3SiC_2* , Ceramics international **33**, 789 (2007).
- [39] D. Chen, K. Shirato, M. W. Barsoum, T. El-Raghy, and R. O. Ritchie, *Cyclic fatigue-crack growth and fracture properties in Ti_3SiC_2 ceramics at elevated temperatures*, Journal of the American Ceramic Society **84**, 2914 (2001).
- [40] N. Jones, C. Humphrey, L. Connor, O. Wilhelmsson, L. Hultman, H. Stone, F. Giuliani, and W. Clegg, *On the relevance of kinking to reversible hysteresis in MAX phases*, Acta materialia **69**, 149 (2014).
- [41] M. W. Barsoum, A. Murugaiah, S. R. Kalidindi, and T. Zhen, *Kinking nonlinear elastic solids, nanoindentations, and geology*, Physical review letters **92**, 255508 (2004).

- [42] A. Murugaiah, M. W. Barsoum, S. R. Kalidindi, and T. Zhen, *Spherical nanoindentations and kink bands in Ti_3SiC_2* , Journal of materials research **19**, 1139 (2004).
- [43] M. Barsoum, T. Zhen, S. Kalidindi, M. Radovic, and A. Murugaiah, *Fully reversible, dislocation-based compressive deformation of Ti_3SiC_2 to 1 GPa*, Nature Materials **2**, 107 (2003).
- [44] E. Orowan, *A type of plastic deformation new in metals*, Nature **149**, 643 (1942).
- [45] T. Zhen, M. Barsoum, and S. Kalidindi, *Effects of temperature, strain rate and grain size on the compressive properties of Ti_3SiC_2* , Acta materialia **53**, 4163 (2005).
- [46] F. J. Brooks, *GE gas turbine performance characteristics*, Ge Power Systems, GER-3567H **10** (2000).
- [47] F. W. Zok, *Ceramic-matrix composites enable revolutionary gains in turbine engine efficiency*, Am Ceram Soc Bull **95**, 22 (2016).
- [48] Z. Ren and G. Singh, *Nonoxide polymer-derived CMCs for “super” turbines*, American Ceramic Society bulletin **98** (2019).
- [49] F. Rebillat, J. Lamon, and A. Guette, *The concept of a strong interface applied to SiC/SiC composites with a BN interphase*, Acta materialia **48**, 4609 (2000).
- [50] M. A. Kmetz, J. M. Laliberte, W. S. Willis, S. L. Suib, and F. S. Galasso, *Synthesis, characterization, and tensile strength of CVI SiC/BN/SiC composites*, in *Proceedings of the 15th Annual Conference on Composites and Advanced Ceramic Materials: Ceramic Engineering and Science Proceedings* (Wiley Online Library, 1991) pp. 2161–2174.
- [51] W. D. Callister and D. G. Rethwisch, *Materials science and engineering*, Vol. 5 (John Wiley & sons NY, 2011).
- [52] B. Heidenreich, R. Renz, and W. Krenkel, *Short fibre reinforced CMC materials for high performance brakes*, High Temperature Ceramic Matrix Composites , 809 (2001).
- [53] I.-M. Low, *Ceramic-matrix composites: Microstructure, properties and applications* (Woodhead Publishing, 2006).
- [54] W. Krenkel, *Ceramic matrix composites: fiber reinforced ceramics and their applications* (John Wiley & Sons, 2008).

2

STATE OF THE ART

2.1. SYNTHESIS OF Ti_3SiC_2 MAX PHASE

Ti_3SiC_2 has been synthesized in the last decades by methods which needs a special equipment and infrastructure apart from a high temperature furnace. Go et al. synthesized Ti_3SiC_2 by chemical vapor deposition (CVD) using chloride gas precursors of Ti, Si and C along with H_2 . The dimensions of plate fabricated by this process were 40 x 12 x 0.4 mm.[1] Pampuch et al. synthesized Ti_3SiC_2 by solid combustion of elemental reactants, the mix of reactants were heated inductively at 1050 °C. The process was self-sustained and fast because of the exothermic nature of the reactions. The reaction products were composed of Ti_3SiC_2 and TiC.[2] Racault et al. synthesized Ti_3SiC_2 by heat treating elemental powders at 1100 °C resulting in a mixture of Ti_3SiC_2 , $TiSi_2$ and TiC. The content of Ti_3SiC_2 was reported to be nearly 85 wt.% The process involved a second step of removal of phases other than Ti_3SiC_2 by chemical dissolution of $TiSi_2$ in HF and oxidized TiC (TiO_2) in $(NH_4)_2SO_4$. Highly pure Ti_3SiC_2 was obtained but the process involved additional steps for purification.[3] Okano et al. synthesized Ti_3SiC_2 powders by calcining Ti, TiC and Si powders in the temperature range of 1300-1600 °C. The obtained powder was hot pressed at 1400 °C under 45 MPa for 30 min in argon. To obtain pure Ti_3SiC_2 , an excess of Si was added to compensate the vaporization of Si at high temperature.[4] Lis et al. synthesized Ti_3SiC_2 by ignition of mixed elemental precursors by tungsten heating coil. The temperature of ignition was measured to be 1830 °C. The purity of synthesized Ti_3SiC_2 was 70-90 wt.% with TiC as the second phase accompanied with traces of Ti and Ti_5Si_3 . [5] Arunajatesan et al. attempted the synthesis of Ti_3SiC_2 by mixing elemental powder and heating them in an alumina boat in the temperature range of 1270-1375 °C. In a separate attempt, the elemental powders were mixed and consolidated at room temperature to form a compact which was further treated in Argon protected Arc melting furnace with a tungsten electrode. The appropriate temperature and time combination were 1200 °C and 100 h, respectively. The most optimum composition with deficient Si resulted in Ti_3SiC_2 with 2 vol.% TiC.[6] Li et al. tried the reactive sintering of Ti, Si and TiC using a powder bed to reduce the Si evaporation. A pure single phase Ti_3SiC_2 was obtained in a temperature window of 1415-1420 °C. The

eutectic liquid in the Ti-Si system and the evaporation of Si was believed to be the controlling factor for the complete conversion of reactants into Ti_3SiC_2 . [7] Radhakrishnan et al. performed the reactive sintering of elemental precursors in hot press at 1350 °C for 5 h. The excess of Si (1.2 mole) resulted in high purity (98 vol.%) of Ti_3SiC_2 . The high temperature stability was demonstrated by annealing the sintered compacts at 1800 °C in argon for 10 h. Unlike the stoichiometric composition, reaction mixture with excess Si did not have any TiC as second phase, rather TiSi_2 as the ancillary phase. [8] A novel solid-liquid reaction process was introduced by Zhimei et al. for the synthesis of Ti_3SiC_2 . The addition of NaF to the reaction mixture of Ti, Si and C results in the formation of a liquid phase which increases the yield of Ti_3SiC_2 as compared to the solid-state reaction route. The exact reaction mechanism in the molten NaF was not reported. [9]

Lis et al. synthesized and consolidated Ti_3SiC_2 in one step by hot isostatic pressing (HIP) of elemental precursors. There is a combustion reaction between the precursors during HIP at 1000 °C and the system self-heated to 1800 °C. A range of temperatures were used for the synthesis process but the purity of Ti_3SiC_2 never increased beyond 75 vol.%. [10] The results on the synthesis of Ti_3SiC_2 did not yet spark the new trend of research in MAX phase until Barsoum and co-workers published their work referring Ti_3SiC_2 as a “remarkable ceramic”. Barsoum et al. was successful in synthesizing highly pure Ti_3SiC_2 by hot pressing (HP) Ti, SiC and C together at 1600 °C for 4 h. The phase purity was above 99 wt.%. It was this work which highlighted the excellent machinability of Ti_3SiC_2 and attributed this property to the layered nature of the material. The Young’s modulus was measured to be 320 GPa and the compressive yield strength was observed to decrease with temperature and at 1300 °C it was measured to be 260 MPa which is higher than any other superalloys known till date. It was also pointed out that Ti_3SiC_2 is not susceptible to thermal shock. In summary, this work highlighted the technological importance of Ti_3SiC_2 which led to the explosion of interest in MAX phase in general. [11] Li et al. did the reactive HIPing of Ti, Si and graphite powders by consecutive encapsulation of BN and boro-silicate glass. It was suggested that the reaction in the Ti-Si-C is not completely solid state rather a liquid in the Ti-Si system is also involved. [12] Sato et al. synthesized Ti_3SiC_2 by reaction synthesis of elemental powder at 1400 °C and the content of TiC was less than 4 vol.%. This group also mentioned the importance of the Ti-Si eutectic temperature on the yield of Ti_3SiC_2 . [13] Temperature fluctuation hot pressing of Ti, Si and C powders were carried out by heating the reaction mixture inside hot press to 1450 °C to melt the Si for initiation the liquid phase reaction. The temperature was then reduced to 1200 °C to avoid vaporization of Si. This method resulted in a short processing time and a higher yield of Ti_3SiC_2 . The microstructural analysis revealed that the grains consisted of thin hexagonal like plates which is an evidence of the growth of crystals from a liquid phase. [14] Yongming et al. synthesized Ti_3SiC_2 by in-situ hot pressing of elemental precursors. The purity of Ti_3SiC_2 obtained with 1.2 mole of Si was 99 wt.% as compared to 87 wt.% with 1 mole of Si. The content of Si was very crucial in determining the final purity of Ti_3SiC_2 . [15] Zhang et al. started with a unique reaction mixture of Ti, TiSi_2 and TiC for the synthesis of Ti_3SiC_2 . Gao et al. HIPed Ti, SiC and C at 1500 °C under 40 MPa for 30 min., the obtained purity of Ti_3SiC_2 was 97 vol.% and the sintered density was above 99%. [16] Sun et al. followed a fluctuation synthesis method for Ti_3SiC_2 . Ti,

Si and graphite powders were heated to 1300 °C for melting Si and then the temperature was reduced to 1200 °C for the molten Si to be consumed in the reaction forming Ti_3SiC_2 . After the molten Si was depleted, the reaction mixture was heated again to 1280 °C for re-melting Si. This process resulted in a substantial reduction in the total processing time and yielded twice the purity of Ti_3SiC_2 than that obtained by a solid-state route. The Ti_3SiC_2 powders obtained by this technique were of fibrous morphology.[17] Khoptiar et al. synthesized Ti_3SiC_2 by thermal explosion method. Thermal explosion is a variant of SHS which simultaneously takes place in the volume of the sample. The application of uniaxial pressure (80 MPa) at 1100 °C resulted in dense compacts (95%), however the content of TiC was nearly 45 wt.%. The modified SHS technique alone was not enough to obtain pure phase Ti_3SiC_2 and had the need of additional HIP treatment.[18]

Goesmann et al. followed a novel route of electron beam ignited solid state reaction for the synthesis of Ti_3SiC_2 . Ti and modified SiC powder were mixed and consolidated at room temperature. The sample was heated by electron beam to 900 °C after which the reaction self-propagated and the temperature was estimated to reach between 1700 °C and 2617 °C. Finally, the reaction mixture was again heated with electron beam to evaporate the excess Si. The Ti_3SiC_2 obtained contained less than 8 wt.% of secondary phases.[19]

Gao et al. synthesized and sintered Ti_3SiC_2 , with some TiC second phase, in one step by FAST/SPS Ti/Si/2TiC at 1250 °C.[20] SPS uses electric current to heat up the material in vacuum with the advantage of very high heating rates and externally applied load. Feng et al. carried out the synthesis of Ti_3SiC_2 by field assisted sintering technique most commonly known as spark plasma sintering (SPS). Ti, Si and graphite powder were mixed in ball mill for 20 h and heat treated in SPS at 1525 °C for 2 h under 46.8 MPa. The synthesized Ti_3SiC_2 had only less than 2 mol.% of TiC as the second phase. A post treatment of the synthesized Ti_3SiC_2 in vacuum resulted in the formation of large amount of TiC whereas annealing in air at 1000 °C resulted in the formation of TiO_2 on the surface.[21] Pulse discharge sintering technique was used to both synthesize and consolidate the reaction mixture in the temperature range of 1100-1325 °C. The crystallization of Ti_3SiC_2 was observed 1200 °C and the ratio of Ti/ $TiSi_2$ /TiC as 1:1:3 was optimum for obtaining high purity of Ti_3SiC_2 . The highest purity obtained for Ti_3SiC_2 was 93 wt.%. The density of the sintered compacts was above 99% at sintering temperature of 1225 °C.[22] Li et al. used mechanical alloying (MA) of elemental powder with large balls for obtaining 95.8 vol.% Ti_3SiC_2 by subsequent annealing. The MA process largely depended on the size of the balls used because larger balls (\varnothing 20.6 mm) can carry more energy in the form of kinetic energy. The resulting impact on the powder particles creates a better intimacy among them resulting in a combustion reaction. The high affinity of Ti towards C results in the formation of TiC which is an unwanted phase in the synthesis of Ti_3SiC_2 . Extensive milling (400 h) of the precursors to amorphosize and a post annealing treatment at 1000 °C for 1 h is an alternative route involving MA for obtaining high purity fine Ti_3SiC_2 powders.[23] Zhang et al. used pulse discharge sintering process to heat up a reaction mixture of Ti, SiC and TiC in the temperature range of 1250-1450 °C. The optimum temperature was found to be 1350 °C for obtaining a purity of 92 wt.%. With the control of sintering temperature and soaking time, the microstructure of Ti_3SiC_2 could be tailored

to be fine, coarse or duplex.[24, 25] Yongming et al. hot pressed a mix of elemental powder with 0.2 mole excess of Si at 1600 °C for 2 h to obtain highly pure Ti_3SiC_2 with full density.[26] Zhu et al. showed that single phase Ti_3SiC_2 was synthesized by the addition of 0.2 mole to either elemental precursors or TiC as one of the starting materials. The elemental mix was SPSed at 1150-1250 °C for 10 min. whereas the reaction mix with TiC was hot pressed at 1300-1400 °C for 2 h. Irrespective of the starting material and the processing route, the addition of 0.2 mole of Al accelerated the reaction for the formation of Ti_3SiC_2 .[27]

Sun et al. was successful in synthesizing 99 wt.% Ti_3SiC_2 powder by heating mixed Ti, Si and TiC in 1:1.1:1 ratio in vacuum.[28, 29] This is an example of self-propagating high-temperature synthesis (SHS) where the heat generated by the reaction of precursors sustains further reaction. However, the control of homogeneity while processing a large quantity of powder is poor and hence the purity does not exceed that of commercially available Ti_3SiC_2 MAX phase.

2.2. MOLTEN SALT ASSISTED SYNTHESIS OF MAX PHASES

As mentioned above, there are different approaches to synthesize Ti_3SiC_2 with high yields. However, powders are typically required for further ceramic processing operation like pressing, slip casting, injection molding etc.[30, 31] Near net shaping of MAX phase is difficult because operations like injection molding[31], slip casting[30], tape casting[32] need powder as the starting material. The existing methods for producing MAX phase yields either dense samples or free powders in small quantity. Moreover for processing methods like deposition by spray technologies [33] on a substrate, powders with a controlled particle size are preferred and the conventional methods only yield dense blocks. The present work is a demonstration of the molten salt-based synthesis of large scale (1 kg) Ti_3SiC_2 MAX phase powder in air without the need of any milling operation. The current methods employed for the synthesis of MAX phases results in a dense block, which is further crushed and milled to obtain fine powders for subsequent processing. Comminution of dense blocks to fine powders require extra energy and milling introduces impurities from the milling jar and the balls resulting in a compromise of the purity of the powder. The milling of MAX phase is an energy intensive process and might also result in the self-ignition of the powders. Moreover, the usage of vacuum or argon for the prevention of oxidation at high temperature increases the cost of the process. Molten salts are also used as an alternative synthesis route for MAX phases, where the elemental precursors are mixed in a suitable metal halide salt and heat treated to obtain the respective phases. Molten salt is used as a medium for enhanced diffusion of reactants to form a targeted product at a relatively lower temperature than the conventional synthesis temperature.[34] The synthesis of Cr_2AlC [35, 36], Ti_3SiC_2 [37], Ti_2AlC and Ti_3AlC_2 [38] by molten salt is reported, but it is noteworthy that the synthesis process was carried out in a protective atmosphere of argon. The synthesis of MAX phase by molten salts is only briefly explored and is always carried out in a protective atmosphere. In the present work, we have developed a new method for the synthesis of Ti_3SiC_2 MAX phase powder in air from elemental powders by following a novel route reference as molten salt shielded synthesis (MS³). This process makes the milling step superfluous and yields

free flowing micro-metric powders. [39]

2.3. COMPOSITES WITH Ti_3SiC_2 AS THE MATRIX

2.3.1. PARTICLE REINFORCED CERAMIC MATRIX COMPOSITES

Tong et al. fabricated Ti_3SiC_2 /20 vol.% β -SiC composite by hot pressing the mixed powders at 1600 °C for 30 min. under a pressure of 45 MPa. The presence of SiC particles resulted in grain size refinement and inhibited the grain growth with a finer grain size as compared to that of monolithic Ti_3SiC_2 . The formation of 8 vol.% of TiC could not be avoided because of high sintering temperature. The addition of SiC particles led to the improvement of flexural strength at both room and high temperature (1200 °C). The oxidation resistance of the composite was also higher than that of pure Ti_3SiC_2 . [40] Radhakrishnan et al. synthesized Ti_3SiC_2 /SiC composites by in-situ displacement reactions of TiC and Si in the ratio of 3:2. A two-step heating in hot press was done at 1380 °C and 1500 °C for synthesis and densification respectively. The presence of SiC particles resulted in an increase of fracture toughness and hardness as compared to the monolithic Ti_3SiC_2 . [41] Ming et al. manufactured a new laminated composite of Si_3N_4 and Ti_3SiC_2 by hot pressing at 1600 °C for 2 h under a pressure of 25 MPa. The laminated structure resulted in multiple toughening mechanism by crack deflection along the weak interface of Ti_3SiC_2 / Si_3N_4 and layered structure of Ti_3SiC_2 . The laminated microstructure resulted in the enhancement of mechanical properties and prevention of catastrophic failure of the composite. [26] Wang et al. mixed Al_2O_3 with Ti_3SiC_2 in the range of 10-20 vol.%. The composites were spark plasma sintered in the temperature of 1200-1400 °C. The addition of alumina resulted in increase of the hardness of the composite. Although the strength and the fracture toughness were slightly reduced, the composite has a higher wear resistance as compared to pure Ti_3SiC_2 . [42] Barsoum et al. prepared Ti_3SiC_2 /30 vol.% SiC and Ti_3SiC_2 /30 vol.% TiC composites. There was a substantial increase in hardness and its combination with the damage tolerance of Ti_3SiC_2 makes the composite a unique material. The oxidation resistance of Ti_3SiC_2 /SiC are better than Ti_3SiC_2 , whereas for Ti_3SiC_2 /TiC composites it is poorer than pure Ti_3SiC_2 . [43] Luo et al. sintered the composite of Al_2O_3 / Ti_3SiC_2 by hot pressing the mixed powders at 1600 °C for 2h. The highest toughness was obtained when the volume fraction of Ti_3SiC_2 was 0.5. [44] Zan et al. prepared multilayer laminated composite of Al_2O_3 and Ti_3SiC_2 by hot pressing at 1600 °C/4h. The interface was rich in TiC which led to a tensile residual stress in the matrix resulting in crack deflection along the interface of alumina and Ti_3SiC_2 thereby toughening the material. [45] Shi et al. attempted to fabricate a machinable bio-ceramic material by spark plasma sintering Ti_3SiC_2 and hydroxyapatite at 1200 °C. The composite was machinable if the content of Ti_3SiC_2 was above 20 vol.% The enhancement in mechanical properties of hydroxyapatite by the addition of Ti_3SiC_2 makes it a potential material for bone repair. [46] Li et al. fabricated Ti_3SiC_2 /c-BN composite by high pressure-high temperature technique at 1050 °C. A pressure of 4.5 GPa was applied to preserve the c-BN crystal structure to avoid the reaction between Ti_3SiC_2 and h-BN. These composites were reported to be a potential candidate for super hard materials. [47]

2.3.2. FIBER REINFORCED CERAMIC MATRIX COMPOSITES

Lenz et al. fabricated C_f/Ti_3SiC_2 composite by reactive melt infiltration of Si into C_f pre-forms impregnated with a mix of phenolic resin and TiC particles.[48] Mu et al. reported an increase in flexural strength with the addition of only 9 wt.% of Ti_3SiC_2 particles as filler in SiC_f/SiC composites.[49] Yin et al. manufactured C-SiC- Ti_3SiC_2 hybrid composites by the combination of TiC slurry and liquid silicon infiltration.[50] The final composite had 4 vol.% of Ti_3SiC_2 which resulted in the improvement of both flexural strength and fracture toughness. Lagos et al. fabricated Ti_3SiC_2 based CMCs by densification with spark plasma sintering of mixed chopped carbon fiber and Ti_3SiC_2 powder.[51] There was an interfacial reaction between carbon fiber and Ti_3SiC_2 which might lead to the degradation of mechanical properties. It was reported by Spencer et al. that Ti_3SiC_2 does not react with SiC fibers even at higher temperatures of 1550 °C and hence SiC_w was selected as the reinforcement in the present work.[52] The inertness of SiC with respect to Ti_3SiC_2 provides the possibility of SiC_w / Ti_3SiC_2 CMCs. Gonzalez et al. fabricated SiC fiber containing CMCs with Cr_2AlC and Ti_2AlC MAX phases as the matrix.[31] It is noteworthy that Al containing MAX phases have a reactivity with SiC and hence Ti_3SiC_2 MAX phase was used as the matrix in the present study. The evaluation of mechanical properties of MAX phase-based composites are majorly done at room temperature. The high temperature mechanical property evaluation of short fiber reinforced MAX phase has not previously been reported and the current dissertation presents the evaluation of compressive creep of SiC whisker reinforced Ti_3SiC_2 MAX phase.

2.4. MECHANICAL PROPERTIES OF MAX PHASES

2.4.1. ROOM TEMPERATURE MECHANICAL PROPERTIES

It was pointed out by El-raghy et al. that MAX phases can fail both in a brittle manner and in a ductile way.[53] The factors deciding the way MAX phases fail under stress are grain size, load at failure and the rate at which the strain is applied. An observation by Barsoum et al. suggests that it is the fine grained MAX phase which fails in a brittle fashion and the coarse grained MAX phase follows a so called graceful failure.[54] Fine grained MAX phases are also resilient to a higher compressive stress as compared to coarse grained counterparts. Zhang et al. attributed the graceful failure mechanism to shear band formation.[55] Moreover, such shear band formation was also observed in other layered solids like ice. Tzenov et al. made some conclusions about the ease of shear band formation after investigating the deformed surface of Ti_3AlC_2 . Coarse grained MAX phases are more prone to the formation of shear band and thereby absorbing the mechanical stresses.[56] The strain rate is also a deciding factor for the mode of failure. The higher the strain rate, the lower is time allowed for the absorption of the stress by shear band formation. Hence, a higher strain rate leads to brittle failure. With the ultimate compressive stress obtained by Hu et al. for V_2AlC , it was established that MAX phases follow the empirical Hall-Petch equation which states that the yield strength of a material is proportional to $1/\sqrt{D}$ where D is the grain size of the material.[57] Since MAX phases are highly anisotropic material with the c-axis more than five times that of the a-axis in the hexagonal crystal. The microstructure of hot-pressed MAX phase are also anisotropic with the basal plane preferentially aligned to a specific direction depending on the MAX

phase and the processing route. Hence, the mechanical properties along different crystallographic directions are also expected to be different. This was validated by Bao et al. by compressive loads on Ti_3AlC_2 parallel and perpendicular to Ti_3AlC_2 . [58] Compressive loads applied parallel to the alignment of the basal plane results in the shear band formation along with kinking of the crystal, so this configuration has a higher load bearing capability than the basal plane and the axis of applied load being perpendicular to each other. It was reported by Radovic et al. that MAX phases under tensile stresses do not demonstrate any ductility and irrespective of the grain size the failure mode is always brittle. [59]

2.4.2. HIGH TEMPERATURE MECHANICAL PROPERTIES

MAX phases behave different at high temperature because they undergo a brittle to plastic transition. [59] The exact temperature of transition is specific to the MAX phase under investigation. Unlike other crystalline materials, MAX phase does not have additional slip systems activated at high temperature. The behavior of MAX phases under stress at high temperature is mainly governed by the accumulation and further relaxation of internal stresses. Since only basal slip is present, the glide of basal plane dislocation is only in two dimension and along the basal plane. Hence, there must be other mechanisms contributing to the deformation of MAX phase at high temperature. Since the dislocations are only constrained only in two dimension, the deformation cannot be completely accommodated by the dislocation glide along the basal plane and hence internal stresses are generated. [59] Such evidence for internal stresses were provided by Radovic et al. by loading Ti_3SiC_2 in tension. The samples kept recovering even after removal of the load. This implies that the internal stresses accumulated in the sample are trying to be relieved by expanding after compressive load and contracting after tensile load both at room and high temperature. [60] El Raghy et al. subjected Ti_3SiC_2 to compressive load and four-point bending loads above 1200 °C. The compressive strength and yield strength decreased at high temperature. Irrespective of the grain size, the materials undergo plastic deformation of more than 20%. For coarse grained Ti_3SiC_2 the compressive strength and yield strength reduced from 720 MPa to 330 MPa and 320 MPa to 100 MPa respectively. The plastic deformation was believed to be a combination of grain delamination, kinking and grain boundary de-cohesion. [61] Li et al. showed that the fracture strength and toughness decreased slightly at 1000 °C as compared to room temperature whereas at 1200 °C, the values were half that of the room temperature values. [62]

2.4.3. HIGH TEMPERATURE CREEP OF MAX PHASES

The mechanical properties like flexural strength (room and high temperature) [62] and tribological behavior [63] of MAX phase are well documented and reported, however creep investigations of MAX phase materials are very limited. [59, 64–66] Radovic et al. measured the tensile creep of both fine and coarse grained Ti_3SiC_2 in the temperature range of 1000-1200 °C. The coarse grained Ti_3SiC_2 had higher creep rate since large grains are more prone to delamination and kink-band formation thereby absorbing the stresses. The activation energies (≈ 460 kJ/mol) and stress exponent (1.5-2) for creep were similar for both coarse and fine grained Ti_3SiC_2 and dislocation creep was the proposed dominant mechanism. Since the stress exponent was same throughout the temperature

range, it was assumed that the rate controlling mechanism was same as well. Delamination were observed along the basal plane. The stress exponent and grain size exponents did not match to any classical creep models suggesting that the creep of MAX phase is a special case. It was clearly stated that the main creep mechanism is not one of the diffusion or grain boundary creep. The creep was a combination of dislocation glide, kinking and cavitation. The internal stress may have been accommodated by grain boundary sliding. The overall creep response was attributed to the formation and relaxation of internal stresses.[65, 66] Zhen et al. investigated the compressive creep of Ti_3SiC_2 in the temperature range of 1100-1300 °C. The creep rates in compression were one order of magnitude lower than that of in tension mode. It was reported that at higher stress (>70 MPa) the mechanism of creep changed from dislocation creep to sub-critical crack growth. The stress exponents were comparable to that in tensile creep. The main creep mechanism was reported to be dislocation creep with small contribution of grain boundary sliding as well. The fine grained Ti_3SiC_2 was more resistant to creep deformation than the coarse counterpart.[59] Tallman et al. conducted the tensile creep of Ti_2AlC at high temperature (1000-1150 °C). There were considerable kinking observed on the post-creep fracture surface. Since Ti_2AlC is an Al containing MAX phase, the activation energy and stress exponent was found to be lower than that of Ti_3SiC_2 . Both dislocation and grain boundary sliding were operating during creep deformation.[64]

REFERENCES

- [1] T. Goto and T. Hirai, *Chemically vapor deposited Ti_3SiC_2* , Materials Research Bulletin **22**, 1195 (1987).
- [2] R. Pampuch, J. Lis, L. Stobierski, and M. Tymkiewicz, *Solid combustion synthesis of Ti_3SiC_2* , Journal of the European Ceramic Society **5**, 283 (1989).
- [3] C. Racault, F. Langlais, and R. Naslain, *Solid-state synthesis and characterization of the ternary phase Ti_3SiC_2* , Journal of materials Science **29**, 3384 (1994).
- [4] T. Okano, T. Yano, and T. Iseki, *Synthesis and mechanical properties of Ti_3SiC_2 ceramic*, in *Advanced Materials' 93* (Elsevier, 1994) pp. 597–600.
- [5] J. Lis, R. Pampuch, J. Piekarczyk, and L. Stobierski, *New ceramics based on Ti_3SiC_2* , Ceramics International **19**, 219 (1993).
- [6] S. Arunajatesan and A. H. Carim, *Synthesis of titanium silicon carbide*, Journal of the American Ceramic Society **78**, 667 (1995).
- [7] J. Li and Y. Miyamoto, *Fabrication of monolithic Ti_3SiC_2 ceramic through reactive sintering of $Ti/Si/2TiC$* , Journal of materials synthesis and processing **7**, 91 (1999).
- [8] R. Radhakrishnan, J. Williams, and M. Akinc, *Synthesis and high-temperature stability of Ti_3SiC_2* , Journal of Alloys and Compounds **285**, 85 (1999).
- [9] S. Zhimei, Z. Yi, and Z. Yanchun, *Synthesis of Ti_3SiC_2 powders by a solid-liquid reaction process*, Scripta materialia **41**, 61 (1999).

- [10] J. Lis, Y. Miyamoto, R. Pampuch, and K. Tanihata, *Ti₃SiC-based materials prepared by HIP-SHS techniques*, Materials Letters **22**, 163 (1995).
- [11] M. W. Barsoum and T. El-Raghy, *Synthesis and characterization of a remarkable ceramic: Ti₃SiC₂*, Journal of the American Ceramic Society **79**, 1953 (1996).
- [12] J.-F. Li, F. Sato, and R. Watanabe, *Synthesis of Ti₃SiC₂ polycrystals by hot-isostatic pressing of the elemental powders*, Journal of materials science letters **18**, 1595 (1999).
- [13] F. Sato, J.-F. Li, and R. Watanabe, *Reaction synthesis of Ti₃SiC₂ from mixture of elemental powders*, Materials Transactions, JIM **41**, 605 (2000).
- [14] Y. Zhou and Z. Sun, *Temperature fluctuation/hot pressing synthesis of Ti₃SiC₂*, Journal of materials science **35**, 4343 (2000).
- [15] L. Yongming, P. Wei, L. Shuqin, C. Jian, and W. Ruigang, *Synthesis of highly pure Ti₃SiC₂ polycrystals by the in-situ hot-pressing and its characterization*, Journal of materials science letters **20**, 1691 (2001).
- [16] N. Gao, Y. Miyamoto, and D. Zhang, *Dense Ti₃SiC₂ prepared by reactive HIP*, Journal of materials science **34**, 4385 (1999).
- [17] Z. Sun and Y. Zhou, *Fluctuation synthesis and characterization of Ti₃SiC₂ powders*, Material Research Innovations **2**, 227 (1999).
- [18] Y. Khoptiar and I. Gotman, *Synthesis of dense Ti₃SiC₂-based ceramics by thermal explosion under pressure*, Journal of the European Ceramic Society **23**, 47 (2003).
- [19] F. Goesmann, R. Wenzel, and R. Schmid-Fetzer, *Preparation of Ti₃SiC₂ by electron-beam-ignited solid-state reaction*, Journal of the American Ceramic Society **81**, 3025 (1998).
- [20] N. Gao, J. Li, D. Zhang, and Y. Miyamoto, *Rapid synthesis of dense Ti₃SiC₂ by spark plasma sintering*, Journal of the European Ceramic Society **22**, 2365 (2002).
- [21] A. Feng, T. Orling, and Z. Munir, *Field-activated pressure-assisted combustion synthesis of polycrystalline Ti₃SiC₂*, Journal of materials research **14**, 925 (1999).
- [22] Z.-F. Zhang, Z.-M. Sun, H. Hashimoto, and T. Abe, *A new synthesis reaction of Ti₃SiC₂ from Ti/TiSi₂/TiC powder mixtures through pulse discharge sintering (PDS) technique*, Materials Research Innovations **5**, 185 (2002).
- [23] J.-F. Li, T. Matsuki, and R. Watanabe, *Mechanical-alloying-assisted synthesis of Ti₃SiC₂ powder*, Journal of the American Ceramic Society **85**, 1004 (2002).
- [24] Z. Zhang, Z. Sun, H. Hashimoto, and T. Abe, *A new synthesis reaction of Ti₃SiC₂ through pulse discharge sintering Ti/SiC/TiC powder*, Scripta materialia **45**, 1461 (2001).

- [25] Z. F. Zhang, Z. M. Sun, H. Hashimoto, and T. Abe, *Effects of sintering temperature and Si content on the purity of Ti_3SiC_2 synthesized from Ti/Si/TiC powders*, Journal of Alloys and Compounds **352**, 283 (2003).
- [26] L. Yongming, P. Wei, L. Shuqin, C. Jian, W. Ruigang, and L. Jianqiang, *Synthesis of high-purity Ti_3SiC_2 polycrystals by hot-pressing of the elemental powders*, Materials Letters **52**, 245 (2002).
- [27] J.-O. Zhu, B.-C. Mei, X.-W. Xu, and J. Liu, *Effect of aluminum on the reaction synthesis of ternary carbide Ti_3SiC_2* , Scripta materialia **49**, 693 (2003).
- [28] Z. Sun, S. Yang, and H. Hashimoto, *Ti_3SiC_2 powder synthesis*, Ceramics International **30**, 1873 (2004).
- [29] S. Yang, Z. M. Sun, H. Hashimoto, and T. Abe, *Synthesis of single-phase Ti_3SiC_2 powder*, Journal of the European Ceramic Society **23**, 3147 (2003).
- [30] K. Sato, M. Mishra, H. Hirano, T. S. Suzuki, and Y. Sakka, *Fabrication of textured Ti_3SiC_2 ceramic by slip casting in a strong magnetic field and pressureless sintering*, Journal of the Ceramic Society of Japan **122**, 817 (2014).
- [31] J. Gonzalez-Julian, L. Classen, M. Bram, R. Vaßen, and O. Guillon, *Near net shaping of monolithic and composite MAX phases by injection molding*, Journal of the American Ceramic Society **99**, 3210 (2016).
- [32] A. Murugaiah, A. Souchet, T. El-Raghy, M. Radovic, M. Sundberg, and M. Barsoum, *Tape casting, pressureless sintering, and grain growth in Ti_3SiC_2 compacts*, Journal of the American Ceramic Society **87**, 550 (2004).
- [33] H. Gutzmann, F. Gärtner, D. Höche, C. Blawert, and T. Klassen, *Cold spraying of Ti_2AlC MAX-phase coatings*, Journal of thermal spray technology **22**, 406 (2013).
- [34] X. Liu, N. Fechler, and M. Antonietti, *Salt melt synthesis of ceramics, semiconductors and carbon nanostructures*, Chemical Society Reviews **42**, 8237 (2013).
- [35] W.-B. Tian, P.-L. Wang, Y.-M. Kan, and G.-J. Zhang, *Cr_2AlC powders prepared by molten salt method*, Journal of alloys and compounds **461**, L5 (2008).
- [36] A. M. Abdelkader, *Molten salts electrochemical synthesis of Cr_2AlC* , Journal of the European Ceramic Society **36**, 33 (2016).
- [37] X. Guo, J. Wang, S. Yang, L. Gao, and B. Qian, *Preparation of Ti_3SiC_2 powders by the molten salt method*, Materials Letters **111**, 211 (2013).
- [38] T. Galvin, N. Hyatt, W. Rainforth, I. Reaney, and D. Shepherd, *Molten salt synthesis of MAX phases in the Ti-Al-C system*, Journal of the European Ceramic Society **38**, 4585 (2018).
- [39] A. Dash, R. Vaßen, O. Guillon, and J. Gonzalez-Julian, *Molten salt shielded synthesis of oxidation prone materials in air*, Nature materials **18**, 465 (2019).

- [40] X. Tong, T. Okano, T. Iseki, and T. Yano, *Synthesis and high temperature mechanical properties of Ti_3SiC_2/SiC composite*, Journal of materials science **30**, 3087 (1995).
- [41] R. Radhakrishnan, S. Bhaduri, C. Henager Jr, and J. Brimhall, *Synthesis of Ti_3SiC_2/SiC and $TiSi_2/SiC$ composites using displacement reactions in the Ti-Si-C system*, Scripta Materialia **34** (1996).
- [42] H. Wang, Z. Jin, and Y. Miyamoto, *Effect of Al_2O_3 on mechanical properties of Ti_3SiC_2/Al_2O_3 composite*, Ceramics international **28**, 931 (2002).
- [43] L. H. Ho-Duc, T. El-Raghy, and M. W. Barsoum, *Synthesis and characterization of 0.3 v_f $TiC-Ti_3SiC_2$ and 0.3 V_f $SiC-Ti_3SiC_2$ composites*, Journal of alloys and compounds **350**, 303 (2003).
- [44] Y. Luo, W. Pan, S. Li, R. Wang, and J. Li, *Fabrication of $Al_2O_3-Ti_3SiC_2$ composites and mechanical properties evaluation*, Materials Letters **57**, 2509 (2003).
- [45] Q. Zan, C.-a. Wang, Y. Huang, Z. Shike, and C. Li, *The interface-layer and interface in the Al_2O_3/Ti_3SiC_2 multilayer composites prepared by in situ synthesis*, Materials Letters **57**, 3826 (2003).
- [46] S. L. Shi and W. Pan, *Machinable Ti_3SiC_2 /hydroxyapatite bioceramic composites by spark plasma sintering*, Journal of the American Ceramic Society **90**, 3331 (2007).
- [47] Z. Li, A. Zhou, L. Li, L. Wang, M. Hu, S. Li, and S. Gupta, *Synthesis and characterization of novel Ti_3SiC_2-cBN composites*, Diamond and related materials **43**, 29 (2014).
- [48] F. Lenz and W. Krenkel, *Fabrication of fiber composites with a MAX phase matrix by reactive melt infiltration*, in IOP Conference Series: Materials Science and Engineering, Vol. 18 (IOP Publishing, 2011) p. 202030.
- [49] Y. Mu, W. Zhou, Y. Hu, Y. Qing, F. Luo, and D. Zhu, *Improvement of mechanical and dielectric properties of PIP- SiC_f/SiC composites by using Ti_3SiC_2 as inert filler*, Ceramics International **41**, 4199 (2015).
- [50] X. Yin, S. He, L. Zhang, S. Fan, L. Cheng, G. Tian, and T. Li, *Fabrication and characterization of a carbon fibre reinforced carbon-silicon carbide-titanium silicon carbide hybrid matrix composite*, Materials Science and Engineering: A **527**, 835 (2010).
- [51] M. Lagos, C. Pellegrini, I. Agote, N. Azurmendi, J. Barcena, M. Parco, L. Silvestroni, L. Zoli, and D. Sciti, *Ti_3SiC_2 -cf composites by spark plasma sintering: Processing, microstructure and thermo-mechanical properties*, Journal of the European Ceramic Society **39**, 2824 (2019).
- [52] C. B. Spencer, J. M. Córdoba, N. H. Obando, M. Radovic, M. Odén, L. Hultman, and M. W. Barsoum, *The reactivity of Ti_2AlC and Ti_3SiC_2 with SiC fibers and powders up to temperatures of 1550 °C*, Journal of the American Ceramic Society **94**, 1737 (2011).
- [53] M. Barsoum, L. Farber, and T. El-Raghy, *Dislocations, kink bands, and room-temperature plasticity of Ti_3SiC_2* , Metallurgical and Materials Transactions A **30**, 1727 (1999).

- [54] M. W. Barsoum, D. Brodtkin, and T. El-Raghy, *Layered machinable ceramics for high temperature applications*, Scripta Materialia **36** (1997).
- [55] Z. Zhang and Z. Sun, *Shear fracture behavior of Ti_3SiC_2 induced by compression at temperatures below 1000 °C*, Materials Science and Engineering: A **408**, 64 (2005).
- [56] N. V. Tzenov and M. W. Barsoum, *Synthesis and characterization of Ti_3AlC_2* , Journal of the American Ceramic Society **83**, 825 (2000).
- [57] C. Hu, L. He, M. Liu, X. Wang, J. Wang, M. Li, Y. Bao, and Y. Zhou, *In situ reaction synthesis and mechanical properties of V_2AlC* , Journal of the American Ceramic Society **91**, 4029 (2008).
- [58] Y. Bao, J. Chen, X. Wang, and Y. Zhou, *Shear strength and shear failure of layered machinable Ti_3AlC_2 ceramics*, Journal of the European Ceramic Society **24**, 855 (2004).
- [59] T. Zhen, M. Barsoum, S. Kalidindi, M. Radovic, Z. Sun, and T. El-Raghy, *Compressive creep of fine and coarse-grained Ti_3SiC_2 in air in the 1100–1300 °C temperature range*, Acta materialia **53**, 4963 (2005).
- [60] M. Radovic, M. Barsoum, T. El-Raghy, S. M. Wiederhorn, and W. E. Luecke, *Effect of temperature, strain rate and grain size on the mechanical response of Ti_3SiC_2 in tension*, Acta materialia **50**, 1297 (2002).
- [61] T. El-Raghy, M. W. Barsoum, A. Zavaliangos, and S. R. Kalidindi, *Processing and mechanical properties of Ti_3SiC_2 : II, effect of grain size and deformation temperature*, Journal of the American ceramic society **82**, 2855 (1999).
- [62] J.-F. Li, W. Pan, F. Sato, and R. Watanabe, *Mechanical properties of polycrystalline Ti_3SiC_2 at ambient and elevated temperatures*, Acta Materialia **49**, 937 (2001).
- [63] S. Gupta and M. Barsoum, *On the tribology of the MAX phases and their composites during dry sliding: a review*, Wear **271**, 1878 (2011).
- [64] D. J. Tallman, M. Naguib, B. Anasori, and M. W. Barsoum, *Tensile creep of Ti_2AlC in air in the temperature range 1000–1150 °C*, Scripta Materialia **66**, 805 (2012).
- [65] M. Radovic, M. Barsoum, T. El-Raghy, and S. Wiederhorn, *Tensile creep of coarse-grained Ti_3SiC_2 in the 1000–1200 °C temperature range*, Journal of Alloys and compounds **361**, 299 (2003).
- [66] M. Radovic, M. Barsoum, T. El-Raghy, and S. Wiederhorn, *Tensile creep of fine grained (3–5 μm) Ti_3SiC_2 in the 1000–1200 °C temperature range*, Acta materialia **49**, 4103 (2001).

3

MATERIALS & METHODS

3.1. SYNTHESIS OF MAX PHASE POWDERS

ELEMENTAL powders of Ti, Si, Al (>99.5%, Alfa Aesar, -325 mesh), graphite (Alfa Aesar, 2 μm) were mixed in the stoichiometric molar ratio of 3:1:0.2:2. KBr (Alfa Aesar) in 1:1 weight ratio was added to the resulting mix. The mixture was milled in a slurry form with ethanol and zirconia milling balls (\O 5mm) for 24 hours in a multidirectional mixer (Turbula, WAB, Switzerland). The resulting slurry was dried in a vertical column rotary evaporator at 60 $^{\circ}\text{C}$. The dried powder was sieved in 300 μm sieve to homogenize the agglomerate size. The dried powder was uniaxially pressed in a steel die under a pressure of 200 MPa followed by isostatic pressing at 300 MPa. The consolidated specimen was further encapsulated with KBr (Fig.3.1 I) and placed in a KBr salt bed inside a cylindrical alumina crucible covered with an alumina lid without any sealant. The KBr salt bed supplied with enough salt after melting to completely submerge the specimen with molten salt for protection against ambient oxidizing atmosphere. The chemical composition of the protective encapsulation and the salt bed should always be the same to avoid the formation of inhomogeneous eutectic at the interface of salt bed and the encapsulated material. The encapsulation of KBr was achieved by re-pressing the already consolidated green sample in a larger steel die with KBr on all sides of the green sample. The samples were heated in a resistance furnace (Nabertherm, Germany) to a temperature of 800 $^{\circ}\text{C}$ at a rate of 20 $^{\circ}\text{C}/\text{min}$ and further heated to 1250 $^{\circ}\text{C}$ at a rate of 5 $^{\circ}\text{C}/\text{min}$ with a soaking time of 1 hour at 1250 $^{\circ}\text{C}$ (Fig.3.1 II). The MAX phase powders were obtained after washing with distilled water repeatedly to dissolve the salt (Fig.3.1 III) followed by filtration (Fig.3.1 IV).

Here a novel process is presented for the synthesis of non-oxide ceramic materials, named Molten Salt Shielded Synthesis process (MS^3), which uses molten salts as a reaction medium and additionally protecting the ceramic powders from oxidation during high-temperature processing in air. Ti_3SiC_2 compositions with Si and Al excess were also synthesized to understand the effect of the same on the phase purity of Ti_3SiC_2 .

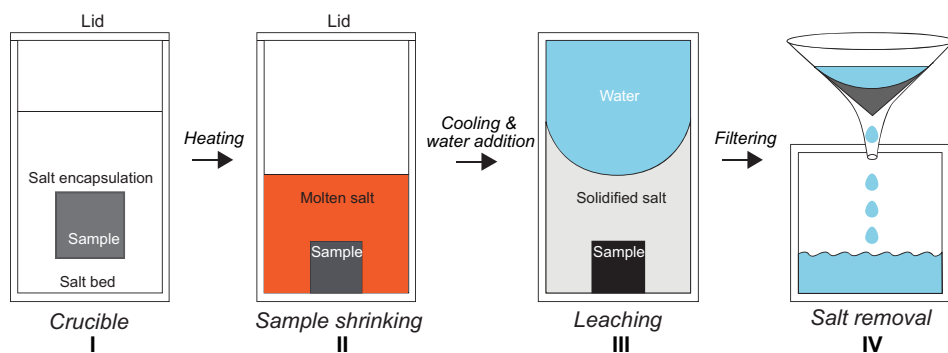


Figure 3.1: Stepwise schematic of MS³ process.

Ti₂AlN and MoAlB were also synthesized following the MS³ process as a proof of concept to demonstrate the possibility of the synthesis of ternary nitrides and borides. For Ti₂AlN, Elemental powders of Ti, Al (Alfa Aesar, -325 mesh) and TiN (d₅₀ 10 μm, H.C. Stark) were mixed in the stoichiometric molar ratio of 1:1:1. For MoAlB Elemental powders of Mo, Al (Alfa Aesar, -325 mesh) and AlB₂ (Rboschco, China, d₅₀ 10 μm) were mixed in the stoichiometric molar ratio of 2:1:1. The same procedure for synthesis and characterization was followed as for Ti₃SiC₂. Further optimization of temperature and composition of starting precursors needs to be done to obtain a pure phase material at a temperature as low as possible.

3.2. POWDER CHARACTERIZATION

Differential scanning calorimetry (DSC) and thermo-gravimetric (TG) analysis were performed in air on specimens with and without encapsulation of KBr to corroborate the absence of oxidation by MS³. Since the elemental precursors (Ti, Si, Al and C) will have their respective oxidation peaks and it would make the analysis cumbersome, pre-synthesized Ti₃SiC₂ powder was used for thermal analysis to demonstrate the possibility of MS³ process in air. 0.1 g of Ti₃SiC₂ were uniaxial pressed under 200 MPa into a small pellet of Ø 5 mm. The pellet was broken into pieces and one of the pieces was further encapsulated with KBr by re-pressing in a Ø 5 mm steel die. Such sample preparation was necessary due to the small crucible size of the DSC-TG instrument. After placing the encapsulated sample into the alumina crucible, the empty space was filled with KBr to provide a shielding effect by forming molten salt pool similar to the process of MS³. The furnace was heated at a rate of 20 °C/min to a temperature of 1300 °C followed by rapid cooling. The fact that the encapsulation of KBr acts as a barrier between the atmosphere and the sample in the pre-salt melting stage is demonstrated by measuring density and gas permeability of a 4 mm thick KBr disk cold pressed at room temperature. The KBr disk was pressed uni-axially at 200 MPa and then iso-statically at 300 MPa. The geometrical density was 98% of the theoretical value. The KBr disk was placed on gas tight O-ring and helium pressure was applied on one side whereas the concentration of helium was

measured on the other side. The permeability values of helium and air through the KBr disk were found to be $1.4\text{E-}7\text{ hPa}\cdot\text{dm}^3\cdot\text{s}^{-1}$ at room temperature, which suggests that the encapsulation of the sample by KBr is gas tight. Hence, a cladding thickness of 4mm is enough to isolate the sample material from ambient oxygen.

The powder obtained after MS³ process was scanned in a θ - 2θ X-ray diffractometer (XRD, D4 Bruker, Germany) using Cu-K α radiation (40kV, 40mA). A silicon single crystal sample holder was used to avoid any background signal in the X-ray diffraction pattern. A Rietveld refinement (Topas) was performed to obtain the purity and wt.% of the phases present in the synthesized powder.

Since the process is carried out in air, oxygen uptakes were measured. Synthesized Ti₃SiC₂ powder and sintered Ti pellet were analyzed for the oxygen content. The oxygen was determined by hot gas extraction using a Leco TCH 600 instrument. Sample amounts of 30 to 250 mg were analyzed at least in triplicate. The sample was packed in tin capsules and nickel baskets prior to heating in a carbon crucible. The amount of carbon dioxide collected after combustion gives the measure of oxygen present in the powder.

The particle size distribution was measured by laser diffraction instrument (LA-950V2, Partica, Horiba). Two light sources (405 nm and 650 nm) and two arrays of photodiode are used to detect the scattered laser from the particle. The particle size distribution is calculated by using Mie scattering theory. The instrument uses an inbuilt ultrasonic probe and agitator to avoid the agglomeration of particles during measurement.

The synthesized free flowing powders were sprinkled on a carbon tape and blown with pressurized carbon dioxide to remove the excess of powder. The sample was coated with platinum to reduce the charge accumulation during microscopy. The powder morphology was observed in a scanning electron microscope (SEM, Zeiss Ultra55, Oberkochen, Germany). The synthesized and milled Ti₃SiC₂ powders were observed in a transmission electron microscope (TEM, Zeiss Libra 200 Cs) to visualize the particle size. The powder was ultra-sonicated in ethanol medium for 30 mins. A drop of the suspension was dried in a copper grid which was later inserted into the TEM.

The reaction of elemental powders of Ti, Si, Al and C leading to the formation of Ti₃SiC₂ by the MS³ process were investigated by quenching the reaction mixtures at temperature range of 700-1300 °C. The reaction mixture of Ti/Si/C and Ti/Si/Al/C in the molar ratio of 3:1:2 and 3:1:0.2:2 were mixed with equal weight of KBr and the procedure similar to the process of MS³ was followed. There was no holding time at the set temperature. The reaction mixture was air quenched by pouring the molten salt along with the pellet onto a steel plate. The pellets were separated from re-solidified salt mechanically.

The quenched samples were dry ground on successive finer abrasive SiC papers and polished by an ion beam (IM4000, Hitachi). The polishing was not done with diamond suspensions to avoid contact of water or oil with the salt content of the sample. Since salt is soluble in the suspensions used for polishing, the complete process of grinding and polishing was kept dry. The quenched samples were coated with platinum and observed in a scanning electron microscope (SEM, Zeiss Ultra55, Oberkochen, Germany). Energy dispersive X-ray spectroscopy (EDS) was performed on points of interest of the quenched microstructures.

3.3. Ti_3SiC_2 BASED CERAMIC MATRIX COMPOSITE (CMCs)

CMCs containing SiC fiber and whisker were fabricated with Ti_3SiC_2 as the matrix. As received chopped Hi-Nicalon SiC fibers (length: 1 mm, \varnothing 10 μ m, NGS Advanced fibers, Japan) were processed to remove the metal catalyst used for the growth of whiskers. 10 g of SiC fibers (SiC_f) were mixed with 100 ml of 0.1M HNO_3 with continuous magnetic stirring at a temperature of 70 $^{\circ}C$ for 1 h. The suspension of SiC_f in dil. HNO_3 was filtered and repeatedly washed with de-ionized water to confirm the removal of added HNO_3 . Acid treated SiC_w were finally rinsed with ethanol and dried at 60 $^{\circ}C$ to avoid agglomeration. The same process was followed for cleaning -SiC whiskers (SiC_w , length: 10 μ m, \varnothing 1 μ m) Haydale technologies, USA).

The synthesized Ti_3SiC_2 was mixed with 10 and 20 vol.% of SiC_f in ethanol with high shear mixer in an ultrasonic bath for 1 h immediately followed by drying in a rotary evaporator to avoid segregation of phases due to density differences. The dried powder mix of Ti_3SiC_2 and SiC_w were loaded into a graphite die (\varnothing 20 mm) with a graphite foil. The weight of powder was so calculated to have a sintered block with 20 mm as diameter and 10 mm as height upon full densification by Spark Plasma Sintering (SPS, HPD5, FCT System, Germany). The graphite die with the powder was heated at a rate of 100 $^{\circ}C/min$ with a holding time of 35 mins and 80 MPa at the peak temperature of 1250 $^{\circ}C$ followed by rapid cooling. Additionally, a blank specimen based on monolithic Ti_3SiC_2 was sintered under the same conditions to be compared with the composites. In addition, a separate set of composites were sintered with SiC_w as the reinforcement phase rather than SiC_f . The volume fractions of SiC_w used for Ti_3SiC_2 composites were similar to that of composites with SiC_f . Table 3.1 summarizes the different grades of composites fabricated with different reinforcements.

Table 3.1: Grades of CMCs fabricated with Ti_3SiC_2 as matrix

Reinforcement	Sample ID
-	TSC
10 vol.% SiC_f	TSC-10 SiC_f
20 vol.% SiC_f	TSC-20 SiC_f
10 vol.% SiC_w	TSC-10 SiC_w
20 vol.% SiC_w	TSC-20 SiC_w

The sintered dense blocks were sand blasted to remove the graphite foil used to separate the contact between MAX phase and graphite die wall. The density was measured by Archimedes method of water displacement. Further the sintered block was ground plane-parallel and cylinders with a diameter of 5 mm and a height of 10 mm were obtained by electro-discharge machining. Three different blocks were sintered with monolithic Ti_3SiC_2 , and 10 and 20 vol.% of SiC_w which is referred to as TSC, TSC-10 SiC_w and TSC-20 SiC_w , respectively. The fabricated CMCs were analyzed for identifying crystalline phases by X-ray diffraction (XRD, D4 Bruker, Germany). The quantitative analysis from XRD data was obtained by Rietveld analysis using Topas software.

3.4. HIGH TEMPERATURE COMPRESSIVE CREEP

The creep testing was done in air at temperatures of 1100, 1200 and 1300 °C using constant loads corresponding to stress levels of 20-120 MPa. The creep data were not analyzed below 1100 °C since the deformation was too small (1 µm/day) and dominated by primary creep. The samples were heated to the test temperature at 5 K/min and a holding time of 1 h was allowed for equilibrium to be achieved between the furnace and sample temperature before the application of constant load by an electro-mechanical machine (INSTRON 1362). The creep tests were performed for a specific temperature and stress level until a deformation of 100 µm after which the tests were aborted. The deformation was measured by a linear variable differential transformer (Solartron Metrology). The same sample was subjected to a higher temperature and a higher stress after the deformation at a corresponding lower temperature and lower stress exceeded 100 µm. A total of 12 combinations of temperature and stress were used to measure the creep deformation on the single cylindrical specimen. The creep at lower temperatures (1100-1200 °C) might affect the creep at 1300 °C, hence creep measurements were in addition carried out on a pristine specimen by directly applying a higher load at a higher temperature (e.g. 1200 °C/80 MPa). The values for the total deformation over time and the minimum creep rate obtained in these tests were in agreement with the creep testing done by sequential increase of temperature and stress on the same sample, hence verifying the procedure.

Pole figures were measured using an X-ray diffractometer (Empyrean, PANalytical GmbH, Germany) with a five-axis cradle to identify preferential orientation of crystals in bulk materials. The intensity of X-ray from a single atomic plane were measured by tilting and rotating the sample. The tilting angle was swept from 0° to 85° and the rotating angle was varied from 0° to 360°. The intervals of both tilting angle and rotating angle was set to 5°. The orientation distribution function (ODF) of one specific crystal direction was analyzed with respect to the reference sample frame. X'Pert Texture (Malvern Panalytical) was used to generate the pole figures and ODF from the X-ray data measured by the diffractogram.

The samples before and after creep tests were ground and polished in both parallel and perpendicular direction of the applied load for electron backscattered diffraction (EBSD, Oxford Instruments, Aztec 2.4) analysis. To avoid the usage of highly corrosive HF for etching the grain boundaries, band contrast from kikuchi patterns were used for the reconstruction of an image which is a representation of the microstructure. Samples for transmission electron microscopy were prepared by Focused Ion beam machining of bulk samples to obtain a TEM lamella. The lamella was obtained from the center of the crept sample as it is believed to have undergone maximum deformation during creep. The lamella was characterized by TEM (FEI Tecnai G2 20S-TWIN).

4

RESULTS & DISCUSSIONS I

Molten salt shielded synthesis (MS³) of Ti₃SiC₂

4.1. MOLTEN SALT SHIELDED SYNTHESIS (MS³) PROCESS

MOLTEN salt synthesis for ceramic powders is well known, but for non-oxide compounds the process has been so far always carried out in argon atmosphere to protect the material from oxidation.[3, 4] These are efficient methods, but expensive, limiting their use at industrial scale. This limitation is particularly determinant for MAX phase since the lack of reliable synthesis processes to produce high pure powders in large quantities have hindered the commercialization of MAX phases. In the MS³ process, we have used potassium bromide (KBr) as the reaction medium. KBr has high ductility at room temperature and can be cold pressed to densities above 95 % relative density.[5, 6] We exploit this property of KBr to have a gas tight encapsulation around the specimen before placing it in the KBr salt bed for further heating. The heating can be divided into two segments: i) salt pre-melting and ii) salt post-melting. The gas-tight salt encapsulation protects the specimen from oxidation during salt pre-melting segment, whereas the post melting oxidation protection is achieved because the specimen is submerged in molten salt, and a barrier is formed between the ambient air and the sample. After cooling, the sample is recovered by dissolving the salt with water. Free powder is obtained by boiling the samples in water followed by filtration. Fig.4.1 shows the step-wise schematic of MS³ process.

Because elemental precursors (Ti, Si, Al and C) have their own respective oxidation temperature, which would make the analysis cumbersome, hence pre-synthesized Ti₃SiC₂ powder was used for thermal analysis to demonstrate the possibility of MS³ process in air. The specimens without encapsulation showed severe oxidation and an obvious increase in mass, whereas the encapsulated specimen showed a slight oxidation. As

Parts of this chapter have been published in Nature Materials **18**, 465 (2019) [1] and Journal of European Ceramic Society **39**, 3651 (2019) [2].



Figure 4.1: Schematic of molten salt shielded synthesis (MS^3).

Ti is highly prone to oxidation and is one of the precursors for the synthesis of Ti_3SiC_2 MAX phase. A similar DSC-TG investigation was performed with only Ti powder. The exothermic peak in Fig.4.2.a,c below 740 °C denotes the oxidation of Ti_3SiC_2 and Ti, respectively (red curve). An initial oxidation is observed in case of encapsulated Ti_3SiC_2 and Ti (blue curve).

The oxidation ceased after the melting point of KBr which is denoted by an endothermic peak at 740 °C (black curve). Fig.4.2.b,d show only initial mass gain of encapsulated samples due to oxidation (blue curve). Further heating results in mass loss in case of encapsulated samples due to the evaporation of salt. The mass loss trend is similar when only KBr is heated (black curve), whereas samples of Ti_3SiC_2 or Ti (Fig.4.2.b,d) heated without an encapsulation suffer only mass gain due to oxidation (red curve).

Fig.4.3 depicts the processing temperature window for a range of alkali and alkaline earth metal halide salts. The yellow, blue and grey regions correspond to the solid, liquid and vapor phase of the salt respectively. It is noteworthy that only the liquid phase temperature range provides the possibility of MS^3 . The processing is only possible if the synthesis temperature is within the temperature window and the oxidation temperature of the material is higher than the melting point of the salt. The eutectic temperature of 2 or 3 component salt system offers the possibility to have a very low melting point as in case of KCl-LiCl-NaCl. The phase evolution of Ti_3SiC_2 is similar to that when KBr was used as the salt medium. Although there are small peaks of TiC seen in the XRD (Fig.4.4), it is

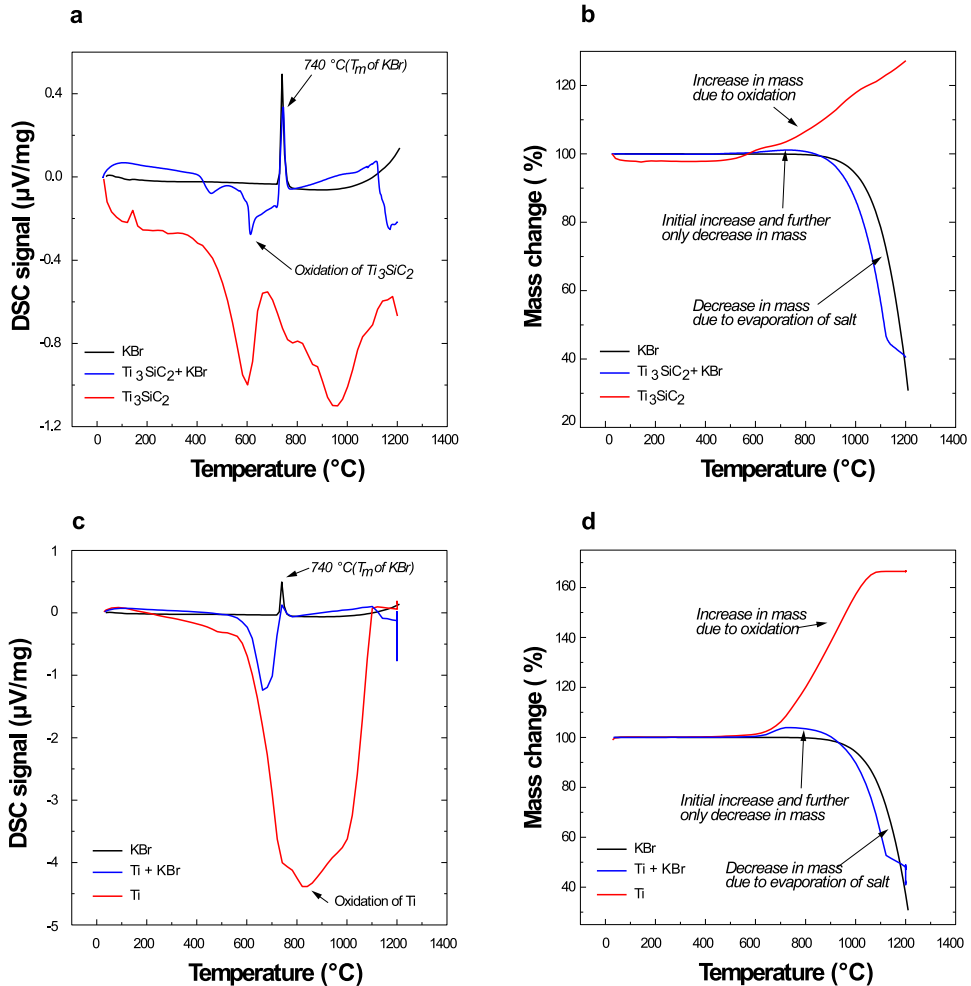


Figure 4.2: **a**, DSC of Ti₃SiC₂, KBr-encapsulated Ti₃SiC₂ and KBr conducted in air, **b**, TG of Ti₃SiC₂, KBr-encapsulated Ti₃SiC₂ and KBr conducted in air, **c**, DSC of Ti, KBr-encapsulated Ti and KBr conducted in air, **d**, TG of Ti, KBr-encapsulated Ti and KBr conducted in air.

noteworthy that there were no oxide phases detected by XRD. The XRD shows only peaks of TiC and TiSi₂ and no Ti₃SiC₂ phase or any oxide phase. Since the synthesis temperature was 1250 °C, it can be assumed that the diffusion of reactant species was not facilitated in the molten CaCl₂ and hence the reaction was incomplete. A higher temperature would be required to enable massive formation of Ti₃SiC₂ MAX phase. Nevertheless, the shielding effect was achieved even by using salts other than KBr, like LiCl-NaCl-KCl and CaCl₂. The synthesis of Ti₃SiC₂ was carried out with KCl-LiCl-NaCl and CaCl₂ under the same conditions as with KBr.

The prime criteria considered when selecting a salt system are for it to be cost-effective,

easily available and water soluble. The cation of the salt should be more electropositive than the material which is to be processed, to avoid possible reactions of the material with the salt. Ca based halides (CaCl₂ and CaBr₂) have very high boiling point and provides the possibility to process materials at temperatures close to 2000 °C which can be beneficial for the synthesis of advanced ceramics. The salts listed in Fig.4.3 are halides of group I and II from the periodic table. The higher members of the groups are not included because low price and water solubility are the prime criteria for MS³. Unlike potassium halide salts; MS³ process by any other salt listed in Fig.4.3 is also possible. However, the usage of other salts compromises the flexibility in terms of the precursors which can be chosen depending on the material which is being synthesized.

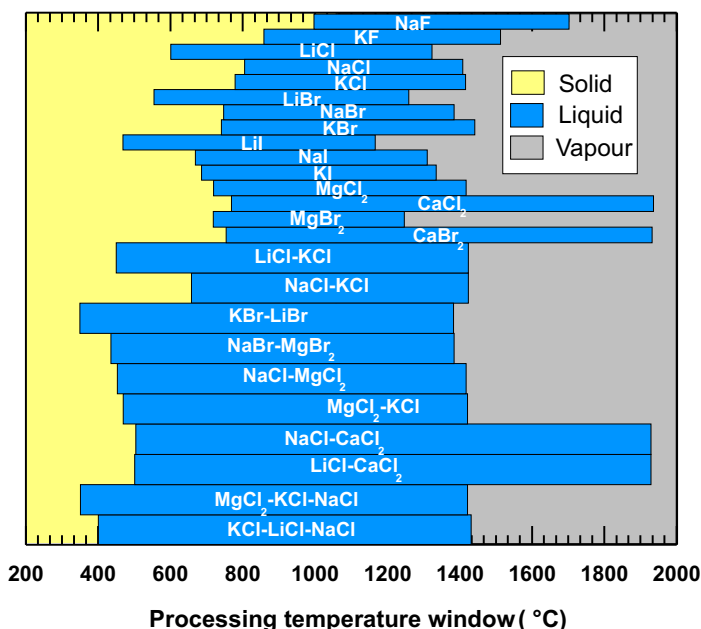


Figure 4.3: Processing temperature window for various salt compositions.

A chemical analysis for the estimation of oxygen was performed on Ti₃SiC₂ powder after washing it with hot distilled water for five times. The oxygen content was found to be 1.53 wt.% as compared to the initial oxygen content of 0.36 wt.%. The oxygen content is comparable to commercially available Ti₃SiC₂ MAX phase (1.25 wt.% O) whereas the phase purity is higher in case of the presently synthesized Ti₃SiC₂. The initial oxidation, results in a minute oxygen uptake as shown by the moderate increase in oxygen content of the sintered Ti (0.49 wt.% O) as compared to the starting Ti powder (0.32 wt.% O). The oxygen content of the initial powder and the salt used for the sintering is decisive to the final oxygen content of the component. A low temperature melting salt composition for MS³ can result in even lower oxygen uptake. Table 4.1 shows the oxygen content before and after MS³.

MS³ process is based on molten salt, so the inter-diffusion of the atomic species

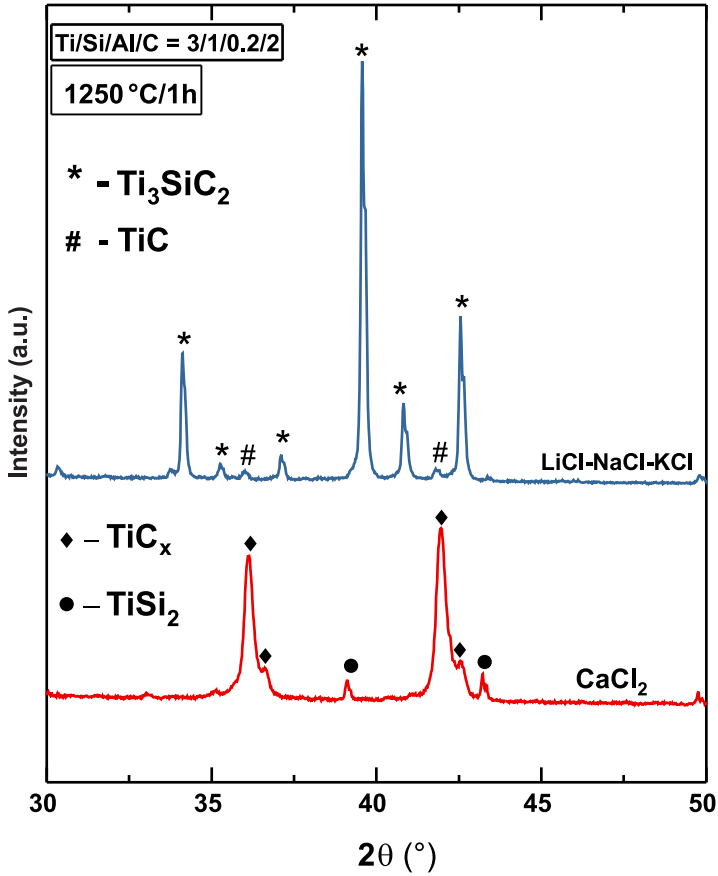


Figure 4.4: XRD of Ti_3SiC_2 synthesized at $1250^\circ\text{C}/1\text{ h}$ with LiCl-NaCl-KCl (blue curve) and CaCl_2 (red curve) as the molten salt medium for MS^3 .

Table 4.1: Summary of the Oxygen content measured before and after MS^3 process **a**, Oxygen uptake of Ti_3SiC_2 during synthesis. **b**, Oxygen uptake of Ti after sintering by MS^3 process in KBr .

a	Synthesis		Species	Sintering	
	Pre MS^3	Post MS^3		Pre MS^3	Post MS^3
	Oxygen wt. %			Oxygen wt. %	
	Ti	0.326	-	Ti	0.326
	Si	0.600	-		0.498
	Al	0.582	-		
	C	0.293	-		
	$\text{Ti}_3\text{SiAl}_{0.2}\text{C}_2$	0.361	1.530		

forming the targeted reaction product by dissolution-precipitation of different atomic species.[7] The molten salt provides a medium for the transport of metals in the form of ions. An oxidant has a major role to play for the diffusion of metal ions into the molten salt.[8] Since no oxidant was added to KBr melt, it is believed that small amounts of dissolved oxygen in the forms of superoxide and peroxide may have assisted the transfer of both metal ion and electron by hopping mechanism.[9] Fig.4.5.a,b shows the interaction zone of the material with salt in the cross-section of alumina crucible. A diffusion sphere is observed around the Ti plate in the solidified salt whereas there is none in case of Ti₃SiC₂, suggesting negligible mass loss from the sample in that case. Fig.4.5.c shows the presence of second-phase precipitates in the KBr solidified matrix.[10] EDS scans (Fig.4.5.e,f,g) near the interface (Fig.4.5.d) confirm that the globular dark grey inclusions (Fig.4.5.c) are Ti metal. This difference is probably because in the case of pure metals, no reaction partners are locally available for producing a new phase and dissolved metal ions can thus diffuse across longer distances through the molten salt. As a result, the synthesis temperature is reduced; Ti₃SiC₂ is typically formed by solid state reaction above 1350 °C whereas by MS³ the required temperature is 1250 °C. This also depends on the precursors used for the synthesis. The synthesis temperature was lowered by 100 °C in case of MS³, and this decrease was observed for other MAX phases as well.

4.2. REACTION MECHANISM FOR THE FORMATION OF Ti₃SiC₂ IN MOLTEN SALT

As mentioned earlier, the synthesis of Ti₃SiC₂ was done with 0.2 mole addition of Al. Hence, a systematic study of the effect of Si and Al excess content was done. Table 4.2 shows the nomenclature of the Ti₃SiC₂ compositions with excess Si and Al.

Table 4.2: Nomenclature of Ti₃Si_xAl_yC₂ compositions with different content of Si and Al

Elemental composition (moles)				Sample ID
Ti	Si(x)	Al(y)	C	Ti ₃ Si _x Al _y C ₂
3	1	0	2	TSC
3	1.1	0	2	TS1.1C
3	1.2	0	2	TS1.2C
3	1	0.1	2	TSA0.1C
3	1	0.2	2	TSA0.2C
3	1	0.3	2	TSA0.3C
3	1	0.4	2	TSA0.4C
3	1	0.5	2	TSA0.5C

The synthesis of Ti₃SiC₂ had been carried out with numerous processing routes but the molten salt synthesis route has been least explored and hence to propose a reaction mechanism leading to the formation of Ti₃SiC₂. The phase evolution and the reactions leading to the formation of the phases at every temperature were proposed based on the XRD of quenched samples supported by point scans of the polished quenched samples.

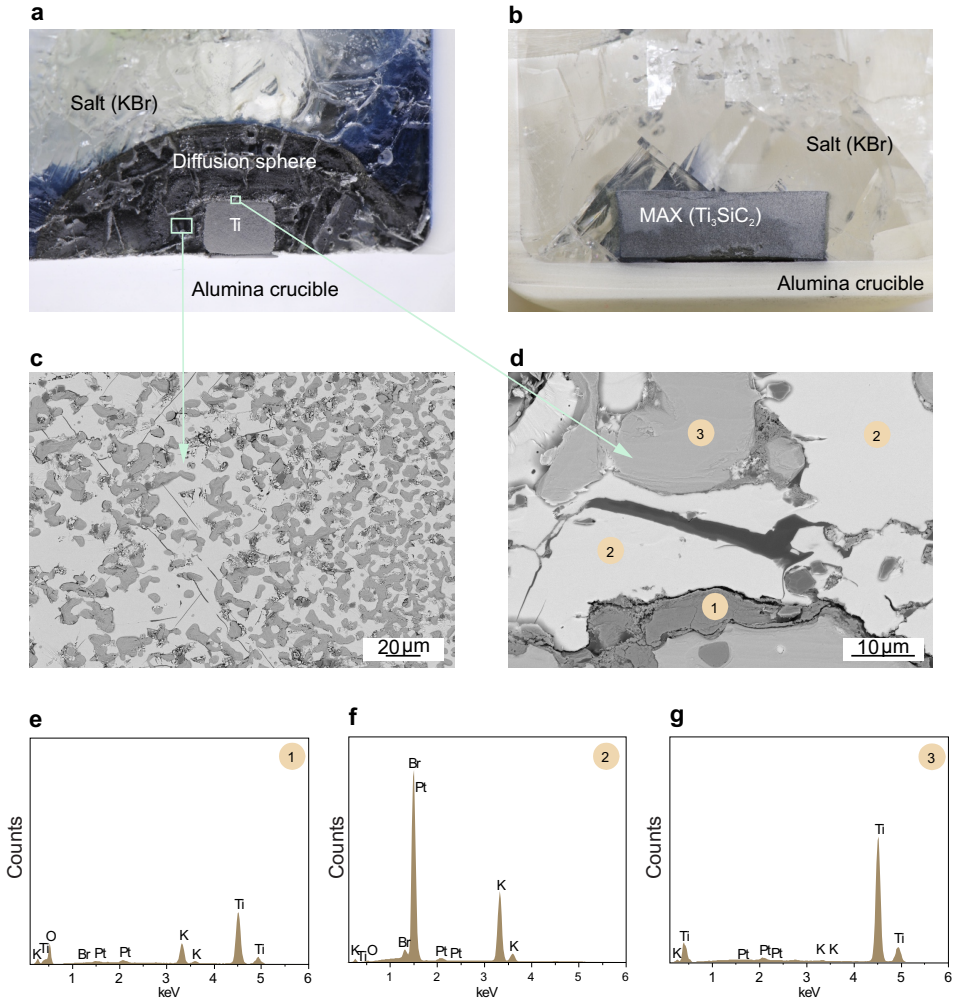
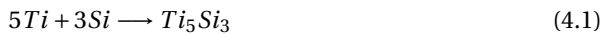


Figure 4.5: Cross-section of alumina crucible with **a**, Ti metal and **b**, Ti_3SiC_2 embedded in KBr, **c**, Back-scattered image of the area corresponding to yellow rectangle in **a**, **d**, Back-scattered image of the area corresponding with red rectangle in **a**, **(e,f,g)** EDS scans of corresponding points in **d**.

Fig.4.6 shows the XRD of quenched TSC at temperatures from 700 °C to 1300 °C. The melting temperature of KBr is 735 °C.[11] There was no reaction between the components at 700 °C because the particles of the starting elements were discrete and not in contact with each other because of the KBr content.

At 800 °C the molten salt mediated the reaction between Ti, Si and C and reaction products like Ti_5Si_3 , $TiSi_2$, and TiC were formed with some unreacted Ti, Si and C. The reactions can be depicted by the following equations:



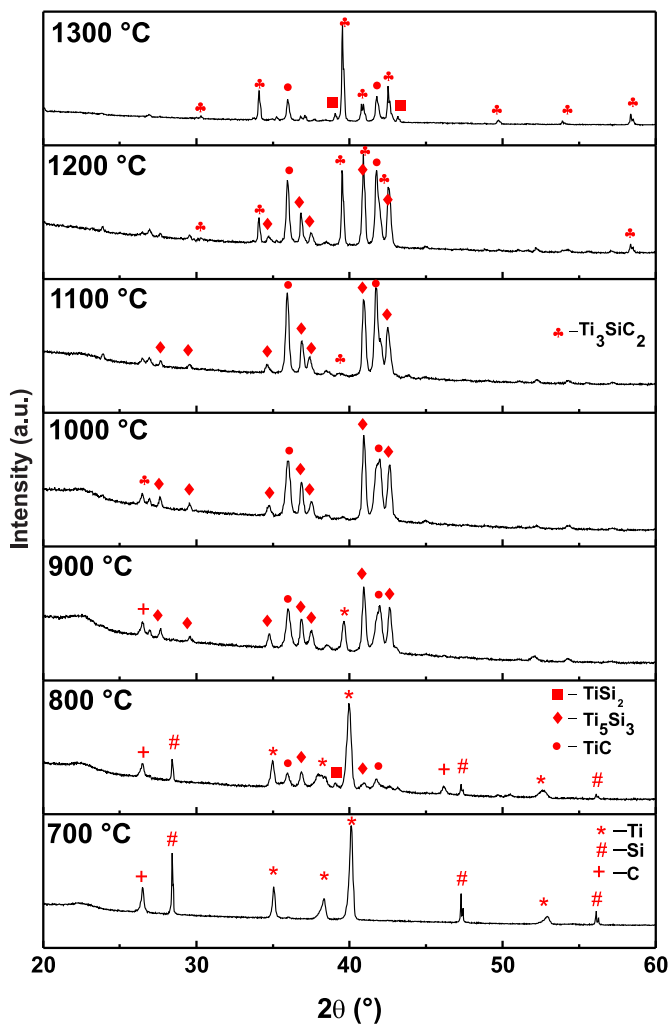


Figure 4.6: Phase evolution of TSC quenched at a temperature range of 700-1300 °C.

The cellular structure in Fig.4.7.a suggests incomplete melting of KBr and EDS point scans suggest the presence of Ti, Si and C as the major phases. The phases detected by XRD at 900 °C were Ti₅Si₃ and TiC mainly. The TiSi₂ observed at 800 °C disappeared due to a possible reaction with Ti according to:



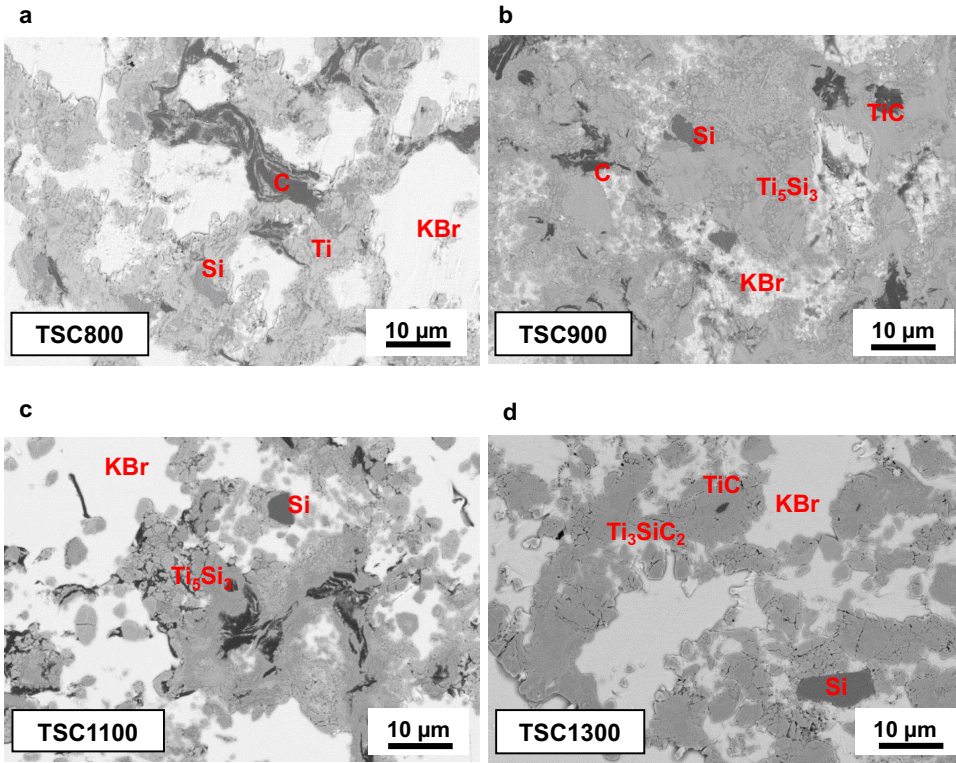


Figure 4.7: Quenched microstructures of TSC at **a** 800 °C, **b** 900 °C, **c** 1100 °C and **d** 1300 °C.

In the temperature range of 1000-1200 °C, the intensity of Ti_5Si_3 and TiC peaks increases indicating the formation of the same. Weak peaks of Ti_3SiC_2 were already visible at 1100 °C. The formation of Ti_3SiC_2 can be realized by the following reaction:



From 1000 °C – 1300 °C, the intensity of Ti_3SiC_2 peaks increased indicating the increase in the quantity of the respective phase. Fig.4.7.c shows the presence of graphite with platelet morphology. Even at 1300 °C there is un-reacted Ti_5Si_3 and TiC is present apart from Ti_3SiC_2 . There is a small amount of $TiSi_2$ re-formation which might be due to the reaction of Ti_3SiC_2 with residual C forming TiC_x and Si.[12]



EDS points scans in Fig.4.7.d depicts the presence of free Si which might have formed by the above-mentioned reaction. The Si formed in this reaction reacts with Ti_5Si_3 to form $TiSi_2$ and can be represented by the following reaction:



Solid state reaction of TSC results in the formation of Ti₅Si₃ and TiC as intermediate phase and its amount decreases from 1200 °C with the subsequent formation of Ti₃SiC₂ [13] whereas in the present work, the amount of Ti₅Si₃ and TiC starts decreasing from 1000 °C. Molten salt provides a medium for inter-diffusion of species even at a low temperature and hence the appearance of phases at low temperature as compared to the solid-state reaction. Intermediate phases like Ti₅Si₃C_x [14, 15] were not observed in the present synthesis route. Since the phase purity of Ti₃SiC₂ starting from stoichiometric composition was very low (81 wt.%), an excess of Si and Al was required to improve the purity of Ti₃SiC₂. 0.1 and 0.2 mole of excess Si was used as the starting reactants for the synthesis of Ti₃SiC₂.

4

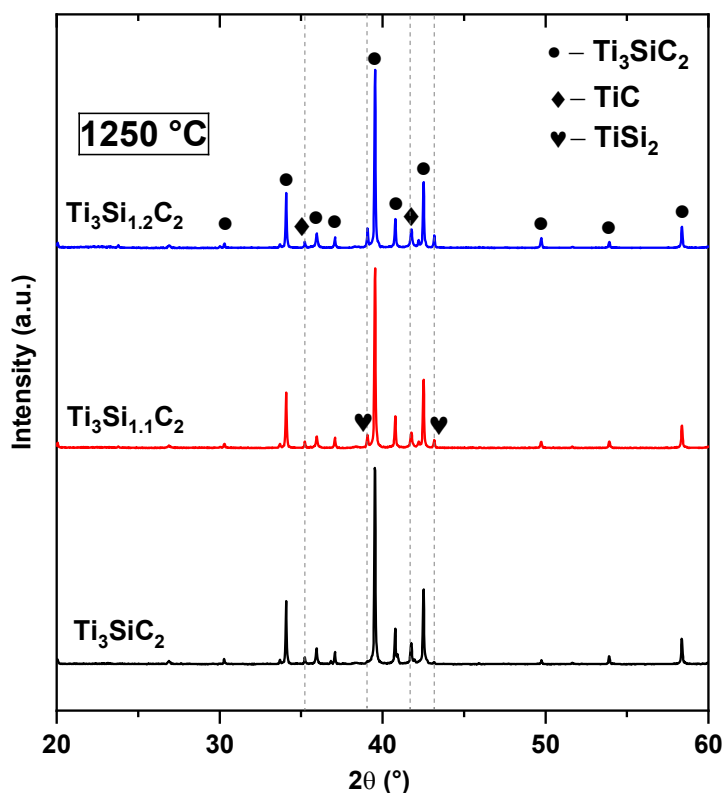


Figure 4.8: XRD of Ti₃SiC₂ with 0.1 and 0.2 excess of Si at 1250 °C for 1 h.

Compositions with stoichiometric amounts of elemental reactants result in formation of ancillary phases which are not desired and hence to maximize the amount of Ti₃SiC₂ formed, an excess of the A element (Si, Al) was added and the phase evolution was investigated. Fig.4.8 shows the XRD pattern for the phase evolution of Ti₃SiC₂ with excess Si at 1250 °C. The addition of 0.1 mole excess of Si resulted in the decrease in the intensity of TiC peak and formation of TiSi₂ whereas the the addition of 0.2 mole ex-

cess of Si resulted in further increase in the intensity of TiC peaks and an increase in the intensity of $TiSi_2$ phase due to the reaction of Si with Ti_3SiC_2 . [12]

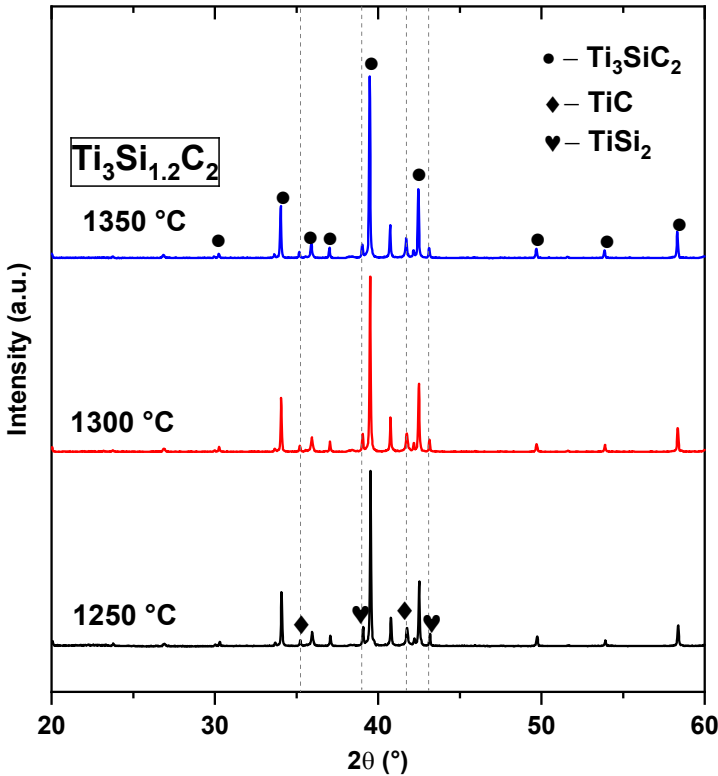


Figure 4.9: XRD of Ti_3SiC_2 with 0.2 excess of Si at a temperature range of 1250-1350 °C for 1 h.

An increase in temperature to 1350 °C for the composition with 0.2 mole excess of Si did not have any effect on the purity level of Ti_3SiC_2 . Fig.4.9 shows the XRD of Ti_3SiC_2 with 0.2 mole excess of Si synthesized at a temperature range of 1250-1350 °C. The excess of Si has a slight effect on the purity of Ti_3SiC_2 hence the addition of Al was done to assist the reaction resulting in the formation of Ti_3SiC_2 . Fig.4.10 shows the phase evolution of $Ti_3SiAl_xC_2$ synthesized at 1250 °C where “x” varies from 0.05 to 0.5 mol.%. With the addition of Al the content of TiC reduces. The addition of 0.1 mol. Al resulted in a highly pure Ti_3SiC_2 phase (97 wt.%) as compared to composition without Al addition (81 wt.%). Further addition of Al beyond 0.1 mol. resulted in the formation of Al_2O_3 without further increase in the purity of Ti_3SiC_2 . Table 4.3 shows the wt.% of the phases present in each composition of excess Al.

The quantitative analysis was done by Rietveld refinement. The calculated lattice parameter(c) (Table 4.3) suggests that Al did not form a solid solution with Ti_3SiC_2 rather Al just assisted the reaction leading to the formation of Ti_3SiC_2 . The increase in Al content leads to an increase in the purity of the Ti_3SiC_2 MAX phase. Beyond the content of 0.1 mole of Al, the formation of alumina is evident and the purity of Ti_3SiC_2 doesn't increase

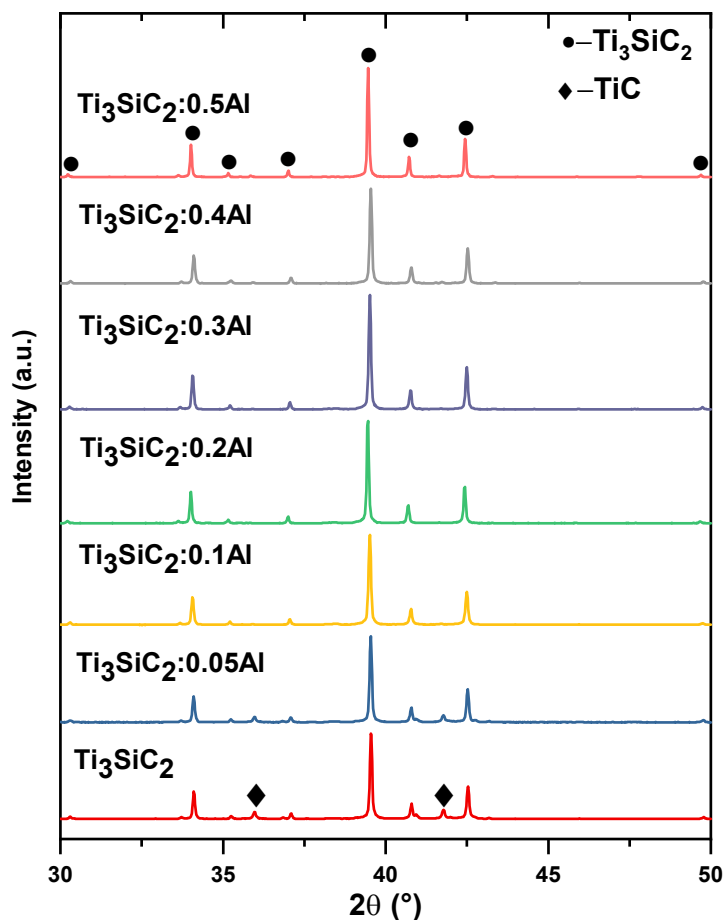


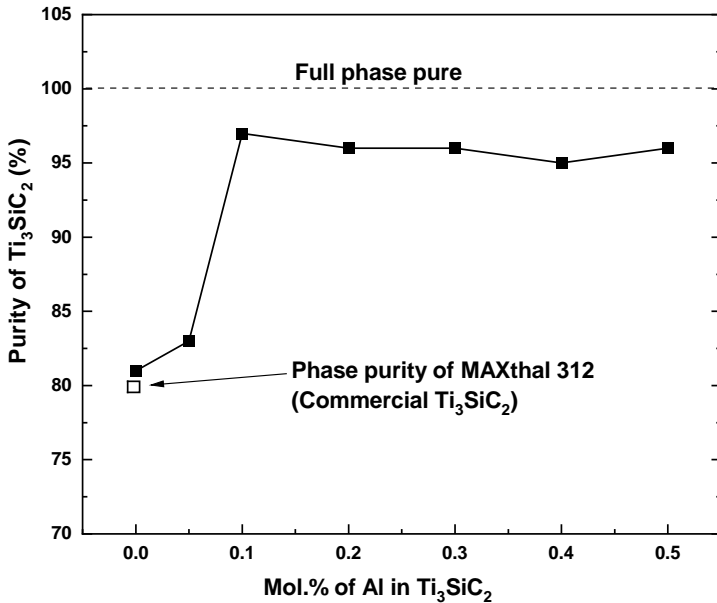
Figure 4.10: Phase evolution of Ti₃SiC₂ with different content of Al at 1250 °C for 1 h.

appreciably. Fig.4.11 shows the increase in the purity of Ti₃SiC₂ phase with the increase in Al content.

The commercially available Ti₃SiC₂ MAX phase with the trade name of MAXthal 312 manufactured by Sandvik Materials Technology only offers a purity of approximately 80 wt.% of Ti₃SiC₂ with the remainder as TiC. Since the processing route followed for the commercial production is self-propagating reaction method, the homogeneity of the reaction mixture is poor and hence the poor purity of the resultant reaction product. To understand the evolution of Ti₃SiC₂ phase with the addition of Al, similar quenching experiments were done and XRD and SEM-EDS analysis was performed. In the temperature range of 800-900 °C Ti₅Si₃, TiAl₃, TiC were formed. Fig.4.12 shows the XRD of TSAC reaction mixture quenched in a temperature range of 700-1300 °C. The peaks of TiAl₃ only appear at 900 °C and traces of TiAl₃ were detected by SEM/EDS. The formation of

Table 4.3: Evolution of phases with the addition of Al at 1250 °C/1 h

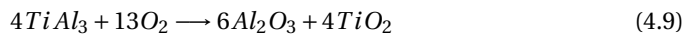
Al Mol. %	Ti_3SiC_2 (wt. %)	TiC (wt. %)	Ti_5Si_3 (wt. %)	$TiSi_2$ (wt. %)	Al_2O_3 (wt. %)	Lattice parameters (c) [Å]
0	81	11	6	2	-	17.68
0.05	83	9	6	2	-	17.68
0.1	97	3	-	-	-	17.68
0.2	96	3	-	-	1	17.69
0.3	96	2	-	-	2	17.69
0.4	95	2	-	-	3	17.69
0.5	96	2	-	-	2	17.68

Figure 4.11: Purity of Ti_3SiC_2 vs. content of Al added for the synthesis of Ti_3SiC_2 .

$TiAl_3$ can be given by:



The peaks of $TiAl_3$ were not visible above 900 °C; rather 1 wt.% of Al_2O_3 was detected at 1250 °C/1 h by Rietveld analysis. The presence of Al_2O_3 can be due to the native surface oxide from the starting powder or due to the following reaction:



The addition of Al acts as an oxygen getter and results in a more oxygen deficient reaction mixture which in turn yields a purer Ti_3SiC_2 phase. Moreover, Al might also reduce TiO_2 on the surface of Ti particles and facilitate better reaction of Ti particles with Si and C.

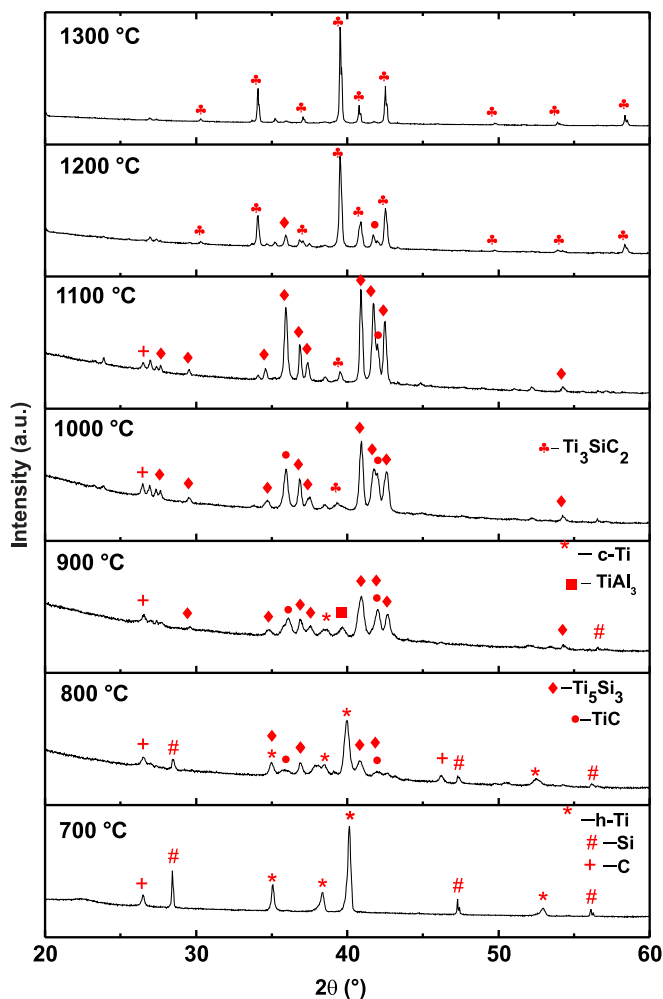
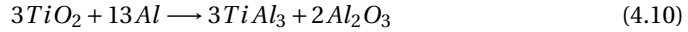


Figure 4.12: Phase evolution of TSA0.2C quenched at a temperature range of 700-1300 °C.

At 1100 °C, 5 wt.% of Ti₃SiC₂ was formed unlike to the reaction mixture without Al which only had traces of Ti₃SiC₂. The content of Ti₃SiC₂ at 1200 °C and 1300 °C are 71 wt.% and 96 wt.% respectively. The addition of Al not only resulted in a purer phase at the synthesis temperature (1250-1300 °C) but also at lower temperatures. Unlike Fig.4.7.a, Fig.4.13.a does not have cellular structure because of Al melting, the main phases identified by EDS and XRD were Ti and Ti₅Si₃. The reactants were dissolved in molten salt at 1100 °C and due to the sudden cooling caused by quenching; the reactants dissolved in the molten salt solidified in a spherical fashion. The samples quenched from 1100 °C (Fig.4.13.c) shows smaller alumina particles whereas the sample quenched from 1300 °C. Fig.4.13.d shows larger alumina particles which might have grown in the tempera-

ture range of 1100-1300 °C. The formation of alumina can be depicted by the following reaction[16]:



Native TiO_2 from starting powders and TiO_2 formed on the surface of the sample in the pre-melting stage of salt might react with Al to form alumina and $TiAl_3$. Moreover, the reduction of TiO_2 on the surface of Ti particles can facilitate better reaction of Ti particles with Si and C. Since the reaction is complete at 1300 °C, there are no more dissolved reactants in the molten salt and hence the grains of KBr can be clearly seen in Fig.4.13.d. Previous investigation suggests that the addition of 0.2 mol.% excess Si results in 95% pure Ti_3SiC_2 phase.[17, 18] The excess Si was assumed to compensate for the Si loss due to evaporation. In the present work the whole reaction mixture is submerged inside molten salt and there is no possibility of loss of Si by evaporation because the synthesis temperature is much lower than the melting point of Si. Experiments with excess of Si resulted in the formation of $TiSi_2$ rather than increasing the purity of Ti_3SiC_2 , whereas the addition of Al resulted in the increase of the purity of Ti_3SiC_2 .

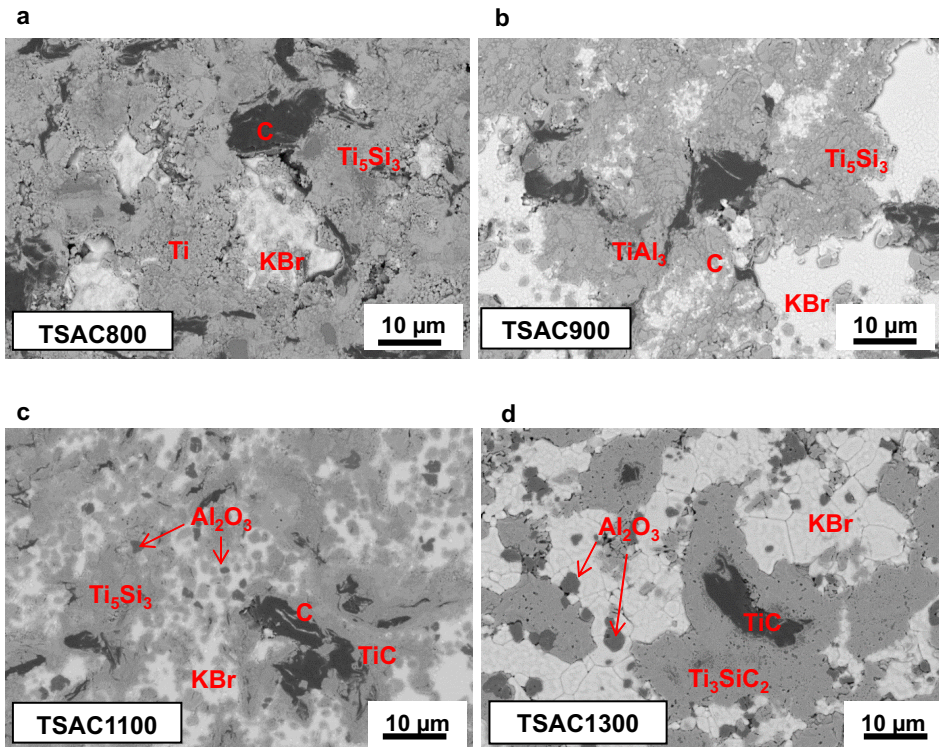


Figure 4.13: Quenched microstructures of TSA0.2C at **a** 800 °C, **b** 900 °C, **c** 1100 °C and **d** 1300 °C.

4.3. INTERFACIAL INVESTIGATION OF KBr-Ti₃SiC₂ WITH AND WITHOUT AL

For a better understanding of the role of Al in enhancing the purity of Ti₃SiC₂, an investigation was performed at the interface of the sample and the surrounding solidified molten salt. The alumina crucible with the sample and the solidified salt was cut into half. The section was ground with SiC paper and polished with ion beam. Fig.4.14.a shows the interface of Ti₃SiC₂ and KBr whereas Fig.4.14.b shows the interface of Ti₃SiC₂ with 0.2 mol.% of Al and KBr. The most obvious difference is that the interface of Ti₃SiC₂ with the addition of Al is clean and there are no second phase observed in the solidified KBr region. In Fig.4.14.a there are numerous artifacts in the KBr region.

4

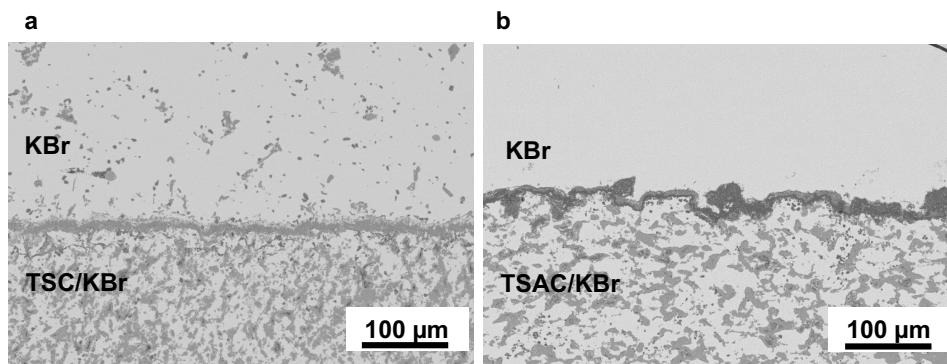


Figure 4.14: SEM of KBr-sample interface **a** Ti₃SiC₂ and **b** Ti₃SiC₂:0.2Al, synthesized at 1250 °C/1 h.

The phase contrast of the interface without Al addition suggests a single phase whereas the interface with Al addition has two phase contrast. Point EDS scans were performed on specific spots to identify the composition of the interface of KBr and Ti₃SiC₂ phase. Fig.4.15 shows the points of EDS scans and Table 4.4 mentions the possible phases from the EDS data (not shown here). The layer facing the KBr is composed of TiO₂ which might have formed due to the oxidation of Ti on the surface of the sample at low temperatures. The subsequent layer beneath the TiO₂ is composed of Al₂O₃ which might have formed due to the reaction of Al with TiO₂ or direct oxidation of Al to Al₂O₃. The interior of the sample showed the presence of only Ti₃SiC₂ and KBr. For a better representation, elemental mapping was performed on the interface of Ti₃SiC₂ and KBr with/without Al addition. Fig.4.16 shows the elemental mapping of the Ti₃SiC₂-KBr interface with and without Al addition. Apart from the fact that the interface (Fig.4.16.a) is TiO₂, it is noteworthy that the artifacts in the KBr region are composed of TiO₂ and metallic Si. It can be assumed that Si diffuses out to the KBr through the TiO₂ interface and hence the sample becomes deficient in both Si and Ti resulting in a lower purity of Ti₃SiC₂. In case of the sample with 0.2 mol.% of Al, the interface (Fig.4.16.d) is composed of both TiO₂ and Al₂O₃ which is impervious to the out-diffusion of TiO₂ and Si and hence the stoichiometric chemical composition is intact resulting in a higher phase purity of Ti₃SiC₂ (Table 4.5).

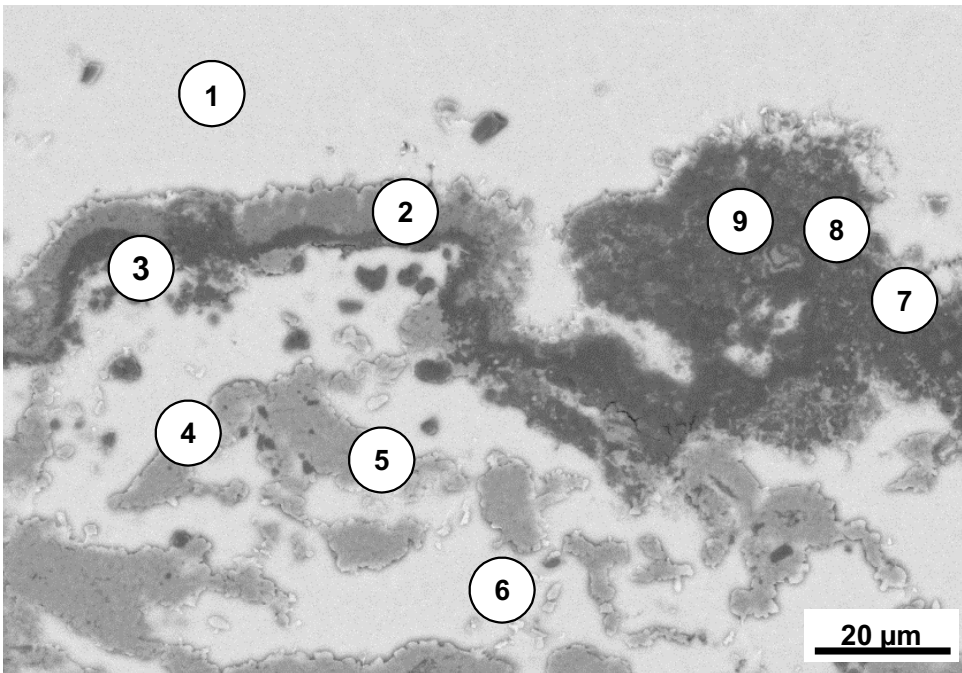


Figure 4.15: EDS point scans of KBr-TSA0.2C interface.

Table 4.4: EDS point scans of the interface of Ti₃SiC₂:0.2Al and KBr corresponding to Fig.4.15

Point	Ti	Si	Al	O	K	Br	Probable phase
1	X	X	X	X	✓	✓	KBr
2	✓	X	X	✓	✓	✓	TiO ₂
3	X	X	✓	✓	X	X	Al ₂ O ₃
4	X	X	X	X	✓	✓	KBr
5	✓	✓	X	X	X	X	Ti ₃ SiC ₂
6	X	X	X	X	✓	✓	KBr
7	X	✓	✓	✓	X	X	Al ₂ O ₃ + Si
8	✓	✓	✓	✓	X	X	TiO ₂ + Al ₂ O ₃ + Si
9	X	X	✓	✓	✓	✓	Al ₂ O ₃ + KBr

The Ti₃SiC₂ synthesized at 1250 °C/1 hr. with 0.2 mol.% Al was repeatedly washed with hot water to remove the KBr content. The synthesized Ti₃SiC₂ was 96 wt.% (Rietveld refinement of XRD data) pure and did not have any oxide second phase (as detected by XRD), 3 wt.% of TiC and 1 wt.% of Al₂O₃ were detected by XRD. The powder was free flowing after washing the salt content and did not need any extra milling. However, an optional milling step can be adopted to further tailor the particle size. Fig.4.17 shows the XRD of the synthesized Ti₃SiC₂ powders.

The addition of 0.2 mole of Al was done to enhance the purity of the synthesized

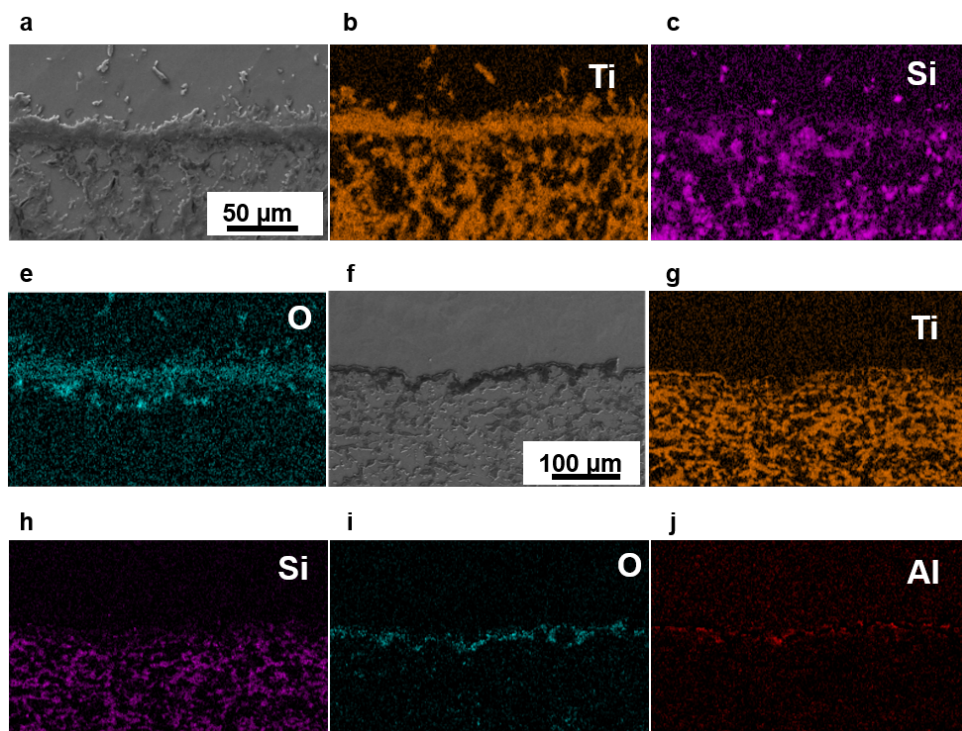


Figure 4.16: Elemental mapping of the interface of Ti_3SiC_2 /KBr **a** electron image **b** Ti, **c** Si, **d** O map and $Ti_3SiC_2:0.2Al$ /KBr **e** electron image **f** Ti, **g** Si, **h** O, **i** Al map.

Ti_3SiC_2 phase. The role of Al addition and the effect of the content of Al has been discussed later in the present chapter.

Fig.4.18.a shows the SEM of the loose powder which seems to be partially agglomerated. The platelet like morphology (Fig.4.18.b) and Fig.4.18.c the layered structure of the primary particles which is the characteristic of MAX phases. The particle size distribution (PSD) of as-synthesized Ti_3SiC_2 (Fig.4.18.d) which is unimodal with a d_{50} value of approximately $40 \mu m$. The synthesized Ti_3SiC_2 was agglomerated and hence the PSD is representative of secondary particle size.

4.4. MILLING STUDY OF SYNTHESIZED Ti_3SiC_2

Since the sintering of MAX phase powder needs pressure assisted consolidation techniques, there is always a need for fine particle size to have enhanced densification for sintering at low temperature. Milling was performed in a planetary ball mill for different times. Fig.4.19 shows the XRD of milled Ti_3SiC_2 . The increase in milling time resulted in a broadening of the peaks and reduction in the intensity of the peaks. Although the crystallite size decreases with increasing milling time, the lattice parameters are intact. For the sake of comparison milling was performed with synthesized Ti_3SiC_2 from solid

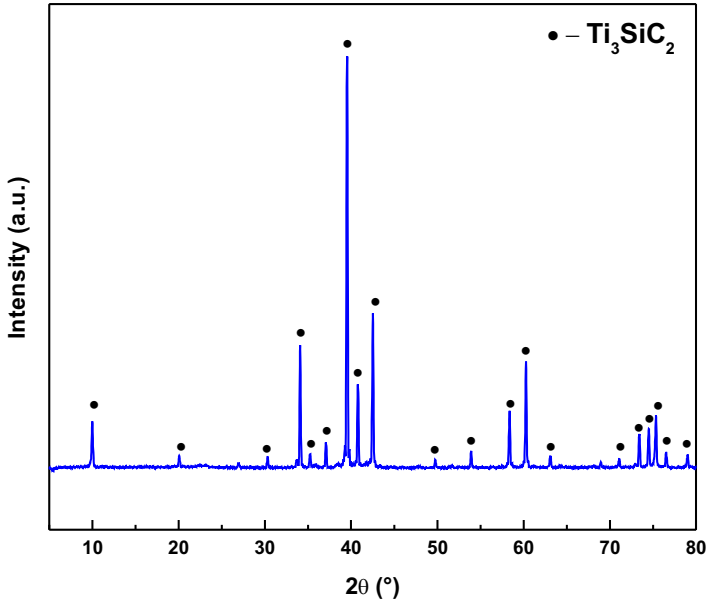


Figure 4.17: XRD of Ti_3SiC_2 synthesized at 1250 °C/1 h with the addition of 0.2 mole of Al.

state route and after a milling time of 1 hour the MAX phase lost its entity (phase change by decomposition) as Ti_3SiC_2 but the powder synthesized from molten salt route did not lose its crystal structure even after a milling time of 10 h.

Fig.4.20 shows the TEM of synthesized Ti_3SiC_2 powder milled for 6 h. The primary particle size is less than 100 nm and the micrograph with a higher magnification shows electron transparent region suggesting single layer/few layer of M-A-X atomic layer stacking. The sinterability of these nano-metric powders still needs to be investigated and is a scope for the future work.

The nanopowder obtained by milling synthesized Ti_3SiC_2 were formed due to the shear induced mechanical cleavage of layers of M-A-X structures from the bulk powder. It can be noted that the structures shown in Fig.4.20 correspond to that of MAXene and not MXene. MXene are graphene analogues of MAX phases formed when the A element is chemically etched out leaving behind 2D layers of MX only.[19] As reported by Mahesh et al., the delamination of MAX 2D structures are possible by the micro-mechanical milling of Ti_3SiC_2 in mortar pestle.[20] The compressive forces by the balls on the particles induce mechanical shear along the basal plane resulting in a suspension of MAXene in ethanol which is stable for nearly 1 month. Such suspensions can be used for efficient heat transfer in thermal fluids. A recent research interest has been growing in the field of 2D structures obtained from MAX phases and the possible application include Li-ion and Na-ion batteries, supercapacitors, gas separation membranes, reinforcements in polymers and in cancer therapy as well.[20–24]

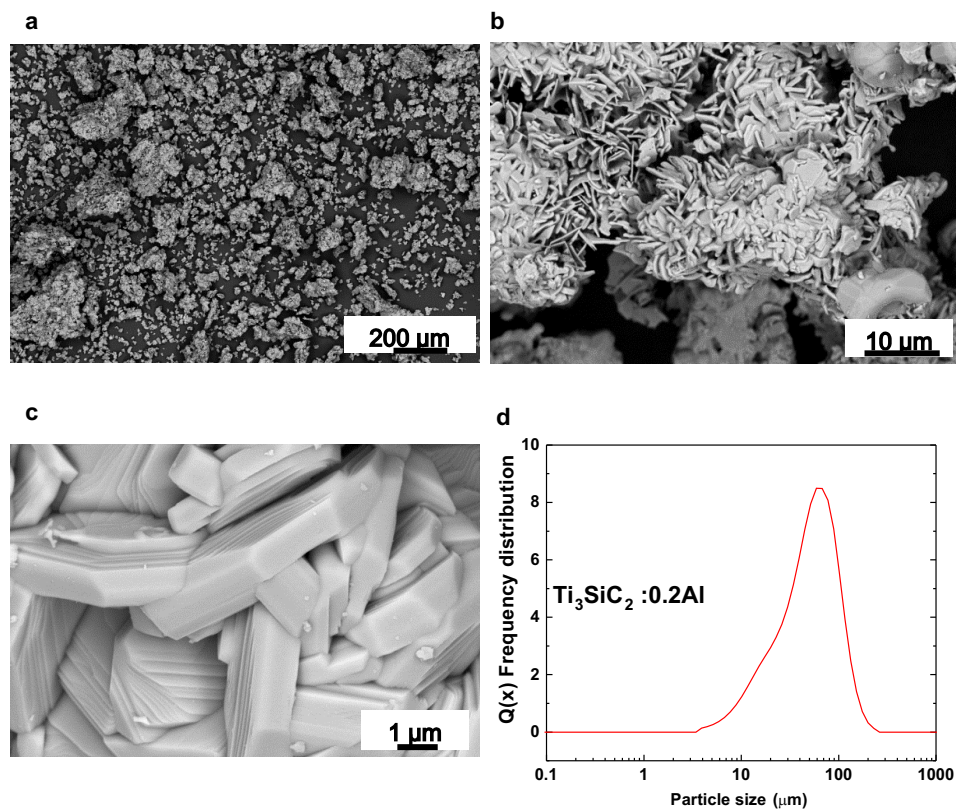


Figure 4.18: Morphology of synthesized Ti₃SiC₂:0.2Al **a,b,c** at different magnification and **d** the particle size distribution.

4.5. SYNTHESIS OF OTHER NON-OXIDE CERAMIC POWDERS

MS³ process opens up an avenue for cheap synthesis of high purity MAX phases/non-oxide ceramics and the sintering of metals in air. The process developed herein does not need any expensive equipment like vacuum furnace, hot isostatic pressing, spark plasma sintering furnace or atmosphere-controlled furnace which requires an uninterrupted flow of argon or any inert gas to prevent oxidation.[18, 25–30] MS³ enables us to obtain free powder by just dissolving the heat-treated samples in water. The solubility of KBr in water is 1020 g/L at 100 °C.[31] Hence production of 1 kg of MAX phase would need approximately 1 L of boiling water to dissolve the salt content. Further washing to ensure the complete removal of the salt which requires an extra 2 L of water. An average estimate of 3 L of water is required to produce 1 kg of MAX phase. The salt recovered from the saline water can be reused in the MS³ process.

The use of molten salt further reduces the synthesis temperature resulting in additional cost reduction. The milling of MAX phase imposes safety threats because of the energy intensive comminution process which might result in the self-ignition of MAX phase.

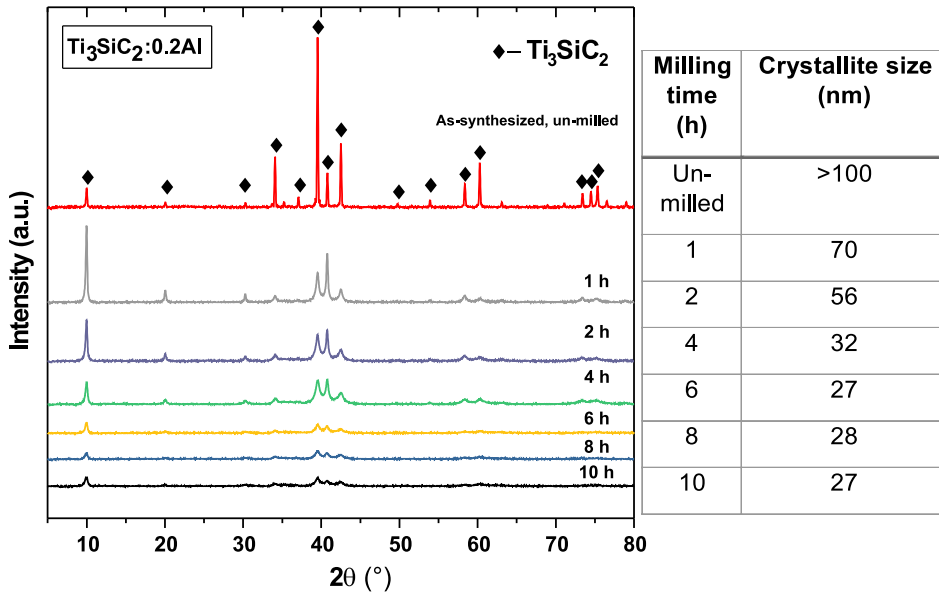
Figure 4.19: XRD of synthesized $\text{Ti}_3\text{SiC}_2:0.2\text{Al}$ with increasing milling time.

Table 4.5: A comparison of detected phases of Ti/Si/C with and without Al w.r.t. temperature (* denotes traces)

Temperature (°C)	Detected phases (XRD)	Detected phases (XRD)
	TSC	TSA0.2C
700	Ti, Si, C	Ti, Si, C
800	Ti_5Si_3 , Si, Ti, C, TiSi_2 , TiC	Ti_5Si_3 , Si, Ti, C, TiAl_3 , TiC
900	Ti_5Si_3 , TiC, C, Ti	Ti_5Si_3 , TiC, C, TiAl_3
1000	Ti_5Si_3 (57%), C*, TiC (43%), Ti_3SiC_2 *	Ti_5Si_3 (68%), C*, TiC (32%), TiAl_3 , Ti, Ti_3SiC_2 *
1100	Ti_5Si_3 (53%), TiC (47%), C*, Ti_3SiC_2 *	Ti_5Si_3 (53%), TiC (42%), C*, Ti_3SiC_2 (5%)
1200	Ti_5Si_3 (41%), TiC (34%), C*, Ti_3SiC_2 (25%)	Ti_5Si_3 (18%), TiC (11%), C*, Ti_3SiC_2 (71%)
1300	Ti_5Si_3 (10%), TiC (22%), C*, TiSi_2 (7%), Ti_3SiC_2 (61%)	C*, TiC (4%), Ti_3SiC_2 (96%)

The sintering of titanium in air is a demonstration of the fact that metals can be sintered in air without oxidation. The cost of powder metallurgical component is mainly due to the heat treatment. MS^3 makes the high temperature processing step cheaper and provides a possibility for the fabrication of more economical components.

As MS^3 impedes oxidation of non-oxide materials; highly pure (XRD) Ti_2AlN was also synthesized by MS^3 process. Nitrogen containing compounds normally need a N_2 par-

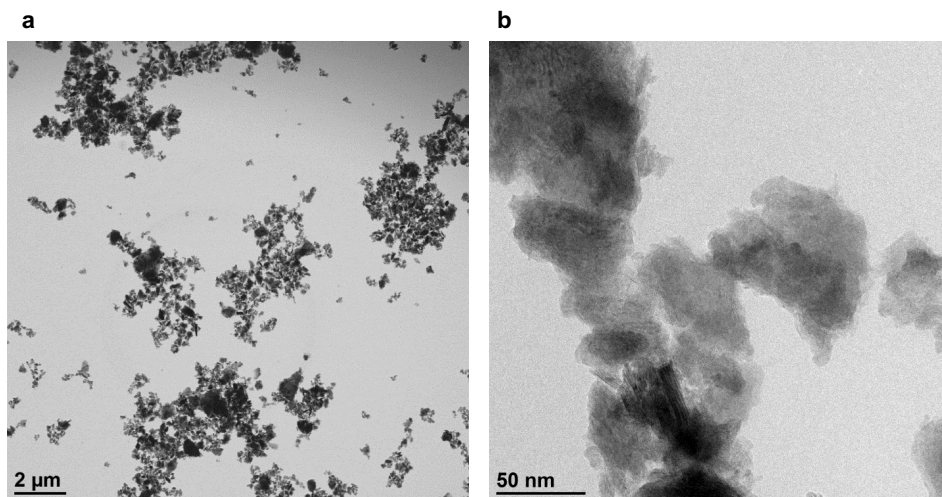


Figure 4.20: TEM of synthesized Ti_3SiC_2 milled for 6 h at different magnification.

tial pressure to prevent the outgassing of nitrogen from the material. $MoAlB$, was synthesized with MoB_2 as the second phase for the proof of concept. The powder morphology and the characteristic layered structure of damage tolerant phases are shown in Fig.4.21-4.23. It is noteworthy that none of the material has oxides as the secondary phases as detected by XRD.

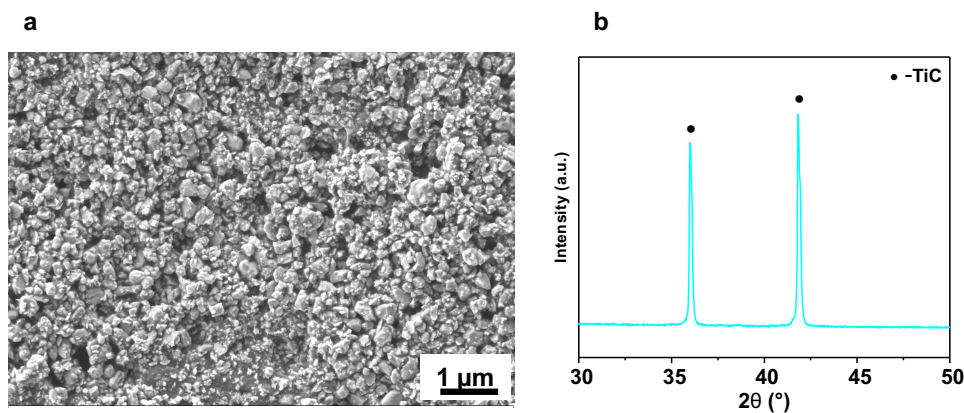


Figure 4.21: TiC synthesized by MS^3 **a** powder morphology **b** XRD.

A multitude of compounds were synthesized including Cr_2AlB_2 [32], Ti_4AlN_3 [33], Mo_2TiAlC_2 [34], Ti_2AlC [35], Ti_3AlC_2 [35], Cr_2AlC [36] and many more but it is not feasible to report all the synthesis experiments with details.

MS^3 process cuts down the milling step required to pulverize dense blocks into micron-

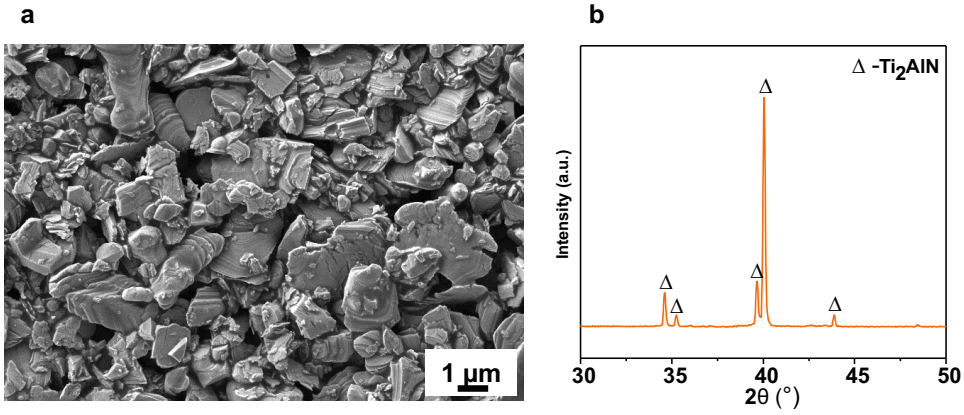


Figure 4.22: Ti₂AlN synthesized by MS³ **a** powder morphology **b** XRD.

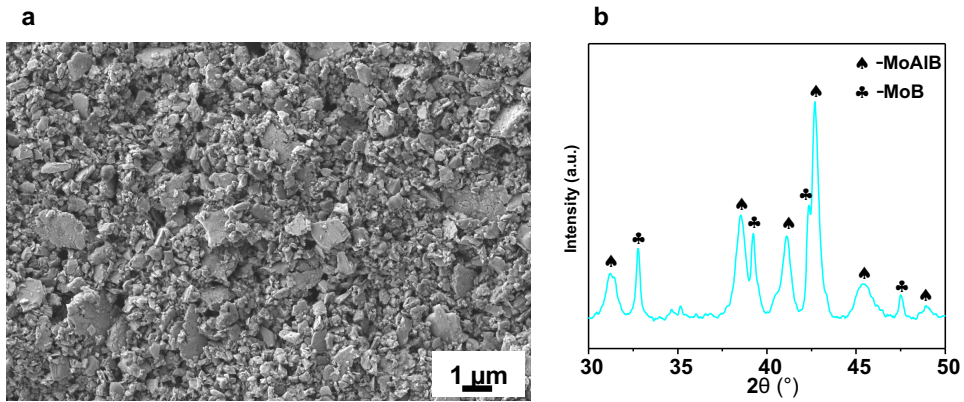


Figure 4.23: MoAlB synthesized by MS³ **a** powder morphology **b** XRD.

sized powder for further fabrication of complex shapes by slip casting [37], tape casting [38], injection moulding [39], additive manufacturing [40] or any other powder metallurgical operations.

Fig.4.24 shows the purity of all MAX phases synthesized by MS³ and other processing routes along with the attributes (lower synthesis temperature and higher purity) of MS³ as compared to conventional processing routes.

MS³ process can be industrially scaled-up by simply increasing the batch size or making the process continuous. Successful trials have been made with a batch size of 500 g for the powder production of Ti₃SiC₂ MAX phase. The sintering of metals via powder metallurgy is also industrially scalable by modifying the process. MS³ can be regarded as an environmentally friendly process because the salts when used in the proper temperature window are not volatile and harmful. Moreover, recycling of the salt is also possible, further making the process sustainable. MS³ opens therefore a new direction for the syn-

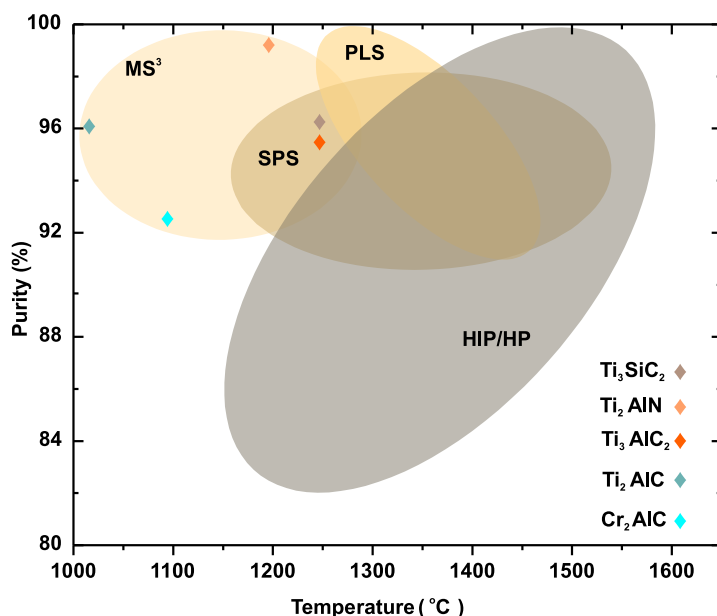


Figure 4.24: Purity vs. synthesis temperature of various MAX phases by different processing routes: Spark Plasma Sintering (SPS), Pressure-Less Sintering (PLS), Hot Isostatic Pressing/Hot Pressing (HIP/HP) (see Table 4.6 for details of the purity and synthesis temperature by conventional processing routes). The purity of the synthesized phases can be further enhanced by optimizing the ratio of the precursors. The aim of the present work is to demonstrate the possibility of synthesizing a wide range of materials at a relatively low temperature in air.

thesis of non-oxide ceramic powders and the sintering of metals in air.

Since processing non-oxide ceramics was possible with MS^3 route. The sintering of Ti was also carried to demonstrate that the sintering of Ti is possible in air without any oxidation. MS^3 sintered Ti was polished and the characteristic luster of metal is shown in Fig.4.25.b. The density of the sintered titanium was measured to be 4.27 g/cm^3 (94% relative density). It was also possible to produce Ti with 70% porosity using KBr as water soluble space holder particles. Fig.4.25.a and 4.26.a shows the microstructure of the sintered dense and porous titanium respectively, revealing no second phase apart from pores. The sintering of titanium both in dense and porous forms has been achieved in an air furnace.

4.6. SINTERING OF Ti BY MS^3 PROCESS

Existing methods for the fabrication of porous Ti [65] includes sacrificial wax method along with rapid prototyping [66], selective laser melting [67], solid state foaming [68], space holder technique [69] or simply incomplete sintering [70]. Irrespective of the method, the sintering of porous titanium is carried out in vacuum or argon atmosphere.

Table 4.6: Summary of the synthesis temperature and purity of phases obtained by conventional processing routes

Research group	Material	Synthesis method	Temperature (°C)	Purity (XRD based)
Barsoum et al. [41]	Ti ₃ SiC ₂	HIP	1600	98 wt. %
Gao et al. [42]	Ti ₃ SiC ₂	HIP	1500	97 vol. %
Lis et al. [43]	Ti ₃ SiC ₂	HIP	1400	82 vol. %
Sun et al. [44]	Ti ₃ SiC ₂	HP	1550	93 wt. %
Radhakrishnan et al. [17]	Ti ₃ SiC ₂	PLS	1350	98.7 vol. %
Li et al. [45]	Ti ₃ SiC ₂	PLS	1450	93 vol. %
Sun et al. [44]	Ti ₃ SiC ₂	PLS	1250	99 vol. %
Zhang et al. [46]	Ti ₃ SiC ₂	SPS	1350	92 wt. %
Gao et al. [27]	Ti ₃ SiC ₂	SPS	1300	98 wt. %
Feng et al. [47]	Ti ₃ SiC ₂	SPS	1525	98 wt. %
Barsoum et al. [25]	Ti ₂ AlN	HIP	1400	85 vol. %
Ming et al. [48]	Ti ₂ AlN	HP	1300	Single phase
Lin et al. [49]	Ti ₂ AlN	HP	1400	Single phase
Cui et al. [50]	Ti ₂ AlN	SPS	1300	99 wt. %
Ming et al. [51]	Ti ₂ AlN	SPS	1200	Single phase
Kota et al. [52]	MoAlB	HP	1200	91 vol. %
Xu et al. [53]	MoAlB	HP	1100	96 wt. %
Tian et al. [36]	Cr ₂ AlC	HP	1400	95 wt. %
Xiao et al. [54]	Cr ₂ AlC	HP	1400	Not reported
Ying et al. [55]	Cr ₂ AlC	HP	1400	Single phase
Tian et al. [56]	Cr ₂ AlC	SPS	1400	99 wt. %
Tian et al. [57]	Cr ₂ AlC	SPS	1250	Highly pure
Panigrahi et al. [58]	Cr ₂ AlC	PLS	1350	Highly pure
Barsoum et al. [25]	Ti ₂ AlC	HIP	1300	Single phase
Barsoum et al. [59]	Ti ₂ AlC	HP	1600	Single phase
Zhou et al. [60]	Ti ₂ AlC	SPS	1100	Single phase
Gauthier et al. [61]	Ti ₂ AlC	PLS	1400	Single phase
Tzenov et al. [29]	Ti ₃ AlC ₂	HIP	1400	96 vol. %
Wang et al. [62]	Ti ₃ AlC ₂	HP	1500	Single phase
Zou et al. [63]	Ti ₃ AlC ₂	SPS	1400	Single phase
Peng et al. [64]	Ti ₃ AlC ₂	PLS	1300	97 wt. %

In certain methods, the polymer used in the process is burnt and is irrecoverable. In view of the initial investment for laser processing or rapid prototyping, MS³ process is cheaper considering the usage of air furnace alone and the fact that the salt particles which are used as pore formers can be recycled. Considering Ti as one of the most oxidation prone metals, it can be assumed that MS³ provides the possibility to sinter metals both in its dense and porous form in an air furnace.

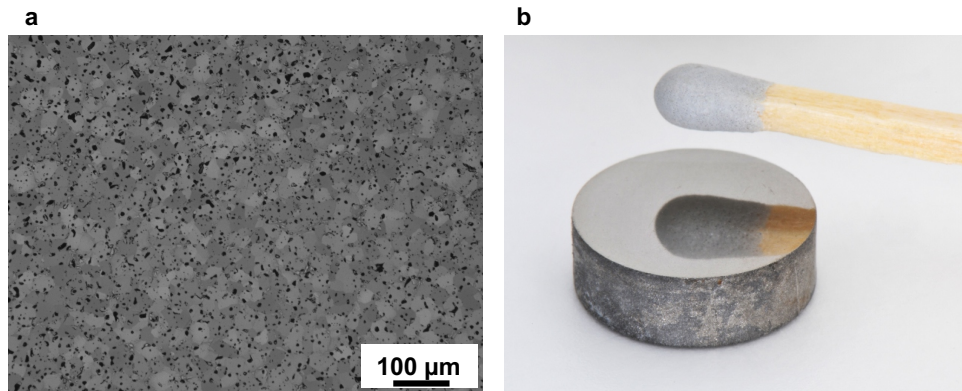


Figure 4.25: **a** Microstructure of Ti sintered by MS³ process, **b** photograph of sintered Ti (note the reflection of the matchstick).

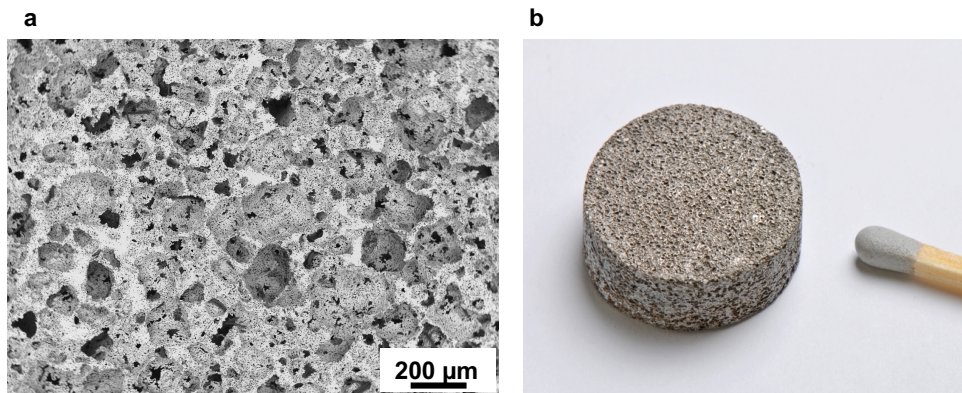


Figure 4.26: **a** Microstructure of porous Ti fabricated by MS³ process, **b** photograph of porous Ti.

REFERENCES

- [1] A. Dash, R. Vaßen, O. Guillon, and J. Gonzalez-Julian, *Molten salt shielded synthesis of oxidation prone materials in air*, *Nature materials* **18**, 465 (2019).
- [2] A. Dash, Y. J. Sohn, R. Vaßen, O. Guillon, and J. Gonzalez-Julian, *Synthesis of Ti₃SiC₂ MAX phase powder by a molten salt shielded synthesis (MS³) method in air*, *Journal of the European Ceramic Society* **39**, 3651 (2019).
- [3] T. Kimura, *Molten salt synthesis of ceramic powders*, *Advances in ceramics-synthesis and characterization, processing and specific applications*, 75 (2011).
- [4] Y. G. Gogotsi and R. A. Andrievski, *Materials science of carbides, nitrides and borides*, Vol. 68 (Springer Science & Business Media, 2012).

- [5] E. R. Parker, J. Pask, J. Washburn, A. Gorum, and W. Luhman, *Ductile ceramics—a high temperature possibility*, JOM **10**, 351 (1958).
- [6] A. Gorum, E. Parker, and J. Pask, *Effect of surface conditions on room-temperature ductility of ionic crystals*, Journal of the American Ceramic Society **41**, 161 (1958).
- [7] K. H. Yoon, Y. S. Cho, and D. H. Kang, *Molten salt synthesis of lead-based relaxors*, Journal of materials science **33**, 2977 (1998).
- [8] Q. Wang, J. Song, G. Hu, X. Zhu, J. Hou, S. Jiao, and H. Zhu, *The equilibrium between titanium ions and titanium metal in NaCl-KCl equimolar molten salt*, Metallurgical and Materials Transactions B **44**, 906 (2013).
- [9] A. Selloni, P. Carnevali, R. Car, and M. Parrinello, *Localization, hopping, and diffusion of electrons in molten salts*, Physical review letters **59**, 823 (1987).
- [10] X. Liu, N. Fechner, and M. Antonietti, *Salt melt synthesis of ceramics, semiconductors and carbon nanostructures*, Chemical Society Reviews **42**, 8237 (2013).
- [11] G. J. Janz, *Molten salts handbook* (Elsevier, 2013).
- [12] T. El-Raghy and M. W. Barsoum, *Diffusion kinetics of the carburization and silicidation of Ti_3SiC_2* , Journal of Applied Physics **83**, 112 (1998).
- [13] J. M. Córdoba, M. J. Sayagués, M. D. Alcalá, and F. J. Gotor, *Synthesis of Ti_3SiC_2 powders: reaction mechanism*, Journal of the American Ceramic Society **90**, 825 (2007).
- [14] T. El-Raghy, M. W. Barsoum, A. Zavaliangos, and S. R. Kalidindi, *Processing and mechanical properties of Ti_3SiC_2 : II, effect of grain size and deformation temperature*, Journal of the American ceramic society **82**, 2855 (1999).
- [15] H. Zhang, Y. Zhou, Y. Bao, M. Li, and J. Wang, *Intermediate phases in synthesis of Ti_3SiC_2 and Ti_3SiAlC_2 solid solutions from elemental powders*, Journal of the European Ceramic Society **26**, 2373 (2006).
- [16] N. Welham, *Mechanical activation of the solid-state reaction between Al and TiO_2* , Materials Science and Engineering: A **255**, 81 (1998).
- [17] R. Radhakrishnan, J. Williams, and M. Akinc, *Synthesis and high-temperature stability of Ti_3SiC_2* , Journal of Alloys and Compounds **285**, 85 (1999).
- [18] X. Guo, J. Wang, S. Yang, L. Gao, and B. Qian, *Preparation of Ti_3SiC_2 powders by the molten salt method*, Materials Letters **111**, 211 (2013).
- [19] M. Ghidui, M. R. Lukatskaya, M.-Q. Zhao, Y. Gogotsi, and M. W. Barsoum, *Conductive two-dimensional titanium carbide ‘clay’ with high volumetric capacitance*, Nature **516**, 78 (2014).
- [20] K. Mahesh, V. Linsha, A. P. Mohamed, and S. Ananthakumar, *Processing of 2D-MAXene nanostructures and design of high thermal conducting, rheo-controlled MAXene nanofluids as a potential nanocoolant*, Chemical Engineering Journal **297**, 158 (2016).

- [21] K. Mahesh, R. Rashada, M. Kiran, A. P. Mohamed, and S. Ananthakumar, *Shear induced micromechanical synthesis of Ti_3SiC_2 MAXene nanosheets for functional applications*, RSC advances **5**, 51242 (2015).
- [22] L. Ding, Y. Wei, L. Li, T. Zhang, H. Wang, J. Xue, L.-X. Ding, S. Wang, J. Caro, and Y. Gogotsi, *MXene molecular sieving membranes for highly efficient gas separation*, Nature communications **9**, 1 (2018).
- [23] X. Wang, T. S. Mathis, K. Li, Z. Lin, L. Vlcek, T. Torita, N. C. Osti, C. Hatter, P. Urbankowski, A. Sarycheva, *et al.*, *Influences from solvents on charge storage in titanium carbide MXenes*, Nature Energy **4**, 241 (2019).
- [24] L. Cheng, X. Wang, F. Gong, T. Liu, and Z. Liu, *2D nanomaterials for cancer theranostic applications*, Advanced Materials **32**, 1902333 (2020).
- [25] M. Barsoum, T. El-Raghy, and M. Ali, *Processing and characterization of Ti_2AlC , Ti_2AlN and $Ti_2AlC_{0.5}N_{0.5}$* , Metallurgical and Materials Transactions A **31**, 1857 (2000).
- [26] Y. Zhou and Z. Sun, *Temperature fluctuation/hot pressing synthesis of Ti_3SiC_2* , Journal of materials science **35**, 4343 (2000).
- [27] N. Gao, J. Li, D. Zhang, and Y. Miyamoto, *Rapid synthesis of dense Ti_3SiC_2 by spark plasma sintering*, Journal of the European Ceramic Society **22**, 2365 (2002).
- [28] W.-B. Tian, P.-L. Wang, Y.-M. Kan, and G.-J. Zhang, *Cr_2AlC powders prepared by molten salt method*, Journal of alloys and compounds **461**, L5 (2008).
- [29] N. V. Tzenov and M. W. Barsoum, *Synthesis and characterization of Ti_3AlC_2* , Journal of the American Ceramic Society **83**, 825 (2000).
- [30] Z. Zhang, Z. Sun, and H. Hashimoto, *Rapid synthesis of ternary carbide Ti_3SiC_2 through pulse-discharge sintering technique from Ti/Si/TiC powders*, Metallurgical and Materials Transactions A **33**, 3321 (2002).
- [31] S. Pinho and E. A. Macedo, *Experimental measurement and modelling of kbr solubility in water, methanol, ethanol, and its binary mixed solvents at different temperatures*, The Journal of Chemical Thermodynamics **34**, 337 (2002).
- [32] M. Ade and H. Hillebrecht, *Ternary borides Cr_2AlB_2 , Cr_3AlB_4 , and Cr_4AlB_6 : The first members of the series $(CrB_2)_nCrAl$ with $n= 1, 2, 3$ and a unifying concept for ternary borides as *mab*-phases*, Inorganic chemistry **54**, 6122 (2015).
- [33] C. Rawn, M. Barsoum, T. El-Raghy, A. Procipio, C. Hoffmann, and C. Hubbard, *Structure of Ti_4AlN_3 —A layered $M_{n+1}AX_n$ nitride*, Materials research bulletin **35**, 1785 (2000).
- [34] B. Anasori, J. Halim, J. Lu, C. A. Voigt, L. Hultman, and M. W. Barsoum, *Mo_2TiAlC_2 : A new ordered layered ternary carbide*, Scripta Materialia **101**, 5 (2015).

- [35] X. Wang and Y. Zhou, *Layered machinable and electrically conductive Ti_2AlC and Ti_3AlC_2 ceramics: a review*, Journal of Materials Science & Technology **26**, 385 (2010).
- [36] W. Tian, P. Wang, G. Zhang, Y. Kan, Y. Li, and D. Yan, *Synthesis and thermal and electrical properties of bulk Cr_2AlC* , Scripta Materialia **54**, 841 (2006).
- [37] C. Hu, Y. Sakka, H. Tanaka, T. Nishimura, and S. Grasso, *Fabrication of textured Nb_4AlC_3 ceramic by slip casting in a strong magnetic field and spark plasma sintering*, Journal of the American Ceramic Society **94**, 410 (2011).
- [38] A. Murugaiah, A. Souchet, T. El-Raghy, M. Radovic, M. Sundberg, and M. Barsoum, *Tape casting, pressureless sintering, and grain growth in Ti_3SiC_2 compacts*, Journal of the American Ceramic Society **87**, 550 (2004).
- [39] J. Gonzalez-Julian, L. Classen, M. Bram, R. Vaßen, and O. Guillon, *Near net shaping of monolithic and composite MAX phases by injection molding*, Journal of the American Ceramic Society **99**, 3210 (2016).
- [40] B. Nan, X. Yin, L. Zhang, and L. Cheng, *Three-dimensional printing of Ti_3SiC_2 -based ceramics*, Journal of the American Ceramic Society **94**, 969 (2011).
- [41] M. W. Barsoum and T. El-Raghy, *Synthesis and characterization of a remarkable ceramic: Ti_3SiC_2* , Journal of the American Ceramic Society **79**, 1953 (1996).
- [42] N. Gao, Y. Miyamoto, and D. Zhang, *Dense Ti_3SiC_2 prepared by reactive HIP*, Journal of materials science **34**, 4385 (1999).
- [43] J. Lis, R. Pampuch, J. Piekarczyk, and L. Stobierski, *New ceramics based on Ti_3SiC_2* , Ceramics International **19**, 219 (1993).
- [44] Z. Sun, S. Yang, and H. Hashimoto, *Ti_3SiC_2 powder synthesis*, Ceramics International **30**, 1873 (2004).
- [45] H. Li, L. Peng, M. Gong, J. Zhao, L. He, and C. Guo, *Preparation and characterization of Ti_3SiC_2 powder*, Ceramics International **30**, 2289 (2004).
- [46] Z. Zhang, Z. Sun, H. Hashimoto, and T. Abe, *A new synthesis reaction of Ti_3SiC_2 through pulse discharge sintering $Ti/SiC/TiC$ powder*, Scripta materialia **45**, 1461 (2001).
- [47] A. Feng, T. Orling, and Z. Munir, *Field-activated pressure-assisted combustion synthesis of polycrystalline Ti_3SiC_2* , Journal of materials research **14**, 925 (1999).
- [48] Y. Ming, Y.-l. Chen, B.-c. Mei, and J.-q. Zhu, *Synthesis of high-purity Ti_2AlN ceramic by hot pressing*, Transactions of Nonferrous Metals Society of China **18**, 82 (2008).
- [49] Z. Lin, M. Zhuo, M. Li, J. Wang, and Y. Zhou, *Synthesis and microstructure of layered-ternary Ti_2AlN ceramic*, Scripta materialia **56**, 1115 (2007).

- [50] B. Cui, R. Sa, D. D. Jayaseelan, F. Inam, M. J. Reece, and W. E. Lee, *Microstructural evolution during high-temperature oxidation of spark plasma sintered Ti₂AlN ceramics*, *Acta Materialia* **60**, 1079 (2012).
- [51] M. Yan, B. Mei, J. Zhu, C. Tian, and P. Wang, *Synthesis of high-purity bulk Ti₂AlN by spark plasma sintering (SPS)*, *Ceramics International* **34**, 1439 (2008).
- [52] S. Kota, E. Zapata-Solvas, A. Ly, J. Lu, O. Elkassabany, A. Huon, W. E. Lee, L. Hultman, S. J. May, and M. W. Barsoum, *Synthesis and characterization of an alumina forming nanolaminated boride: MoAlB*, *Scientific reports* **6**, 1 (2016).
- [53] L. Xu, O. Shi, C. Liu, D. Zhu, S. Grasso, and C. Hu, *Synthesis, microstructure and properties of MoAlB ceramics*, *Ceramics International* **44**, 13396 (2018).
- [54] L.-O. Xiao, S.-B. Li, G. Song, and W. G. Sloof, *Synthesis and thermal stability of Cr₂AlC*, *Journal of the European Ceramic Society* **31**, 1497 (2011).
- [55] G. Ying, X. He, M. Li, W. Han, F. He, and S. Du, *Synthesis and mechanical properties of high-purity Cr₂AlC ceramic*, *Materials Science and Engineering: A* **528**, 2635 (2011).
- [56] W. Tian, K. Vanmeensel, P. Wang, G. Zhang, Y. Li, J. Vleugels, and O. Van der Biest, *Synthesis and characterization of Cr₂AlC ceramics prepared by spark plasma sintering*, *Materials Letters* **61**, 4442 (2007).
- [57] W. Tian, Z. Sun, Y. Du, and H. Hashimoto, *Synthesis reactions of Cr₂AlC from Cr-Al₄C₃-C by pulse discharge sintering*, *Materials Letters* **62**, 3852 (2008).
- [58] B. B. Panigrahi, M.-C. Chu, Y.-I. Kim, S.-J. Cho, and J. J. Gracio, *Reaction synthesis and pressureless sintering of Cr₂AlC powder*, *Journal of the American Ceramic Society* **93**, 1530 (2010).
- [59] M. W. Barsoum, D. Brodtkin, and T. El-Raghy, *Layered machinable ceramics for high temperature applications*, *Scripta Materialia* **36** (1997).
- [60] W. Zhou, B. Mei, J. Zhu, and X. Hong, *Rapid synthesis of Ti₂AlC by spark plasma sintering technique*, *Materials Letters* **59**, 131 (2005).
- [61] V. Gauthier-Brunet, T. Cabioc'h, P. Chartier, M. Jaouen, and S. Dubois, *Reaction synthesis of layered ternary Ti₂AlC ceramic*, *Journal of the European Ceramic Society* **29**, 187 (2009).
- [62] X. Wang and Y. Zhou, *Solid-liquid reaction synthesis of layered machinable Ti₃AlC₂ ceramic*, *Journal of Materials Chemistry* **12**, 455 (2002).
- [63] Y. Zou, Z. Sun, S. Tada, and H. Hashimoto, *Synthesis reactions for Ti₃AlC₂ through pulse discharge sintering Ti/Al₄C₃/TiC powder mixture*, *Scripta materialia* **55**, 767 (2006).

- [64] C. Peng, C.-A. Wang, Y. Song, and Y. Huang, *A novel simple method to stably synthesize Ti_3AlC_2 powder with high purity*, *Materials Science and Engineering: A* **428**, 54 (2006).
- [65] D. C. Dunand, *Processing of titanium foams*, *Advanced engineering materials* **6**, 369 (2004).
- [66] G. E. Ryan, A. S. Pandit, and D. P. Apatsidis, *Porous titanium scaffolds fabricated using a rapid prototyping and powder metallurgy technique*, *Biomaterials* **29**, 3625 (2008).
- [67] W. Xue, B. V. Krishna, A. Bandyopadhyay, and S. Bose, *Processing and biocompatibility evaluation of laser processed porous titanium*, *Acta biomaterialia* **3**, 1007 (2007).
- [68] N. Davis, J. Teisen, C. Schuh, and D. Dunand, *Solid-state foaming of titanium by superplastic expansion of argon-filled pores*, *Journal of Materials Research* **16**, 1508 (2001).
- [69] Y. Torres, J. Pavón, and J. Rodríguez, *Processing and characterization of porous titanium for implants by using NaCl as space holder*, *Journal of Materials Processing Technology* **212**, 1061 (2012).
- [70] I.-H. Oh, N. Nomura, N. Masahashi, and S. Hanada, *Mechanical properties of porous titanium compacts prepared by powder sintering*, *Scripta Materialia* **49**, 1197 (2003).

5

RESULTS & DISCUSSIONS II

Processing of Ti_3SiC_2 composites containing SiC whiskers and short SiC fibers

IN the present work, CMC is being manufactured by powder metallurgy route. CMC with Ti_3SiC_2 MAX phase as the matrix were sintered with different content of (i) chopped Hi-Nicalon SiC fiber (SiC_f , length 1 mm, Ø 10 μm , density: 2.6 g/cm^3) and (ii) SiC whiskers (SiC_w , length 10 μm , Ø 1 μm , density: 2.74 g/cm^3). Whereas, monolithic Ti_3SiC_2 were sintered as blank specimen to be used as a reference for the CMCs fabricated. The following Table 5.1 shows the nomenclature of the CMCs with varying volume fraction of SiC_f and SiC_w .

Table 5.1: Nomenclature and sintered density of ceramic matrix composites

Vol.% of reinforcement	Sample ID	Theoretical Density (g/cm^3)	Sintered Density (g/cm^3)	Relative Density (%)
0	TSC	4.5	4.46	99.20
10 vol.% SiC whiskers	TSC-10 SiC_w	4.324	4.3	99.44
20 vol.% SiC whiskers	TSC-20 SiC_w	4.148	4.21	101
10 vol.% SiC fiber	TSC-10 SiC_f	4.31	4.27	99.04
20 vol.% SiC fiber	TSC-20 SiC_f	4.13	3.73	90.1

Table 5.1 shows the density of the CMCs fabricated as compared to the theoretical densities considering the volume fractions of corresponding SiC_w and SiC_f . The densities of all the composites are nearly 100% of the theoretical value except for TSC-20 SiC_f because of which it was not considered for further high temperature mechanical testing.

Parts of this chapter have been published in Journal of American Ceramic Society **103**, 5952 (2020) and **103**, 7072 (2020) [1, 2].

The relative density of TSC-20 SiC_w is slightly higher than 100% because of probable reaction of residual $TiSi_2$ with SiC_w resulting in Ti_3SiC_2 . This is shown further in the present chapter that pure TSC has traces of $TiSi_2$ whereas TSC-20 SiC_w does not have any $TiSi_2$ content and can be related to the reaction with SiC_w resulting in Ti_3SiC_2 .

5.1. CHARACTERIZATION OF SPARK PLASMA SINTERED MONOLITHIC Ti_3SiC_2

Ti_3SiC_2 was sintered without any reinforcements to be used as reference for the CMCs with SiC_f and SiC_w . Ti_3SiC_2 was sintered from the molten salt synthesized powder by pressure assisted consolidation in spark plasma sintering furnace at 1250 °C for 15 min under uniaxial pressure of 80 MPa.

SCANNING ELECTRON MICROSCOPY

5

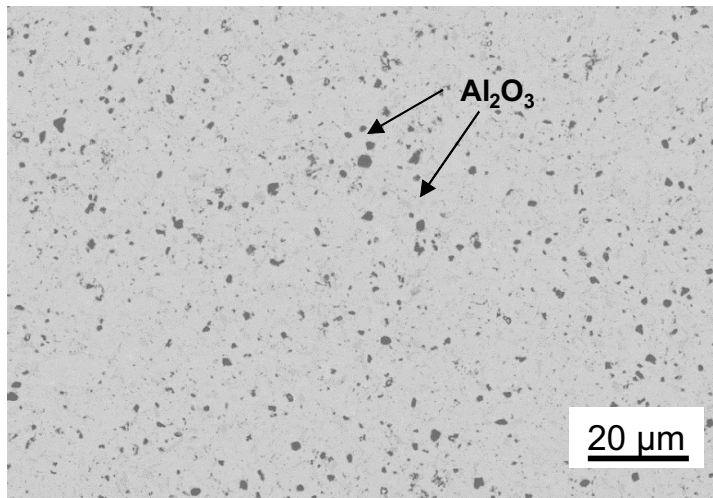


Figure 5.1: Backscattered electron micrograph of SPS sintered Ti_3SiC_2 .

Fig.5.1 shows the polished top surface of dense Ti_3SiC_2 sintered in SPS at 1250 °C for 15 minutes under a uniaxial pressure of 80 MPa. The microstructure reveals that there are no pores and the material is completely dense. The measurement of density by Archimedes method of water displacement yielded results above the 99% of the theoretical density. The backscattered image shows the phase contrast with different shades of grey. Energy dispersive spectroscopy (EDS, Fig.5.2) performed over a high magnification micrograph on various points reveal the probable phases present in the sintered Ti_3SiC_2 .

The sintered material is composed of Ti_3SiC_2 , TiC and alumina as confirmed from the XRD analysis of the sintered material. The EDS point analysis provides further evidence to the presence of alumina which was calculated to be 5.7 vol.% by image analysis of a low magnification microstructure. Table 5.2 shows the probable phase estimation from

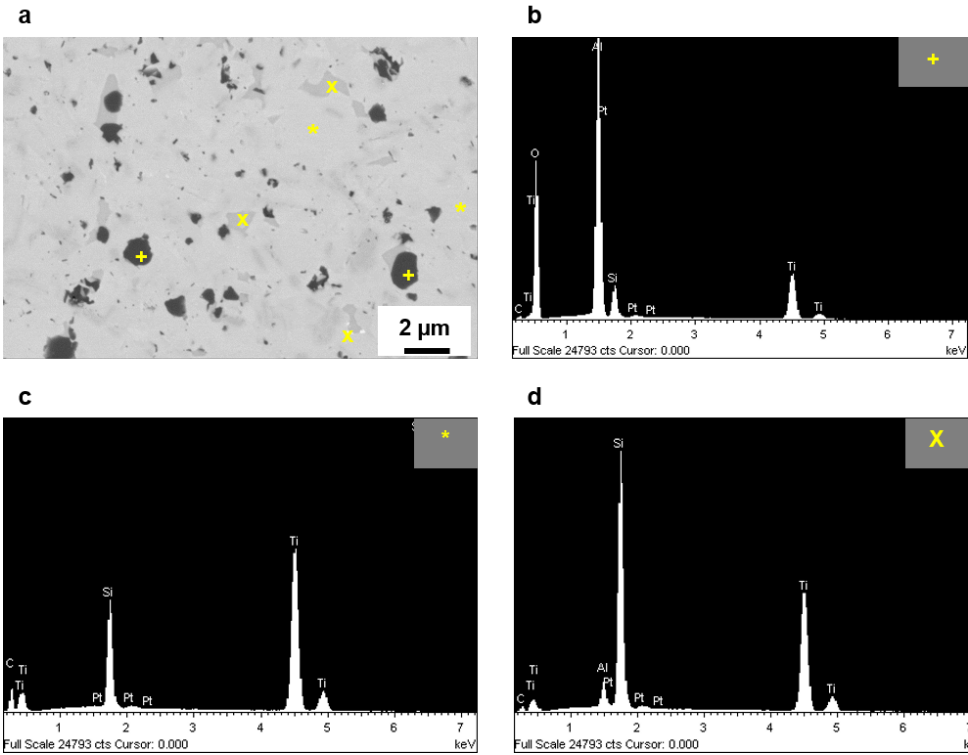


Figure 5.2: SEM-EDS investigation on the polished surface of sintered Ti_3SiC_2 , **a** high magnification backscattered micrograph, **b c d** EDS plot corresponding to the points represented in **a**.

the data obtained by EDS point analysis.

Table 5.2: Possible phases identified by EDS spectra correlated to the phase contrast

Phase contrast	EDS peaks (S: strong, W: weak)	Probable phase
Light grey (*)	Ti(s), Si(s), Al(w)	Ti_3SiC_2
Dark grey (X)	Ti(s), Si(s), Al(w)	Ti_3SiC_2 (orientation contrast)
Black (+)	Ti(w), Al(s), Si(w), O(s)	Al_2O_3

Fig.5.3 shows the XRD pattern of the synthesized powder and the sintered pellet. TiC peaks are visible which might be related to the loss of silicon due to the high vacuum during the sintering process. The wt.% of TiC and Al_2O_3 is 8.8% and 4.6% by Rietveld analysis, respectively, in the SPS sintered Ti_3SiC_2 . The presence of Al_2O_3 is due to the use of Al as a reaction additive during the molten salt synthesis of Ti_3SiC_2 . The sintered sample has developed texture because of the uniaxial deformation of the powder at high temperature and hence the relative peak intensity ratio has changed. Since the initial powder morphology (Fig.4.18.b) is platelet like, the high temperature consolidation might have caused the platelets to rearrange in an orderly fashion. The calculation of Lotgering Fac-

tor (f_L) will shed more light on the orientation of the Ti_3SiC_2 grains in the sintered pellet.

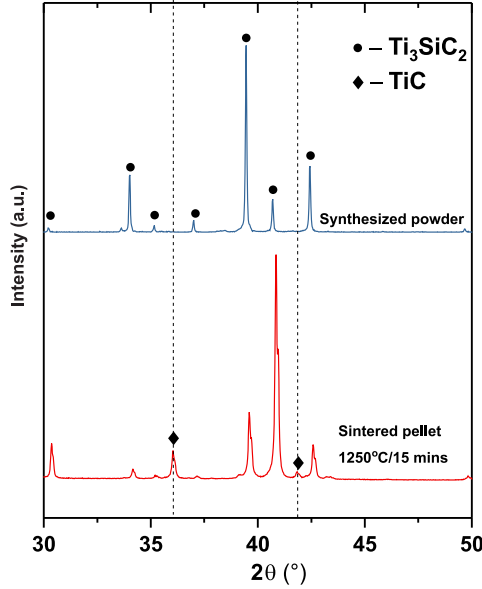


Figure 5.3: XRD pattern of synthesized Ti_3SiC_2 powder and sintered pellet.

LOTGERING FACTOR

Lotgering factor is a measure of the degree of texture in a polycrystalline material according to the relative peak intensity ratios in a XRD diffraction pattern. Since Ti_3SiC_2 is a hexagonal crystal structure, considering a material with perfectly oriented crystals along the $[0001]$ direction, the XRD of the surface normal to the $[0001]$ direction will yield a pattern with no $hkil$ reflections. The XRD pattern will have peaks of planes parallel to $[0001]$ only. If the grains are partially oriented at a small angle with respect to the $[0001]$ direction, the $hkil$ reflections will start appearing and get more intense as the angle of the orientation increases. Hence, the degree of orientation can be approximated by comparing a textured material with that of the randomly oriented crystal orientation. In the present case, the comparison has been made between the spark plasma sintered pellet and the starting powder (which are assumed to be randomly distributed). The Lotgering factor, f_L is given by the following relation:

$$f_L = \frac{(P - P_0)}{(1 - P_0)} \quad (5.1)$$

For a, b axes orientation,

$$P = \frac{\sum I_{hk0}}{\sum I_{hkl}} \quad (5.2)$$

whereas for c axis orientation

$$P = \frac{\sum I_{00l}}{\sum I_{hkl}} \quad (5.3)$$

from the XRD pattern of the textured sample in a given range of 2θ . Similarly, P_0 is calculated using the same formula but for a randomly oriented material. The Lotgering factor for a randomly oriented poly-crystal is 0 and that for a single crystal is 1. Fig.5.4 shows

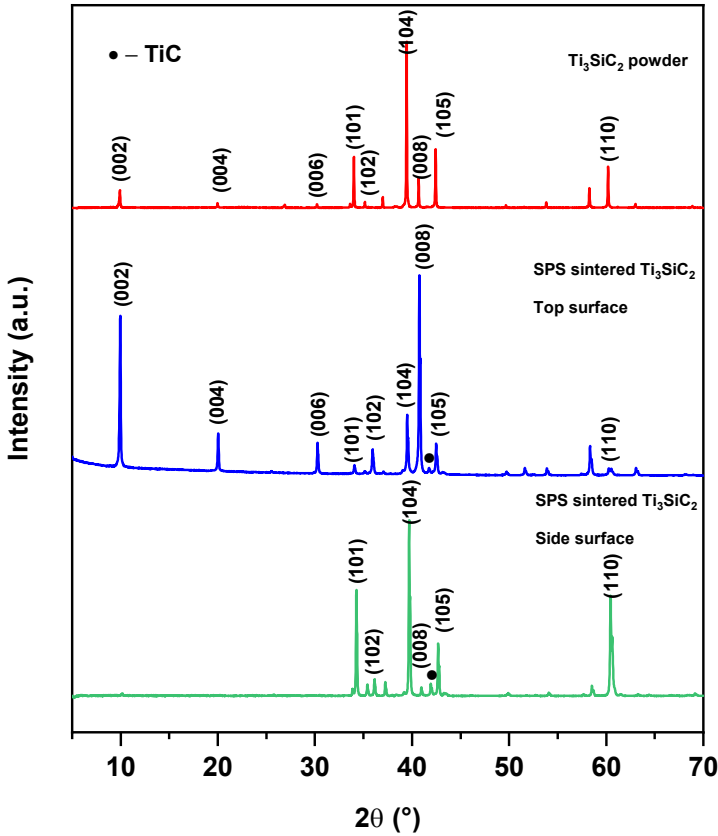


Figure 5.4: XRD pattern of synthesized powder and spark plasma sintered top surface and side surface of Ti_3SiC_2 .

the XRD pattern of the top and side surface of the sintered Ti_3SiC_2 as compared to the starting powder. The initial powder shows a random orientation because of the inherent nature of the powder particles to align in a stochastic manner. The top surface of the sintered Ti_3SiC_2 shows stronger reflections of $(00l)$ planes whereas the (hko) planes become weaker. The side surface of sintered Ti_3SiC_2 has stronger (hko) reflections and weak $(00l)$ peaks. Table 5.3 summarizes the values of P for the calculation of Lotgering factor for the top and side surface.

The degree of orientation for the top surface $f_L(00l)$ and the side surface $f_L(hko)$ were calculated to be 0.78 and 0.88 respectively. The crystal orientation is opposite to

Table 5.3: Intensity summation and P values for the calculation of Lotgering Factor

	Ti_3SiC_2 powder	Top surface	Side surface
ΣI_{00l}	7119	50346	669
ΣI_{hk0}	42047	13905	38561
ΣI_{hkl}	49166	64251	39230
$P_0(00l)$	0.1447	-	-
$P_0(hk0)$	0.8552		
$P(00l)$	-	0.7835	0.0170
$P(hk0)$	-	0.2164	0.9829

that identified by Mishra et al. who oriented the Ti_3SiC_2 particles with the aid of high intensity magnetic field (12 Tesla).[3] The side surface texture is equivalent to the top face texture in the present case and vice versa for the top surface in case of Mishra et al. The $f_L(00l)$ and $f_L(hk0)$ in case of Mishra et al. was 0.75 and 0.35 respectively. The improvement of $f_L(hk0)$ from 0.35 to 0.88 in the present case suggest a higher degree of prismatic texture apart from basal texture which is very evident from high $f_L(00l)$ values. The higher value of $f_L(hk0)$ can also be accounted for the fact that the intensity of equivalent planes like (101) and (104) were also considered.

POLE FIGURE

In hexagonal materials, basal texture is the most common form of preferred orientation. The sintered Ti_3SiC_2 has a strong basal texture. Fig.5.5 shows (008) and (110) pole figure of the top surface of Ti_3SiC_2 . The top surface is a surface perpendicular to the direction of the application of uniaxial pressure during the sintering process. The (008) pole figure is distributed along the normal direction (ND) suggesting the alignment of basal planes along the normal direction (ND) plane. The c/a ratio for Ti_3SiC_2 is 5.759 which is nearly 3.5 times the ideal c/a ratio of 1.633. Although the c/a ratio is very high, the (0002) pole figure represented by (008) pole figures strongly shows basal texture fiber resembling materials with $c/a = 1.633$. Usually, materials with high c/a ratio shows splitting along the RD. This is due to the absence of any other slip system besides basal slip in Ti_3SiC_2 . The process of sintering in ceramics can be compares to that of annealing in metals. Hence, the texture evolution of metals during annealing can be compared to that of sintering in ceramics which results in a low energy configuration of the material.

The $(10\bar{1}0)$ pole figure in combination with (0002) pole figure intensity makes it evident that material has basal texture similar to cold rolled hexagonal metals.[4]

ORIENTATION DISTRIBUTION FUNCTION

Since the information obtained from pole figures are semi-quantitative and incomplete, an orientation distribution function is a way of representation of the orientation of a crystal in a three-dimensional Euler space. The Euler space is defined by three angles (ϕ_1, ϕ, ϕ_2) which are used to rotate the crystal in Z, X and Z' (new Z axis after ϕ_1 and ϕ rotation) axis respectively to coincide with the sample geometry axis. The ϕ_1 was varied

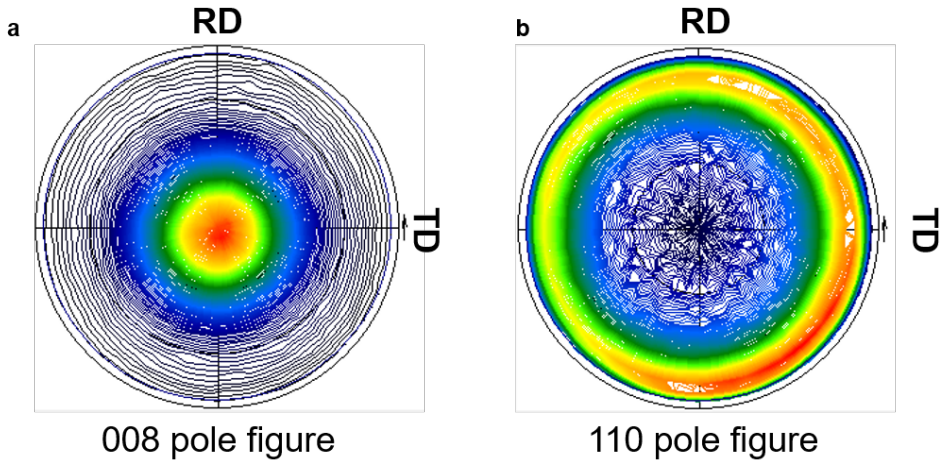


Figure 5.5: Incomplete pole figures of **a** 008 and **b** 110 orientation in normal direction of spark plasma sintered Ti_3SiC_2 , (VIBGYOR intensity scale **a** 0-3460 **b** 0-918).

from 0° to 60° , whereas ϕ was varied from 0° to 90° . For hexagonal crystal systems, there is no direct correlation between ODF and crystal planes and direction. Hence a conversion of hexagonal to cubic system is necessary.[4] Table 5.4 shows the main texture components for hexagonal materials with constant ϕ_2 and ϕ sections. The convention used for defining the Euler space was Bunge notation.

Table 5.4: Common texture components for hexagonal material in the Bunge convention

Texture component	ϕ_2 ($^\circ$)	ϕ ($^\circ$)	ϕ_1 ($^\circ$)
Basal fiber $\{0001\}$	0-60	0	0-90
Fiber $\{10\bar{1}0\}$	30	90	0-90
Fiber $\{11\bar{2}0\}$	0/60	90	0-90
$\{0001\} \langle 10\bar{1}0 \rangle$	0/60	0	0,60
$\{0001\} \langle 11\bar{2}0 \rangle$	0/30	0	0,60/0,90

The ODF shown in Fig.5.6 matches with the Basal fiber 0001 texture component and hence the sintered Ti_3SiC_2 has the same texture component. The significant texturing of Ti_3SiC_2 by just sintering free powders in SPS is reported for the first time. Mishra et al and Hu et al. used very strong magnetic field (12 Tesla) and the aid of slip casting to have a liquid medium to ease the rotation of Ti_3SiC_2 particles.[3, 5, 6] As compared to the tedious processing in presence of high magnetic field and further careful sintering to preserve the texture obtained during green body processing. In the present case, the synthesized powder has a platelet morphology (Fig.4.18.b) and hence during pressure assisted sintering the platelets gets aligned to their lowest energy state which corresponds to the basal texture observed by pole figure and ODF.

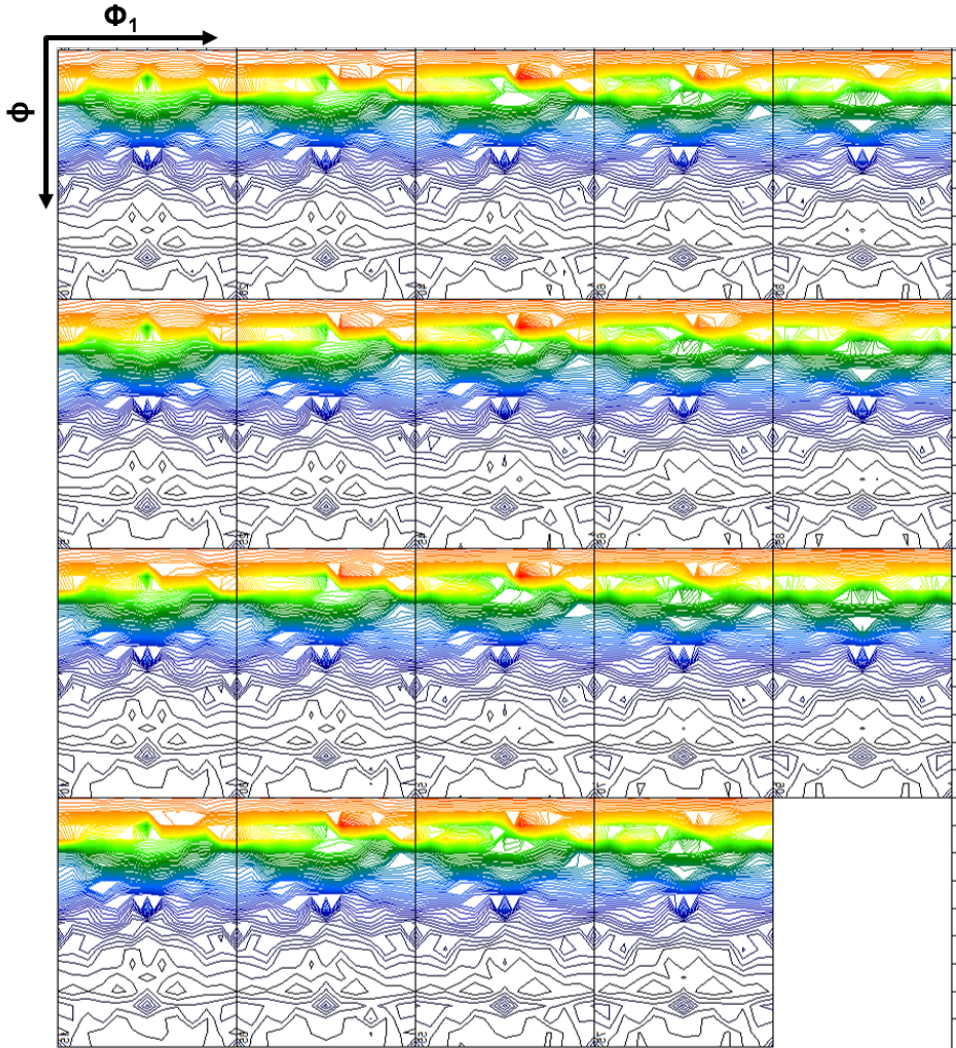


Figure 5.6: Orientation distribution function of spark plasma sintered Ti_3SiC_2 with ϕ_2 section from 0° to 90° .

GRAIN SIZE MEASUREMENT AND PHASE MAP

The microstructure of a spark plasma sintered material tends to be anisotropic due to the uniaxial pressure and not isotropic pressure. In case of materials with non-cubic crystallography, the anisotropy is exaggerated in the microstructure. In an anisotropic microstructure, the grain size measurement is calculated by considering the geometric mean of the grain sizes of the surface perpendicular and parallel to the application of load during sintering at high temperature. The elongated grains with high aspect ratio make it difficult to have an overall grain size distribution.

The equivalent grain size is calculated by the following relation:[7]

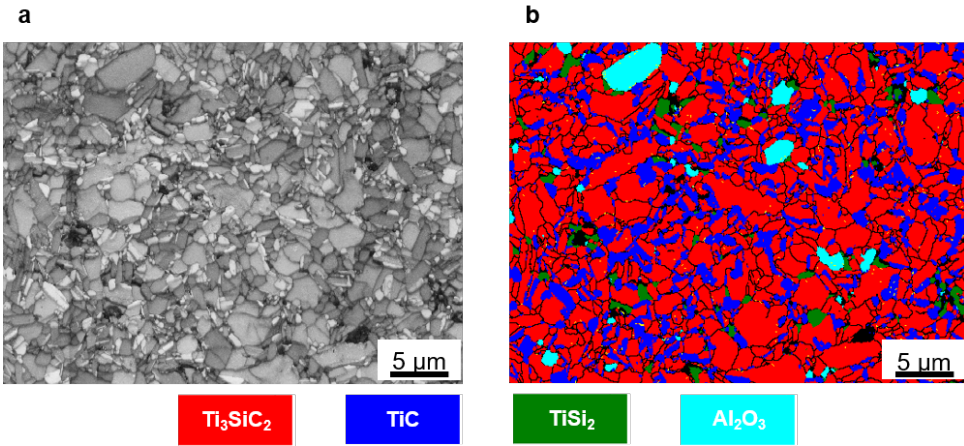


Figure 5.7: **a** Microstructure and **b** phase map of the perpendicular surface (top) of sintered Ti_3SiC_2 obtained from the band contrast of kikuchi patterns.

$$\frac{4}{3}\pi\left(\frac{d_{\perp}}{2}\right)^2\left(\frac{d_{\parallel}}{2}\right) = \frac{4}{3}\pi\left(\frac{d_{eff}}{2}\right)^3 \Rightarrow d_{eff} = \sqrt[3]{(d_{\perp}^2 d_{\parallel})} \quad (5.4)$$

Where d_{\perp} and d_{\parallel} are the average grain size of perpendicular and parallel face respectively. Although the grain morphology was different comparing the parallel and perpendicular face, the average grain size calculated by the projected area diameter was similar for both faces and the effective grain size was always calculated to be $1.2 \pm 0.6 \mu\text{m}$. Fig.5.7 shows the grain morphology and phase map of sintered Ti_3SiC_2 from the top surface of the specimen. The grain shape is equiaxed with large grains of approximately $5 \mu\text{m}$ in diameter accompanied with small grains below $1 \mu\text{m}$. The formation of TiC (4.93 g/cm^3) and TiSi_2 (4.02 g/cm^3) by decomposition does not affect the calculated density because of the counter-compensation of new phases resulting in an aggregate same density as of Ti_3SiC_2 . The presence of TiC on the grain boundaries supports the assumption of Si depletion from the grain boundaries in vacuum at high temperature. It is noteworthy that TiC is only seen on grain boundaries and not the interior of the Ti_3SiC_2 grain. TiSi_2 may have formed due to the reaction between de-intercalated Si and Ti_3SiC_2 resulting in the subsequent formation of more TiC. The presence of alumina grains can be explained by the fact that Al was used for enhancing the purity of Ti_3SiC_2 .

The role of Al was to form an impervious layer of alumina in the interface of salt and reaction mixture to stop the out-diffusion of Si. There might be residual Al after the synthesis process which can be oxidized due to the boiling of synthesized product in water to clean the salt content. The grain shape of the side surface of the sintered Ti_3SiC_2 has a lenticular shape. With the grain morphology of the top and side surface, the three-dimensional shape of the grain can be assumed to be platelet like which is the morphology of the initial Ti_3SiC_2 particles after synthesis. The platelets are aligned perpendicular to the direction of application of pressure.

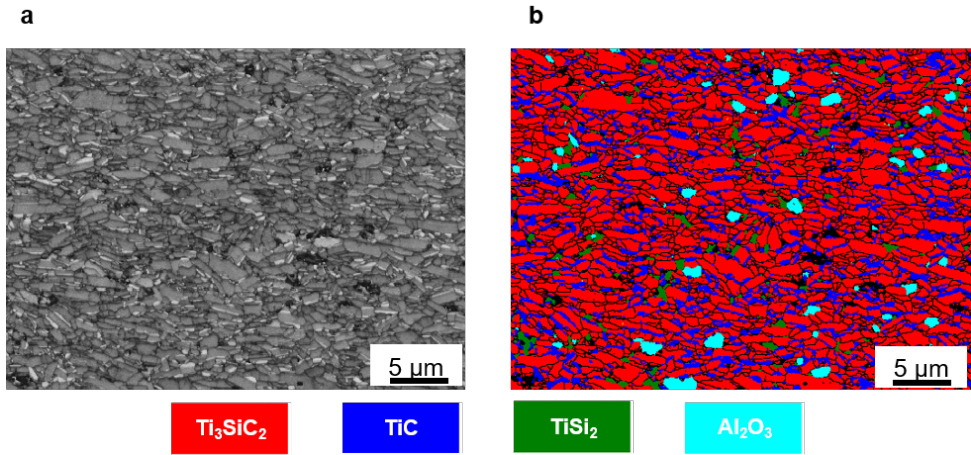


Figure 5.8: **a** Microstructure and **b** phase map of the parallel surface (side) of sintered Ti_3SiC_2 obtained from the band contrast of kikuchi patterns.

5

ELECTRON BACK SCATTERED DIFFRACTION

Although pole figures and ODF provide the information for the texture present in the material, they do not show visually the orientation of single grains. Moreover, x-ray investigations yield macrotexture and EBSD results in the realization of microtexture. Fig.5.9 shows the EBSD scan of top and side surface of sintered Ti_3SiC_2 .

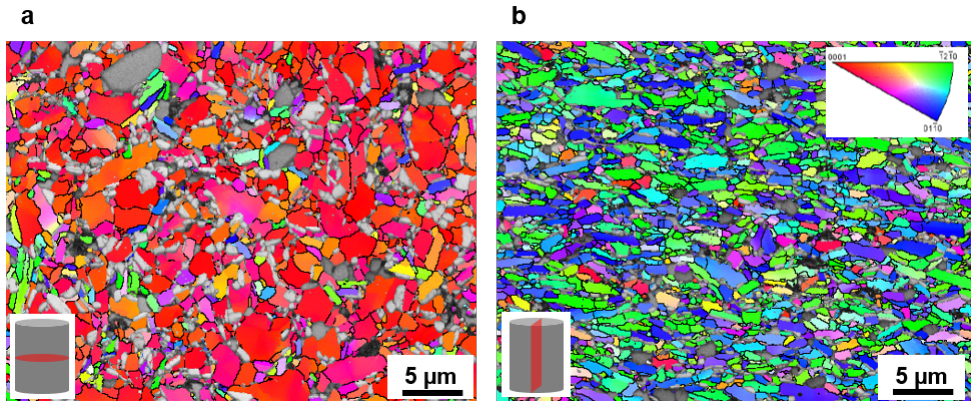


Figure 5.9: Orientation map of sintered Ti_3SiC_2 , **a** top surface and **b** side surface of the specimen perpendicular and parallel to the direction of applied uniaxial load. The top right inset in **b** shows the inverse pole figure key for the orientation map in **a** and **b**.

The EBSD orientation map suggests that the basal plane is oriented in the normal direction plane. If the Ti_3SiC_2 grains are considered to be individual hexagon crystals, the 0001 basal plane which should be hexagonal in shape in ideal condition faces upright and is represented by a higher density of red color in Fig.5.9.a. As prismatic texture is

complimentary to basal texture in a hexagonal system, it is expected that the orientation map of the side surface in Fig.5.9.b has a prismatic texture with $(11\bar{0}0)$ family of planes. This is in contradiction to the results obtained by Tang et al. who reported that the basal planes of Ti_3SiC_2 do not prefer to be oriented parallel to the pressing surface during hot press.[8] The reason might be due to the reaction sintering in the case of hot pressing. In the present case, already synthesized Ti_3SiC_2 powder with platelet morphology was used and hence the strong basal texture on the pressing surface.

5.2. GRAIN GROWTH OF TEXTURED Ti_3SiC_2 AND ITS CHARACTERIZATION

Ti_3SiC_2 is known to have different mechanical properties for its fine grained and coarse grained counterparts and as it was observed that there is a texture evolution along with coarsening of the grains. Ti_3SiC_2 was annealed at 1500 °C for 1 h in argon to induce grain growth. The properties of Ti_3SiC_2 depend on the grain size, moreover the microstructure evolution of textured Ti_3SiC_2 has not been reported till date.[9] The large grains of Ti_3SiC_2 have higher propensity to delaminate and kink as compared to fine grain counterpart. This difference makes the same material with a higher grain size behave differently as far as mechanical response is concerned.

X-RAY DIFFRACTION

The high temperature treatment resulted in the recombination of TiC and TiSi_2 to form Ti_3SiC_2 . The TiC peak disappeared from the XRD pattern after annealing at 1500 °C. Moreover, the peaks of the 101 family planes also disappeared suggesting an increase in the basal texture. The XRD pattern of the interior of the sample is like that of SPS sintered Ti_3SiC_2 . The increase in purity of Ti_3SiC_2 may be related to the long processing time during annealing as compared to the SPS operation in vacuum. The results obtained are in agreement to the phase composition reported by Murugaiah et al.[10] The condition for grain growth was intermediate to that of fine grains and coarse grains, hence in the present case the microstructure can be expected to be duplex. Since the $(hk0)$ reflections disappeared after annealing at 1500 °C, the lotgering factor (f_L) of the annealed sample was re-calculated. The f_L was calculated to be 0.96 which is very high for a polycrystalline sample. Since the value of f_L is approaching the value of 1 which is the representative of a single crystal. A conclusion based on the f_L speculation can be drawn that the solid-state single crystal conversion (SCC) of Ti_3SiC_2 phase is not anecdotal. It may be achieved by prolonged annealing of textured Ti_3SiC_2 at high temperature (>1500 °C) to enable the grain boundaries to move to the surface of the specimen, rendering the MAX phase into a single crystal entity. Dillon et al. demonstrate the SCC of alumina by local co-doping of alumina to induce controlled abnormal grain growth.[11]

POLE FIGURE

The pole figure shown in Fig.5.10.a has intense peaks at specific points which suggests that the presence of very few orientations which has a single peak in the center of the pole figure. The grain growth process has intensified the basal texture. The grains with strong basal texture consumed other grains with weak basal texture. This can also be

correlated to the fact that the grains of MAX phases or hexagonal materials in general prefer to grow in a direction parallel to the basal plane. The 110 pole figure shown in Fig.5.11.b also intensified at certain points which represent specific atomic planes. It is noteworthy that the intensity in Fig.5.11.a is one order of magnitude higher than that of the finer grain counterpart (Fig.5.3.a).

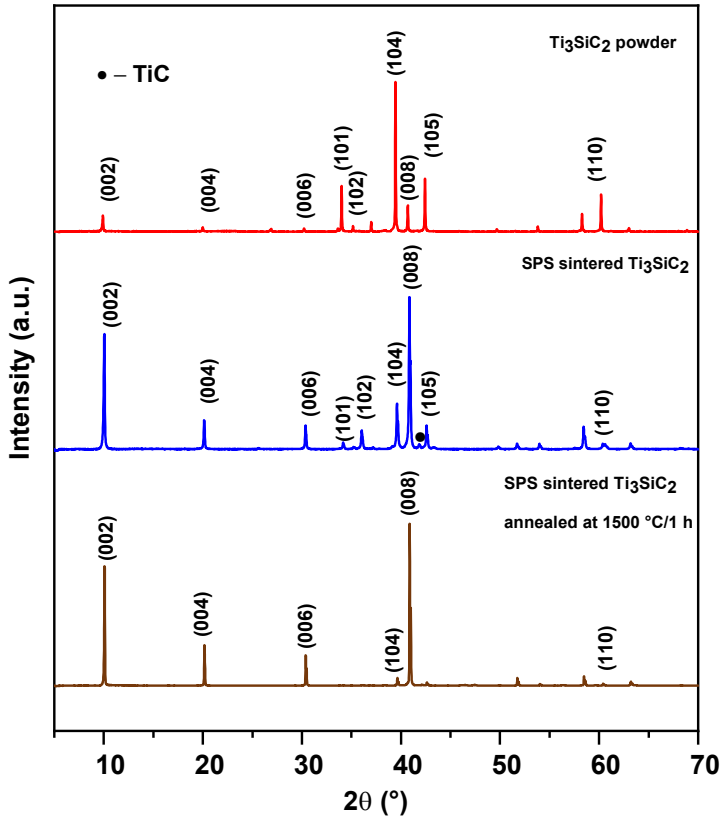


Figure 5.10: XRD pattern of synthesized Ti_3SiC_2 powder, SPS sintered and high temperature ($1500^\circ C/1h$) annealed Ti_3SiC_2 .

ORIENTATION DISTRIBUTION FUNCTION

The pole figures provide evidence for the increase in basal texture during grain growth, but they do not provide the complete information of the texture evolution in the bulk of the sample and hence an ODF was plotted for the coarse grained textured Ti_3SiC_2 and is shown in Fig.5.12.

The texture components identified from the ODF in Fig.5.12 are $0001 \langle 10\bar{1}0 \rangle$ and $0001 \langle 11\bar{2}0 \rangle$ and can be referred to table 5.3. The basal texture is getting weaker and there is evolution of other texture components. The weakening of basal texture can be attributed to the grain growth process which consumed the grains with basal texture

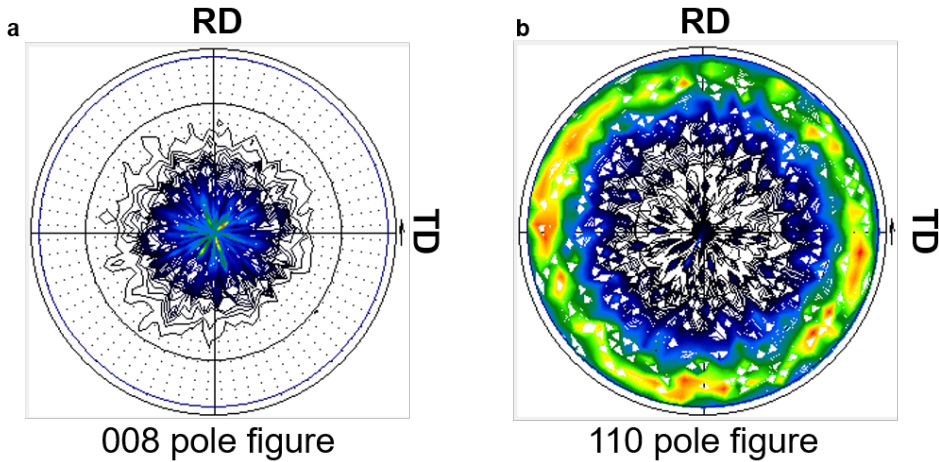


Figure 5.11: Incomplete pole figures of **a** 008 and **b** 110 orientation in normal direction of high temperature annealed Ti_3SiC_2 , (VIBGYOR intensity scale **a** 0-31208 **b** 0-1205).

orientation. The hypothesis of differential grain growth on the surface and in the interior bulk of the material is still subject to speculation and further studies to come to derive a tangible conclusion of the texture evolution of Ti_3SiC_2 during the grain growth process.

MICROSTRUCTURE AND PHASE MAP

The microstructure of annealed Ti_3SiC_2 is highly anisotropic with grains with very high aspect ratio. The grains are aligned in a direction perpendicular to the application of pressure during sintering. Since the initial alignment of the basal plane was perpendicular to the normal direction, the grain growth was preferred along the basal plane resulting in a grain with very high aspect ratio. Fig.5.13.a shows the microstructure of annealed Ti_3SiC_2 .

Fig.5.13.b shows the phase map and since the image is at a low magnification, it a better representation of the phase composition and the wt.% of Ti_3SiC_2 calculated was 93%. Moreover, the content of TiC and Al_2O_3 were calculated to be 3.8 and 2 wt.% respectively. It is evident that annealing resulted in a duplex microstructure with very large grains embedded in a matrix of very fine grains. The grain size of the large grains are above $500\ \mu\text{m}$ and the grain size of the fine grains are nearly $1\ \mu\text{m}$. Hence, the calculation of the average grain size wouldn't be a realistic representation.

ELECTRON BACK SCATTERED DIFFRACTION

Fig.5.14 shows the EBSD of side surface of Ti_3SiC_2 annealed at $1500\ ^\circ\text{C}$ for 1 h. The duplex microstructure is due to the selection of temperature and time for annealing ($1500\ ^\circ\text{C}$, 1 h).

Unlike the top surface which has pure basal texture, the side surface has a mixed pyramidal and prismatic texture and grain growth can lead to the exaggeration of one of

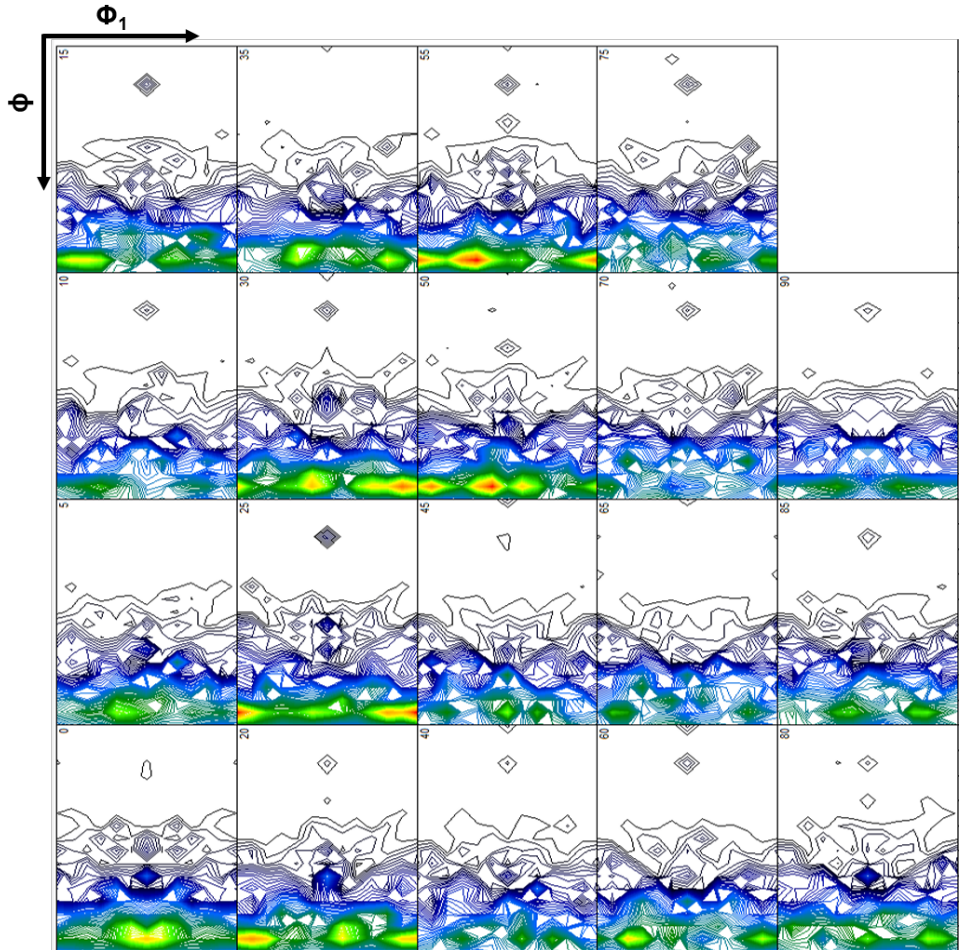


Figure 5.12: Orientation distribution function of high temperature annealed (1500 °C) Ti_3SiC_2 with ϕ_2 section from 0° to 90° .

either. Fig.5.14.b shows the propagating front of the grain boundary, wherein the small grains with similar orientations are consumed by the large grains, whereas other small grains with basal orientation (grains in red color) are entrapped within the large grains. Fig.5.14.c shows the grain boundary interface of two large grains which are equilibrium with each other and the grain boundary mobility may have been ceased due to the reduction in the curvature of the grain boundaries and absence of sufficient thermal activation leading to further atomic jumps across the grain boundary.[12] The top surface of annealed Ti_3SiC_2 showed in Fig.5.15 has faceted grains rather than equiaxed grains as in the as-sintered Ti_3SiC_2 . The annealing process may have resulted in a more equilibrium grain boundary configuration. The EBSD measurement is done at a very high magnification and hence the imaging is perhaps focused on the fine grain matrix of the duplex

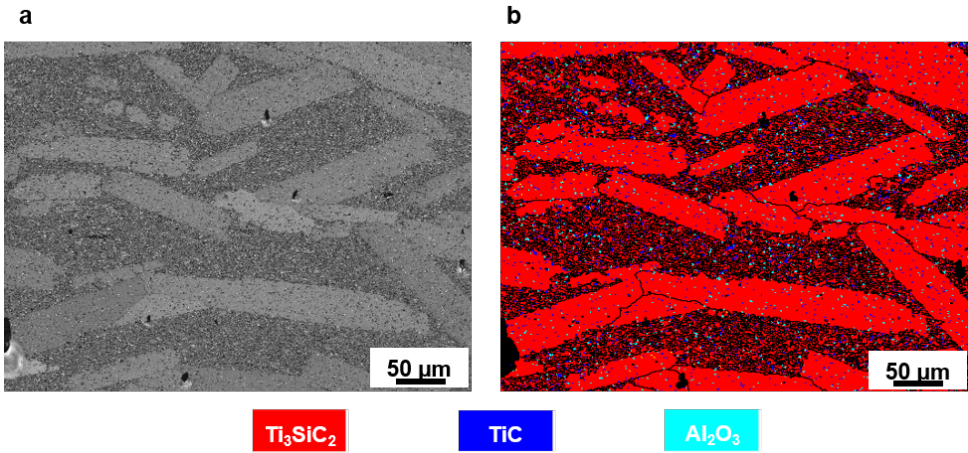


Figure 5.13: **a** Microstructure and **b** phase map of the parallel surface (side) of high temperature (1500 °C) annealed Ti_3SiC_2 obtained from the band contrast of kikuchi patterns.

5

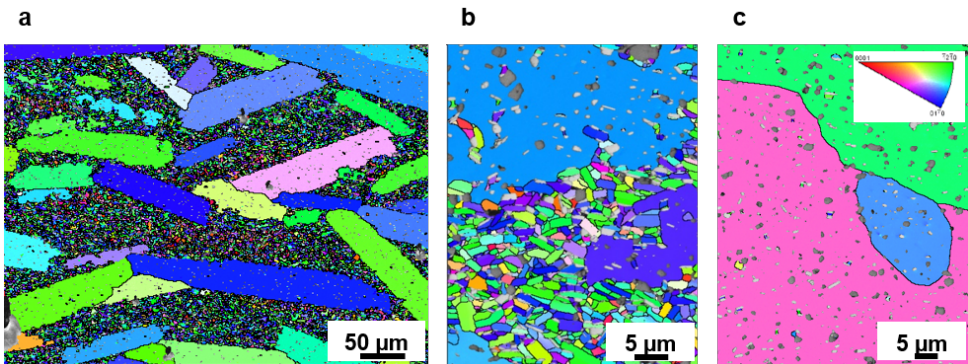


Figure 5.14: Orientation map of high temperature annealed Ti_3SiC_2 , **a** side surface, **b** the interface of coarse-fine grains and **c** the interface of coarse-coarse grains. The top right inset in **c** shows the inverse pole figure key for the orientation map in **a**, **b** and **c**.

microstructure. An EBSD measurement with a low magnification may reveal the basal plane of large grains shown in Fig.5.14.a.

5.3. CHARACTERIZATION OF SPARK PLASMA SINTERED SHORT $\text{SiC}_f / \text{Ti}_3\text{SiC}_2$ COMPOSITES

SiC fiber containing composites are novel material system which can provide a new aspect for the research in composite materials. Chopped SiC_f offers the ease of fabrication and also higher mechanical stability for the composite. $\text{SiC}_f / \text{Ti}_3\text{SiC}_2$ composites (TSC- SiC_f) were fabricated by mixing chopped Hi-Nicalon SiC fibers of 1 mm length and 10 μm

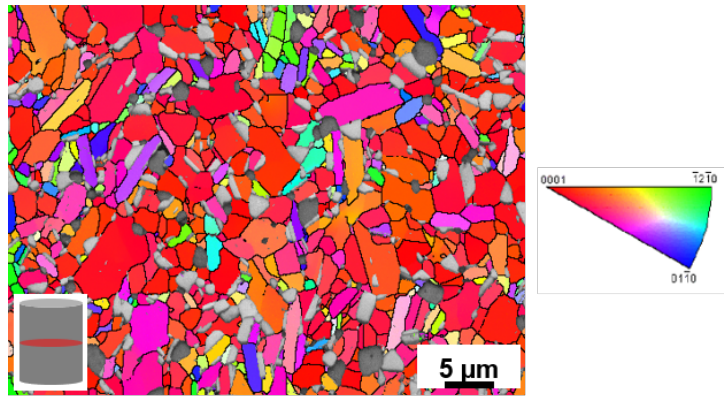


Figure 5.15: Orientation map of high temperature annealed Ti_3SiC_2 top surface.

5

diameter. Fig.5.16 shows the XRD and SEM of chopped SiC fiber. The XRD shows β -SiC phase with wide peaks suggesting nano-crystalline grains..

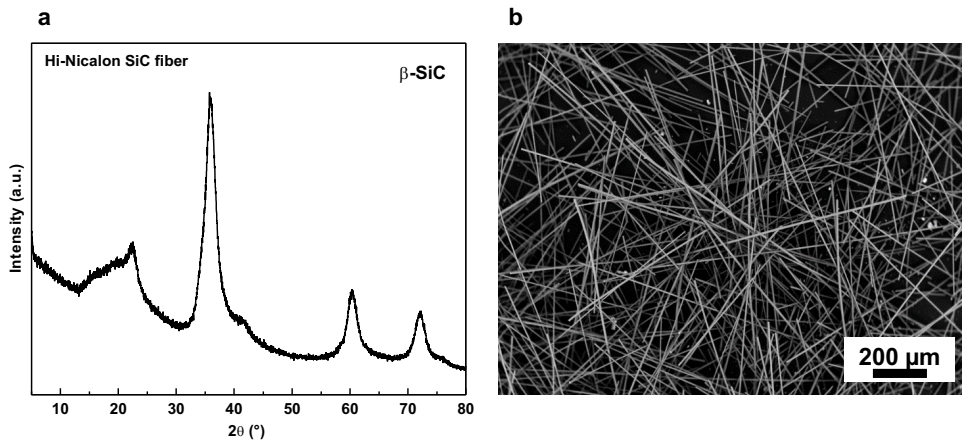


Figure 5.16: Chopped Hi-Nicalon SiC fibers, **a** XRD and **b** SEM.

X-RAY DIFFRACTION

The composites were densified in a SPS at 1250 °C for 35 min. To analyze the phase purity and a potential reaction XRD and SEM were performed. Fig.5.17 shows the XRD pattern of TSC-10SiC_f composite. The XRD shows similar basal texture on the top surface as that of monolithic material. The degree of basal plane alignment may have been hindered by the presence of chopped SiC fibers. The content of SiC_f was not substantial to be detected by X-ray diffraction. Moreover, the Hi-Nicalon SiC fibers are composed of nano crystals of β -SiC which decreases the signal to noise ratio. The alignment of SiC_f cannot be concluded from XRD data and needs direct imaging to be commented on. The

successful fabrication of a composite depends on the interaction of the matrix and reinforcement and in the present case the XRD suggests the absence of any reaction between Ti_3SiC_2 and SiC_f due to absence of any third phase apart from TiC which forms due to decomposition of Ti_3SiC_2 . The absence of any reaction between SiC_f and Ti_3SiC_2 is further supported by Spencer et al.[13] The XRD of TSC-20 SiC_f was like TSC-10 SiC_f and hence not shown here. The mass attenuation coefficient of SiC_f are higher and hence the peaks of Ti_3SiC_2 are more intense and the SiC_f are not identifiable by XRD.

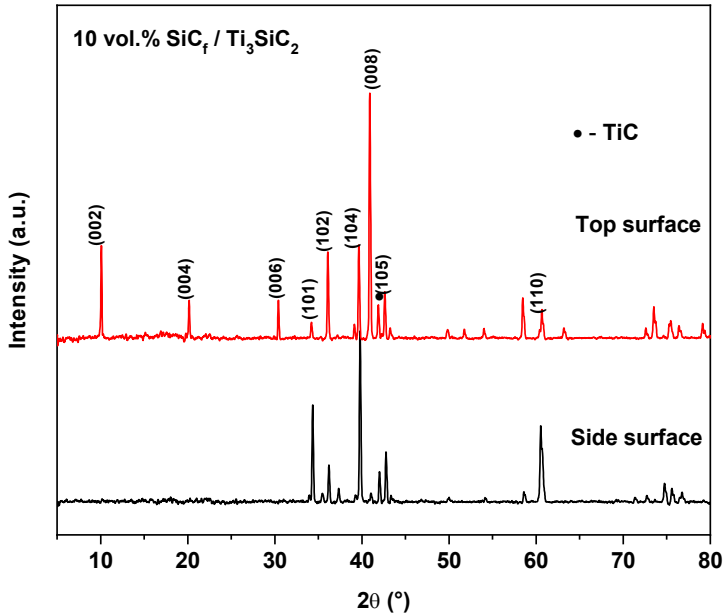


Figure 5.17: XRD of TSC-10 SiC_f ceramic composites with top surface and side surface.

SCANNING ELECTRON MICROSCOPY

Fig.5.18 shows the perpendicular and parallel surface of TSC-10 SiC_f sintered by SPS at 1250 °C for 30 min. Apart from the orientation of basal plane of Ti_3SiC_2 in the direction perpendicular to the pressing direction. The SiC fibers are also aligned and it can be seen in Fig.5.18.a as being aligned in the x-y plane if z-axis is considered as the normal direction or the direction along which the uniaxial pressure is applied. The SiC fibers appear dark because of material contrast. The fibers are randomly oriented in the x-y plane with the axis of the fiber aligned long the plane. Fig.5.18.b shows that cross-section of the fibers confirming the orientation of chopped SiC_f . The density of the SiC_f reinforced Ti_3SiC_2 CMCs were above 99% with no pores visible in the SEM of TSC-10 SiC_f . The addition of 20 vol.% of SiC_f resulted in an inhomogeneous distribution of fibers and agglomeration to form unresolvable knots which cannot be infiltrated by Ti_3SiC_2 powder during sintering. Hence, a higher content of SiC_f resulted in porous compact which cannot be further used for mechanical characterization. The content of the reinforcement can be increased by decreasing the size of the fibers which will offer a better homogene-

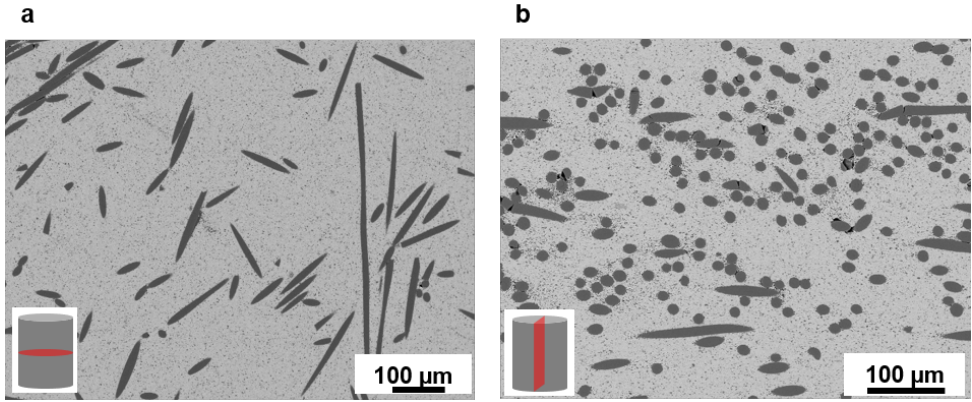


Figure 5.18: Back-scattered electron image of 10 vol.% SiC_f reinforced Ti_3SiC_2 , **a** perpendicular surface and **b** parallel surface.

5

ity. Fig.5.19 shows the fiber crinkling in the sintered TSC-20 SiC_f . The dispersion of SiC_f in TSC-20 SiC_f is erratic and the areas with high density of fibers have incomplete densification with large pores as shown in Fig.5.19.b. The problem of incomplete densification and poor dispersion maybe solved by using a surfactant-micelle system to stabilize the fibers in a suspension.

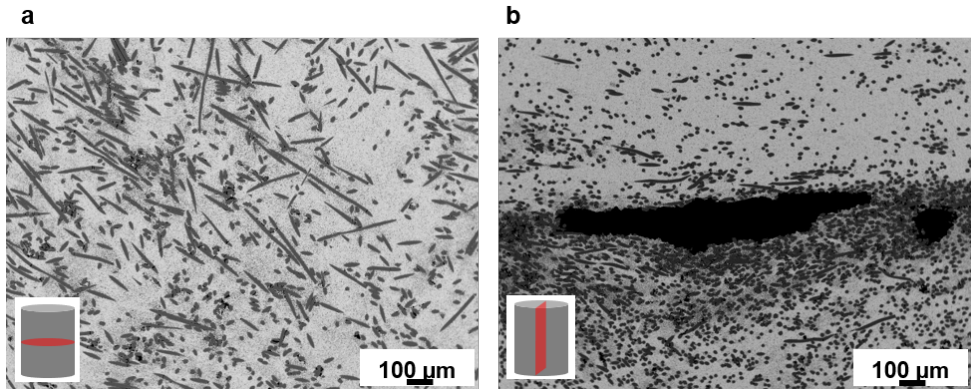


Figure 5.19: Back-scattered electron image of 10 vol.% SiC_f reinforced Ti_3SiC_2 , **a** perpendicular surface and **b** parallel surface.

ELECTRON BACK SCATTERED DIFFRACTION

The presence of SiC short fibers did not influence the microstructure evolution of sintered Ti_3SiC_2 in context to the grain size. However, the alignment of Ti_3SiC_2 platelets were greatly hampered by the presence of SiC fibers. The basal texture exists but is not as intense as that of monolithic Ti_3SiC_2 . The combination of X-ray data and EBSD con-

firmly that the presence of SiC_f has impeded the texture evolution of Ti_3SiC_2 . The SiC_f could not be indexed by EBSD because of nanocrystalline nature. The black patch on the top left hand side of Fig.5.20 shows the cross-section of a SiC_f .

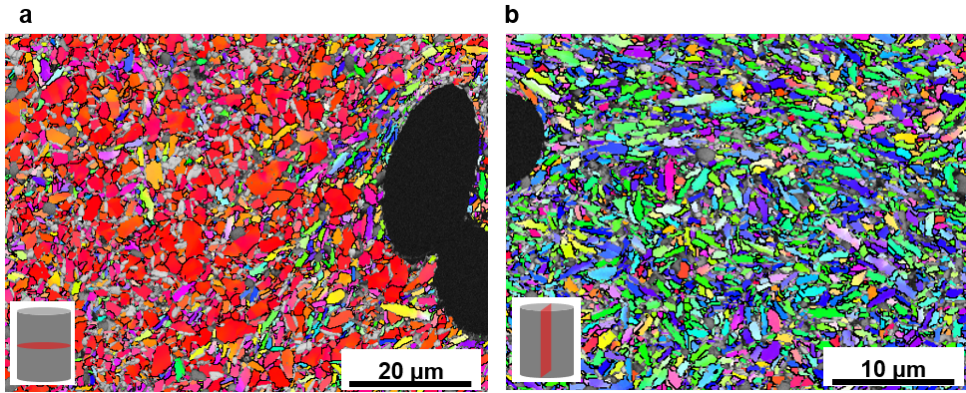


Figure 5.20: Orientation map of 10 vol.% SiC_f containing Ti_3SiC_2 **a** top surface and **b** side surface.

5.4. CHARACTERIZATION OF SPARK PLASMA SINTERED $\text{SiC}_w / \text{Ti}_3\text{SiC}_2$ COMPOSITES

In the present work, instead of using a shorter (<1mm) SiC fiber, SiC whisker were used which are single crystals of SiC with very high aspect ratio and will serve the purpose of reinforcement similar to fibers. However, the effect of reinforcement of SiC whiskers will be different than that of SiC_f . The silicon carbide whiskers (length: 10 μm , diameter of 1 μm) Haydale technologies, USA) used for the fabrication of the composites are shown in Fig.5.21. The as-received whiskers (Fig.5.21.a) were agglomerated and hence dispersed in ethanol and ultra-sonicated (Fig.5.17.b) for better dispersion.

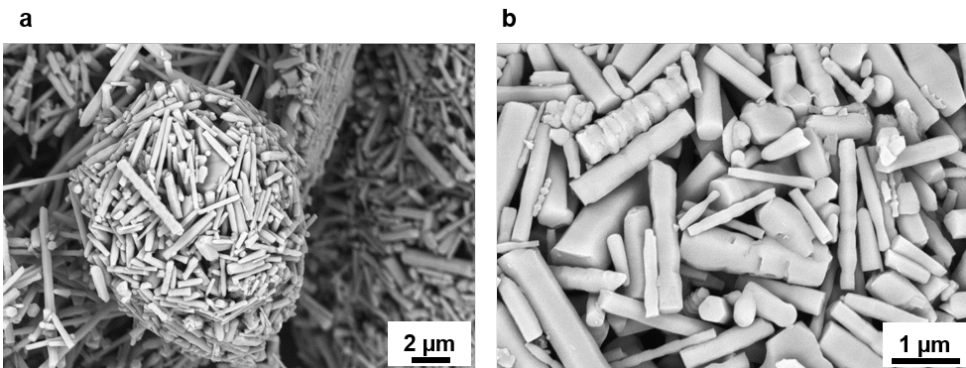


Figure 5.21: SEM of **a** as-received SiC whisker and **b** ultra-sonicated SiC whisker.

The density of the CMCs was measured to be above 99% of the theoretical value as calculated by considering the initial volume fraction of Ti_3SiC_2 and SiC_w . The formation of TiC (4.93 g/cm^3) and TiSi_2 (4.02 g/cm^3) by decomposition does not affect the calculated density because of the counter-compensation of new phases resulting in an aggregate with the same density of Ti_3SiC_2 . The size of whiskers is much smaller than that of SiC fibers and hence the reinforcement is in a much finer scale. Since the whiskers are single crystal entities they offer a different reinforcement mechanism than that of polycrystalline SiC fibers. The matrix-whisker interface does not provoke any crack propagation into the whisker along the grain boundaries as it does in case of fibers. The use of SiC whiskers gives us the possibility of full crack deflection along the matrix-whisker interface. However, the interface strength dictates the fate of the crack tip. This can further be engineered by surface treatments of the whisker. In the present case, whiskers were used as reinforcements without any further surface treatment. As whiskers are single crystals, they offer an atomically smooth surface which makes the need of an inter-phase superfluous.

X-RAY DIFFRACTION

Fig.5.22 shows XRD of Ti_3SiC_2 powder, SPS-sintered Ti_3SiC_2 and 20 vol.% SiC_w reinforced Ti_3SiC_2 . TSC-10 SiC_w is not shown because it is same as that of TSC-20 SiC_w . The XRD peaks correspond to Ti_3SiC_2 , SiC_w and other phases like TiC, Al_2O_3 and TiSi_2 . There is no direct implication of any interfacial chemical reaction between SiC_w and Ti_3SiC_2 that could have compromised the structural integrity of the final CMC. Although the starting Ti_3SiC_2 powder presented only 3 wt.% of TiC and 1 wt.% of Al_2O_3 , the sintered Ti_3SiC_2 has a higher content of TiC (8.8 wt.%) and Al_2O_3 (4.6 wt.%). The higher content of TiC might have resulted from the thermal decomposition of Ti_3SiC_2 during sintering. The change in the intensity ratio of the peaks at 39.5 and 40.8 2θ positions are due to the evolution of a crystallographic texture during sintering of Ti_3SiC_2 .

SCANNING ELECTRON MICROSCOPY

Fig.5.23.a, b and c show the microstructure of SPSed TSC, TSC-10 SiC_w and TSC-20 SiC_w after polishing a face perpendicular to the direction of external pressure applied during sintering. The dispersion of SiC_w is homogeneous in TSC-10 SiC_w whereas an increase in SiC_w resulted in agglomeration in TSC-20 SiC_w . However, the Ti_3SiC_2 matrix phase was infiltrated into the SiC_w agglomerates. There were no pores observed in any of the composition and this was beneficial for the evaluation of creep in further investigation.

GRAIN SIZE MEASUREMENT AND PHASE MAP

Fig.5.24.a reveals the grain shape and SiC_w orientation in the direction perpendicular to the direction of pressure for sintering. The high vacuum and uniaxial pressure applied during sintering might be responsible for the evaporation of Si from the crystal structure of Ti_3SiC_2 forming TiC. Fig.5.24.b depicts the phase map of TSC-20 SiC_w corresponding to Fig.5.24.a. The presence of TiC on the grain boundaries supports the assumption of Si depletion from the grain boundaries in vacuum at high temperature. The orientation of SiC_w may be beneficial for the creep resistance because the deformation due to compressive stress is in lateral direction which is same as that of whisker alignment. The

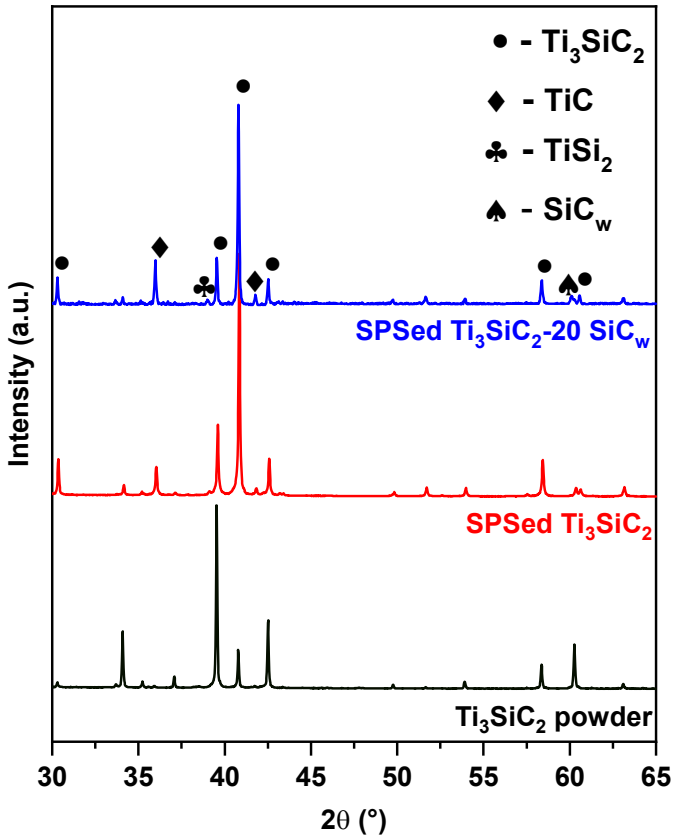


Figure 5.22: XRD of initial Ti_3SiC_2 powder and sintered $\text{SiC}_w / \text{Ti}_3\text{SiC}_2$ MAX phase composites.

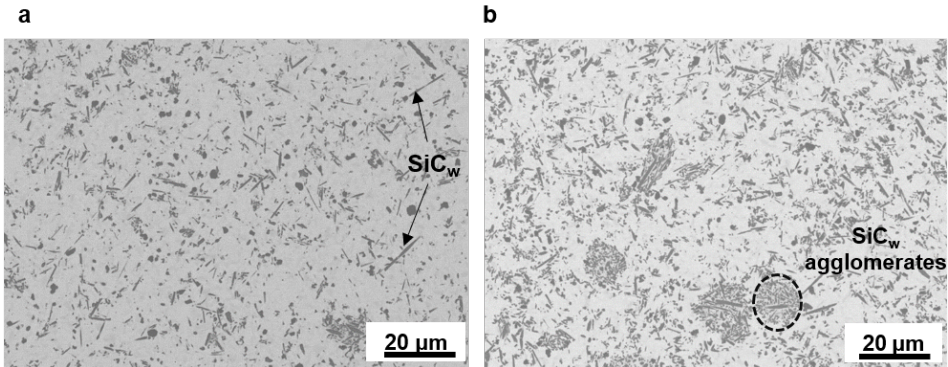


Figure 5.23: Back-scattered electron image of SPS sintered Ti_3SiC_2 a with 10 vol.% SiC_w and b 20 vol.% SiC_w .

microstructures of the CMCs on the perpendicular face are equiaxed with an average

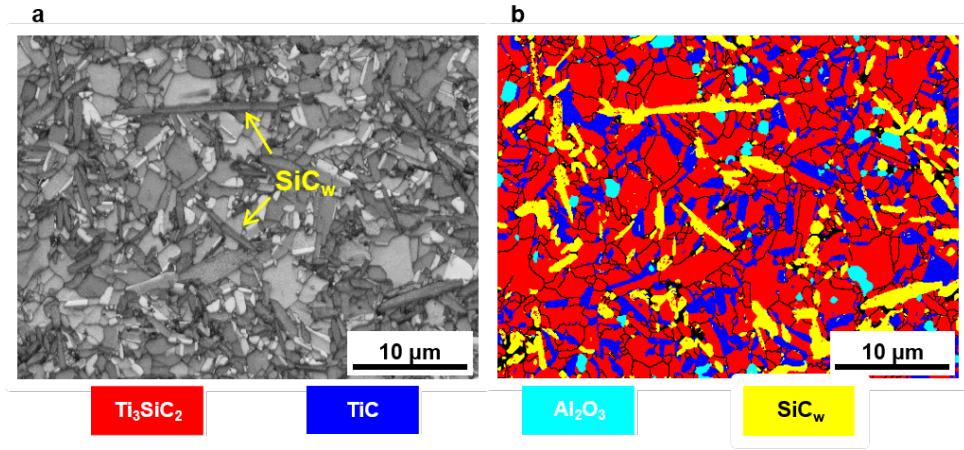


Figure 5.24: Microstructure of SPS sintered **a** Ti_3SiC_2 with 20 vol.% SiC_w and **b** phase map corresponding to **a**.

5

grain size of $1.2 \pm 0.6 \mu m$ of the Ti_3SiC_2 phase, irrespective of the SiC_w content.

ELECTRON BACK-SCATTERED DIFFRACTION

Fig.5.25.a shows the orientation map of TSC-10 SiC_w perpendicular to the pressing direction. Clearly, the sintered TSC-10 SiC_w has a texture due to the applied uniaxial external pressure and the rearrangements of the platelets under high temperature and pressure to attain a high density. The c-axis is parallel to the pressing direction. As expected, the SiC_w are also oriented perpendicular to the pressing direction and the perpendicular plane the orientation of the whiskers can be considered as random.[7] In Fig.5.25.b

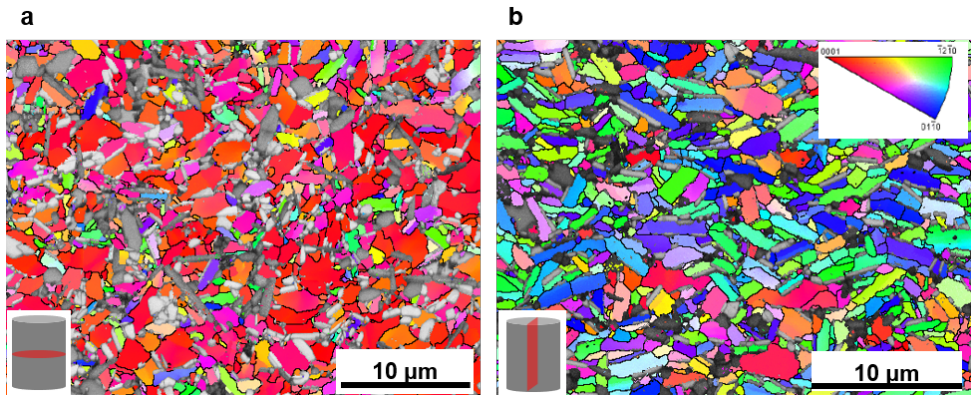


Figure 5.25: Orientation map of Ti_3SiC_2 with 10 vol.% of SiC_w , **a** perpendicular surface and **b** parallel surface.

only the tips of SiC_w are visible, hence not identifiable as entities with high aspect ratio (SiC_w). The Ti_3SiC_2 grains on the face perpendicular to pressing direction are equi-axed

whereas on the parallel to pressing direction the grains were elongated with an aspect ratio ≈ 10 .

The Ti_3SiC_2 platelets are not aligned perpendicular to the pressing direction as that of monolithic Ti_3SiC_2 (Fig.5.9.b). This maybe be attributed to the presence of SiC whisker between the particles of Ti_3SiC_2 which impedes the rearrangement of platelets during sintering process. This was not observed in the case of SiC_f reinforced Ti_3SiC_2 because of the higher scale of reinforcement.

REFERENCES

- [1] A. Dash, J. Malzbender, K. Dash, M. Rasinski, R. Vaßen, O. Guillon, and J. Gonzalez-Julian, *Compressive creep of SiC whisker/ Ti_3SiC_2 composites at high temperature in air*, Journal of the American Ceramic Society **103**, 5952 (2020).
- [2] A. Dash, J. Malzbender, R. Vaßen, O. Guillon, and J. Gonzalez-Julian, *Short SiC fiber/ Ti_3SiC_2 MAX phase composites: Fabrication and creep evaluation*, Journal of the American Ceramic Society **103**, 7072 (2020).
- [3] M. Mishra, Y. Sakka, C. Hu, T. S. Suzuki, T. Uchikoshi, and L. Besra, *Electrophoretic deposition of Ti_3SiC_2 and texture development in a strong magnetic field*, Journal of the American Ceramic Society **95**, 2857 (2012).
- [4] Y. Wang and J. Huang, *Texture analysis in hexagonal materials*, Materials Chemistry and Physics **81**, 11 (2003).
- [5] K. Sato, M. Mishra, H. Hirano, T. S. Suzuki, and Y. Sakka, *Fabrication of textured Ti_3SiC_2 ceramic by slip casting in a strong magnetic field and pressureless sintering*, Journal of the Ceramic Society of Japan **122**, 817 (2014).
- [6] C. Hu, Y. Sakka, S. Grasso, T. Suzuki, and H. Tanaka, *Tailoring Ti_3SiC_2 ceramic via a strong magnetic field alignment method followed by spark plasma sintering*, Journal of the American Ceramic Society **94**, 742 (2011).
- [7] A. De Arellano-Lopez, A. Dominguez-Rodriguez, and J. Routbort, *Microstructural constraints for creep in SiC-whisker-reinforced Al_2O_3* , Acta materialia **46**, 6361 (1998).
- [8] K. Tang, C.-a. Wang, Y. Huang, and J. Xia, *An x-ray diffraction study of the texture of Ti_3SiC_2 fabricated by hot pressing*, journal of the European ceramic Society **21**, 617 (2001).
- [9] T. Zhen, M. Barsoum, S. Kalidindi, M. Radovic, Z. Sun, and T. El-Raghy, *Compressive creep of fine and coarse-grained Ti_3SiC_2 in air in the 1100–1300 °C temperature range*, Acta materialia **53**, 4963 (2005).
- [10] A. Murugaiah, A. Souchet, T. El-Raghy, M. Radovic, M. Sundberg, and M. Barsoum, *Tape casting, pressureless sintering, and grain growth in Ti_3SiC_2 compacts*, Journal of the American Ceramic Society **87**, 550 (2004).

- [11] S. J. Dillon and M. P. Harmer, *Mechanism of “solid-state” single-crystal conversion in alumina*, *Journal of the American Ceramic Society* **90**, 993 (2007).
- [12] M. N. Rahaman, *Sintering of ceramics* (CRC press, 2007).
- [13] C. B. Spencer, J. M. Córdoba, N. H. Obando, M. Radovic, M. Odén, L. Hultman, and M. W. Barsoum, *The reactivity of Ti_2AlC and Ti_3SiC_2 with SiC fibers and powders up to temperatures of 1550 °C*, *Journal of the American Ceramic Society* **94**, 1737 (2011).

6

RESULTS & DISCUSSIONS III

Compressive creep resistance of short SiC fiber / Ti_3SiC_2 composites

HIGH temperature compressive creep measurements were done on a variety of monolithic and reinforced Ti_3SiC_2 ceramics. The details of the samples with the corresponding nomenclature is shown in Table 6.1. The creep was measured in the temperature range of 1100-1300 °C under a uniaxial compressive pressure of 20-120 MPa. Since

Table 6.1: Nomenclature of samples under high temperature compressive creep investigation

Microstructure	Basal plane orientation	Reinforcement	Sample ID
Fine	x-y plane	-	TSCFxy
Fine	x-z plane	-	TSCFxz
Duplex	x-y plane	-	TSCDxy
Duplex	x-z plane	-	TSCDxz
Fine	x-y plane	10 vol.% SiC _f	TSCF-10SiC _f
Duplex	x-y plane	10 vol.% SiC _f	TSCD-10SiC _f
Fine	x-y plane	10 vol.% SiC _w	TSC-10SiC _w
Fine	x-y plane	20 vol.% SiC _w	TSC-20SiC _w

the sintered samples were highly textured with a preferential basal plane orientation, the creep was also measured with the compression axis parallel and perpendicular to the basal plane orientation. Fig.6.1 shows the configuration of the Ti_3SiC_2 samples cut in a different geometry from the same sintered block.

Parts of this chapter have been published in Journal of American Ceramic Society **103**, 5952 (2020) and **103**, 7072 (2020) [1, 2].

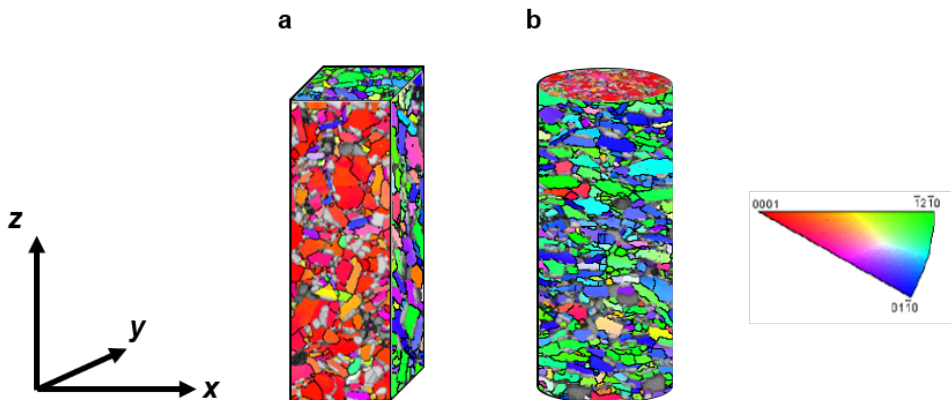


Figure 6.1: Machined creep samples of Ti_3SiC_2 with basal plane **a** parallel (TSCFxz) and **b** perpendicular (TSCFxy) to the compression direction of creep.

6.1. CREEP OF TEXTURED Ti_3SiC_2

6.1.1. STEADY STATE CREEP OF FINE GRAINED TEXTURED Ti_3SiC_2

Like other physical properties, creep resistance is also a function of the crystallographic anisotropy and hence the investigation of creep resistance of textured Ti_3SiC_2 was done in different configurations. Fig.6.2 shows the strain vs. time plot at a constant temperature (1100, 1200 °C) and load (20 MPa).

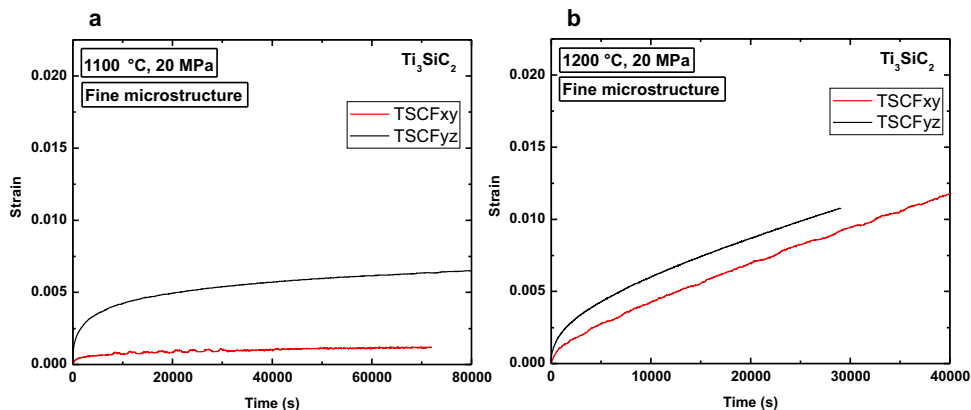


Figure 6.2: Compressive creep curves of textured Ti_3SiC_2 at **a** 1100 °C, 20 MPa and **b** 1200 °C, 20 MPa.

The creep was measured only in the steady state regime, it is to be noted that the creep of TSCFyz at 1100 °C, 20 MPa has an influence of the primary creep. The tests were aborted before the tests could go into tertiary regime. Although the initial deformation of TSCFyz was higher the creep rate of both TSCFxy and TSCFxz at 1100 °C, 20 MPa were similar. The higher initial deformation of TSCFxz can be related to the forma-

tion of probable kink bands due to the basal plane being aligned parallel to the applied load direction. TSCF_{xz} is more prone to deformation because the stresses generated by loading can be relieved by shear of the layers relative to each other. Since MAX phases only constitute basal dislocations, individual grains of TSCF_{xz} can also undergo more extensive bending as compared to the TSCF_{xy} grains. At 1200 °C, the total deformation has increased and so has the creep rate which is evident from the slope of the curves in Fig.6.2.b. As Ti_3SiC_2 has a brittle to plastic transition (BPT) at around 1200 °C, the increase in deformation is obvious.[3] The deformation of MAX phases are simple as compared to metals because of absence of any slip plane other than the basal slip. Hence deformation by dislocations can only take place in grains with the alignment of basal plane parallel to applied stress. However, the deformation of MAX phases can be seen as complicated because the deformation is more than just the movement of dislocations as in other crystalline materials. Multiple phenomenon like shear banding, grain delamination, grain bending and kink band formation can act in a mutually exclusive manner or together.[4] However, the deformation and creep rates of TSCF_{xy} and TSCF_{xz} at 1300 °C, 20 MPa are different (meanwhile at lower temperatures were similar). Fig.6.3 shows the strain vs. time curve at 1300 °C and 20 MPa.

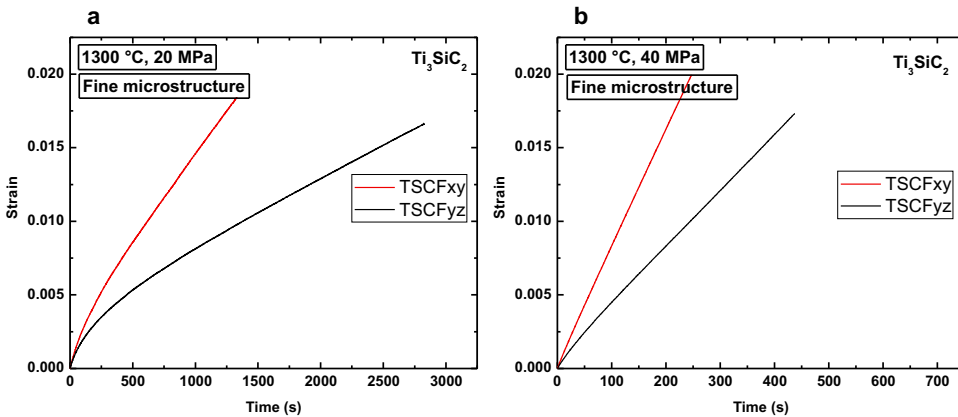


Figure 6.3: Compressive creep curves of textured Ti_3SiC_2 at 1300 °C, **a** 20 MPa and **b** 40 MPa.

The difference in creep rate of TSCF_{xy} and TSCF_{xz} is controlled by temperature. The reason about why TSCF_{xy} is more susceptible to deformation is not exactly clear. The same is true for creep at 1300 °C at a higher load of 40 (Fig.6.3.b) and 80 MPa (not shown here). TSCF_{xz} are loaded with their basal planes edge-on and hence more prone to kinking.[5] TSCF_{xy} are loaded with their basal plane face-on and hence more susceptible to shear banding.

6.1.2. STEADY STATE CREEP OF COARSE GRAINED TEXTURED Ti_3SiC_2

The Ti_3SiC_2 under investigation is more precisely with a duplex microstructure. However, the rate controlling factor for the creep deformation is the least creeping grains. Hence the response of the duplex microstructure towards the creep will be an average

of fine grains and coarse grains. As already known, coarse grains of MAX phases have a higher tendency to form kink bands and shear bands resulting in a higher initial deformation. However, coarse grained Ti_3SiC_2 is also known to have a lower creep resistance as compared to fine grained Ti_3SiC_2 . [6] The creep resistance of coarse grained textured Ti_3SiC_2 has not been reported till date. This section is about the creep resistance of high temperature (1500 °C) annealed Ti_3SiC_2 mentioned in Chapter 5. TSCD_{xy} and TSCD_{xz} were subjected to a constant load of 20-120 MPa from a temperature of 1000-1300 °C. The creep of TSCD_{xy} was not measured because of rapid deformation and it was not possible to attain a steady state creep rather directly into tertiary creep. Fig.6.4 shows the creep curves of TSCD_{xy} and TSCD_{xz} at 1100 °C under 20 MPa load.

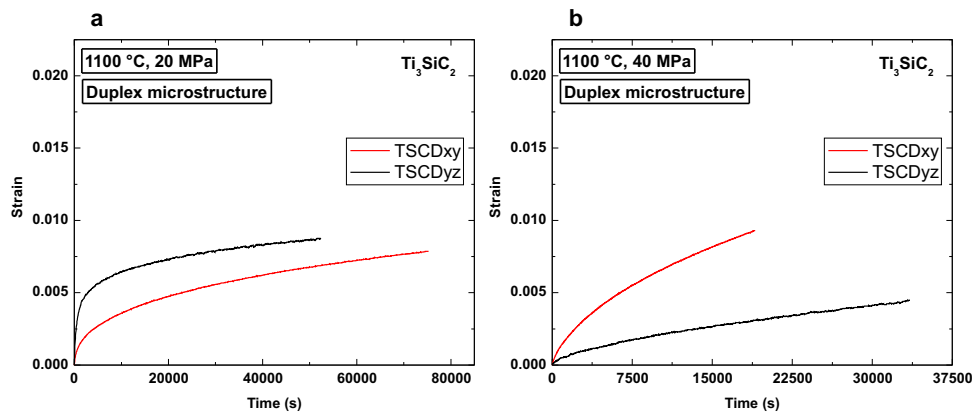


Figure 6.4: Compressive creep curves of high temperature annealed textured Ti_3SiC_2 at 1100 °C, a 20 MPa and b 40 MPa.

TSCD_{yz} has a higher deformation as compared to TSCD_{yz} at 1100 °C, 20 MPa whereas at 40 MPa TSCD_{xy} has a higher deformation. The combination of 1100 °C and 40 MPa may have been the threshold condition for the critical shear resolved stress in case of TSCD_{xy} for delamination of grains or possibility the formation of shear bands. At higher temperatures, TSCD_{xy} undergoes a higher deformation along with a higher creep rate as well. Fig.6.5 shows a comparison of the creep of fine and coarse grained textured Ti_3SiC_2 in every configuration. TSCD_{xz} has the highest deformation of all the other configurations of Ti_3SiC_2 . As 1100 °C is lower than the BPT and 20 MPa is a low load to initiate mechanisms like shear banding and delamination. Hence, the configuration which was easily deformable was the one with large grains of Ti_3SiC_2 with basal plane upright, so that the loading was edge-on. This is the probable reason for the highest deformation of TSCD_{xz}. With the exception of 1100 °C and 20 MPa (Fig.6.3.a), TSCD_{xy} has the highest deformation at higher temperature and pressure combination. Since TSCD_{xy} has elongated grains in the x-y plane. The creep of TSCD_{xy} might have resulted in grain fracture thereby leading to grain refinement. The cleavage of grains during creep needs a higher driving force as compared to simple dislocation creep. Moreover, it is observed that TSCD_{xz} bends after creep at 1300 °C, 80 MPa forming an arch between the top and bottom fixtures of the instron testing machine, whereas TSCD_{xy} only bulges radially. It

can be inferred from this observation that there is extensive grain kinking and bending in the case of TSCDxz. TSCDxy undergoes plastic deformation during the creep by the probable shearing of the basal planes resulting in material movement in a radial manner.

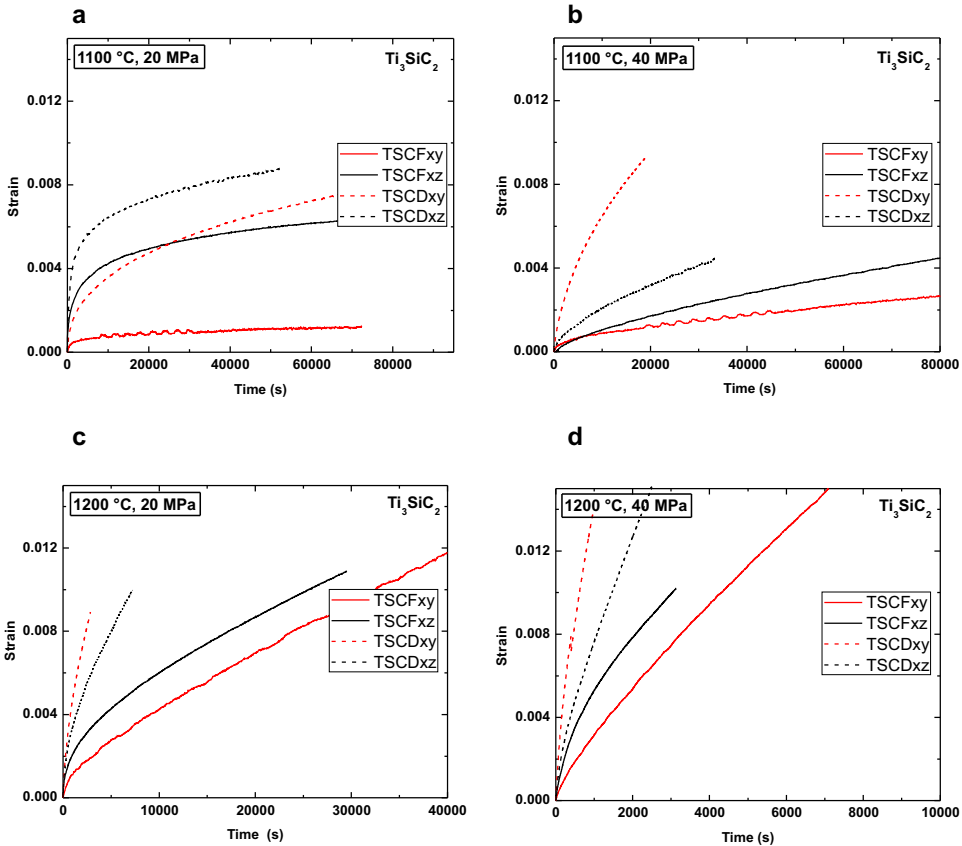


Figure 6.5: Compressive creep curves of TSCFxy, TSCFxz, TSCDxy, TSCDxz at 1100 °C, **a** 20 MPa, **b** 40 MPa and 1200 °C, **c** 20 MPa, **d** 40 MPa.

The trend of gradation of deformation resistance is similar 1200 °C with TSCFxy as the least deformable and TSCDxy as the most deformable. It is to be noted that the creep of Ti_3SiC_2 or any other MAX phase involves multiple phenomenon and it is difficult to decipher the main contributing factor for creep. Further analysis of activation energy, stress exponent supported with microstructural evidence are presented in further sections for a proposed creep mechanism.

6.1.3. CREEP ACTIVATION ENERGY AND STRESS EXPONENT

The activation energy and the stress exponent imply the rate controlling factor and the main creep mechanism respectively. However, the exact the mechanisms without direct evidence from high resolution microscopy are only speculative. The steady state creep

rate was obtained by measuring the slope of the fitted straight line in the steady state regime of the creep curves with time as the x-axis and creep strain as the y-axis. The activation energy and the stress exponent values were calculated by using the following relation[7]:

$$\dot{\epsilon} = \dot{\epsilon}_0 A \left(\frac{\sigma}{\sigma_0} \right)^n \exp \left(\frac{-Q}{RT} \right) \tag{6.1}$$

Where A, n, Q are dimensionless constant, stress exponent and activation energy respectively. $\dot{\epsilon}_0$ and σ_0 are 1 s^{-1} and 1 MPa, used for defining the dimensions of strain rate and stress. The slope of straight lines plotted by fitting the data of minimum creep rate with respect to inverse of absolute temperature and ln of the applied stress gives the activation energy and stress exponent respectively. Eq.6.1 is simplified into straight line equation ($y= mx + c$) by applying the natural logarithm on both sides of the equation where m accounts for the slope of the fitted line.

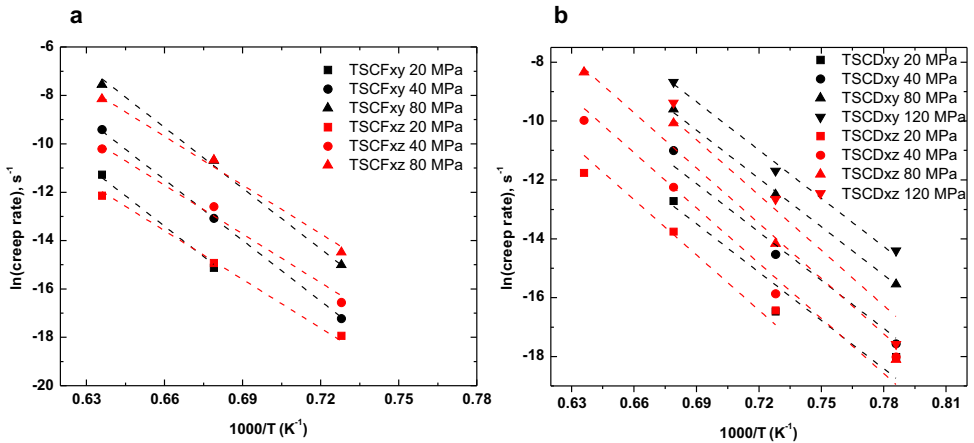


Figure 6.6: Ln-ln plot of min strain rate as a function of temperature for textured **a** fine and **b** coarse Ti_3SiC_2 .

Fig.6.6 and 6.7 shows the ln-ln plot of steady state creep rate vs. the inverse of temperature and the ln of the applied stress respectively. The activation energies and stress exponents of textured Ti_3SiC_2 for different configurations are mentioned in Table 6.2.

Table 6.2: Summary of creep activation energy and stress exponents of textured Ti_3SiC_2

Sample	Q (kJ/mol)	n	Reference
TSCFxy	696 ± 16	2.95 ± 0.13	This work
TSCFxz	558 ± 14	2.98 ± 0.14	This work
TSCDxy	454 ± 29	2.53 ± 0.11	This work
TSCDxz	520 ± 31	2.54 ± 0.12	This work
Ti_3SiC_2 fine	537 ± 31	1.9	[6]
Ti_3SiC_2 coarse	835 ± 40	2.1	[6]

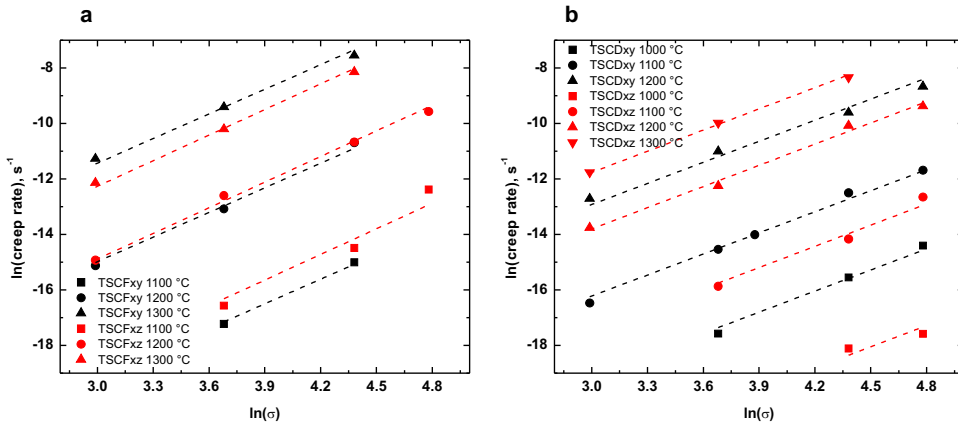


Figure 6.7: Ln-ln plot of min. strain rate as a function of applied compressive stress during the creep test of textured **a** fine grained and **b** coarse grained Ti_3SiC_2 .

TSCFxy has the highest activation energy for creep and TSCFzx has lower activation energy and is consistent as every stress values (Fig.6.6.a). TSCDxy has the lowest activation energy. It is worth nothing that TSCFzx and TSCDzx has similar activation energy which might suggest that the xz alignment of basal plane makes the creep response independent of grain size. The alumina and TiC present in the sintered Ti_3SiC_2 might also affect the creep response of the material but it is safe to compare the different grades of textured Ti_3SiC_2 because they all contain same vol.% of alumina. In contrary to the results reported by Zhen et al. coarser microstructure had a lower activation energy in the present work.[6] The grain growth experiments were done in argon which has some ppm level of oxygen and can diffuse into the material at high temperature. The stress exponents are all in the range of 2.5 – 3 and does not differ hugely with the orientation or grain size.

6.1.4. POST CREEP MICROSTRUCTURAL INVESTIGATION

The post-deformation micrographs of TSCFxy and TSCFzx are shown in Fig.6.8. The electron back scattered diffraction images provide insight of how the grain deformed or fractured.

TSCFxy was loaded face-on and TSCFzx was loaded edge-on with respect to basal plane orientation. TSCFxy simply resulted in fracture of basal plane and fragmentation of larger grains into smaller grains. Please note the clusters of grains with same orientation in Fig.6.8.b. It can be assumed that the cluster was a single grain before creep deformation and after creep at 1300 °C, 80 MPa, the grains with favorable orientations fractured into smaller grains. In case of TSCFzx, complete folding of grains basal texture has occurred, this can be seen in Fig.6.8.d where some grains with basal texture are seen as compared to Fig.6.8.b where grains with basal texture are not present. To better understand the phenomena and mechanism involved during the creep of TSCFxy, a fractured surface of a post-creep samples was analyzed.

Fig.6.9 shows the fractured surface features which confirm that creep of fine grained

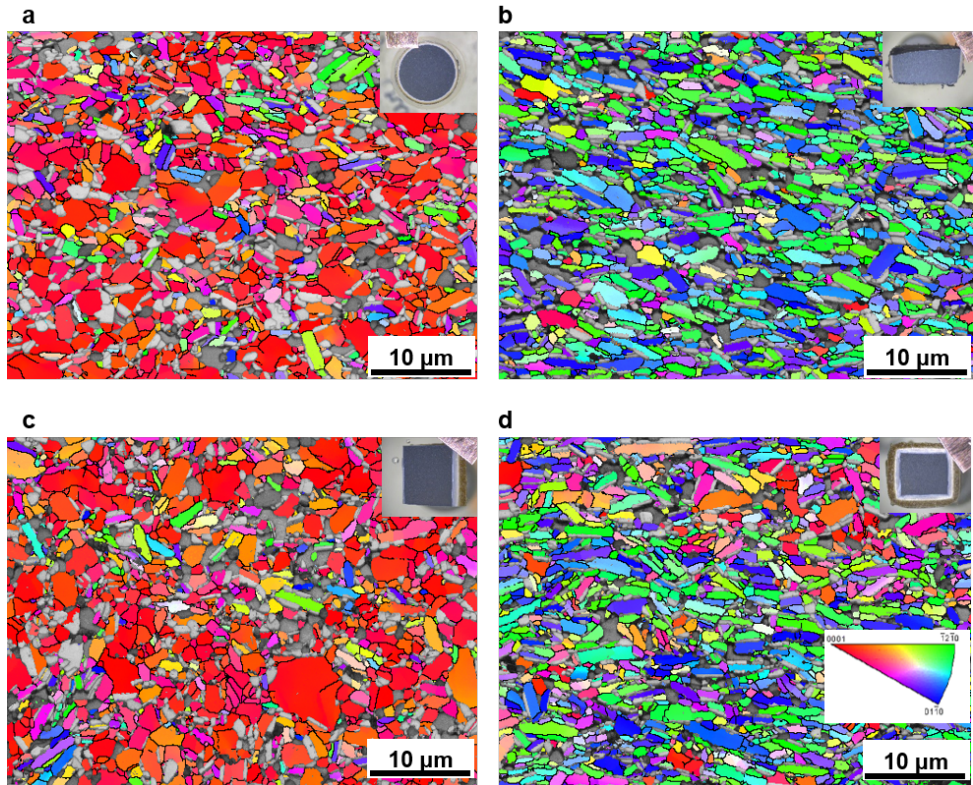


Figure 6.8: Orientation map of post creep textured Ti_3SiC_2 ceramics. **a** top and **b** side surface TSCFxy, **c** top and **d** side face of TSCFyz.

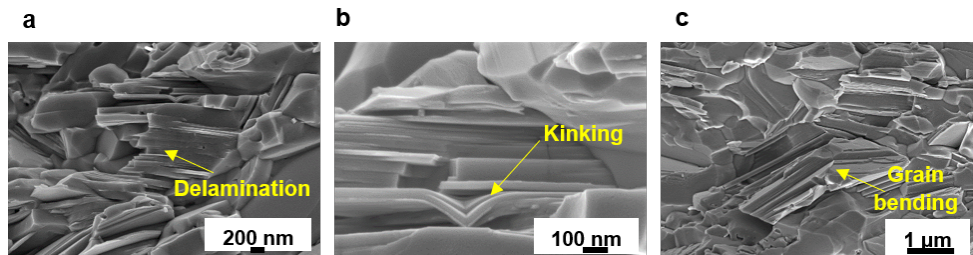


Figure 6.9: SEM micrographs of fractured surface of crept sample of fine grained Ti_3SiC_2 (TSCFxy) showing **a** delamination, **b** kinking and **c** grain bending.

Ti_3SiC_2 involved delamination, limited kinking and grain bending. Whether these are the main mechanism contributing to the deformation during creep has still not been clear. Basal slip and dislocations along the basal slip plane are the only operating slip plane in MAX phases and hence this cannot be ignored and might be the main contributor

for deformation as reported by Zhen et al.[6] A transmission electron microscopy study was done obtaining a lamella from the post creep sample of TSCFxy. Fig.6.10.a shows an overview of the lamella with grains of different phases at low magnification. The density of dislocation across the different grains shown in Fig.6.10.a was inhomogeneous. Fig.6.10.b shows the phase distribution in the lamella under investigation. Some grains did not have any dislocation at all and some grains had a high density of dislocations. As Ti_3SiC_2 is known to have only perfect dislocations lying the basal plane, a transmission kikuchi diffraction (TKD) was obtained and shown in Fig.6.10.c.[5, 8] The blue and green colored grains in Fig.6.10.c represents pyramidal and prismatic orientation respectively. There were no dislocations seen in the blue and green color-coded grains. However, the pink colored grains, which represent near basal orientation shows dislocation arrays.

Fig.6.10.d shows a low angle grain boundary (LAGB) with dislocation pile-up along it, the dislocation glide along the basal plane is the most favorable.[9] There are shear bands observed in grains oriented in a non-basal manner (Fig.6.7.e). It is noteworthy that shear bands and dislocations are present independent of each other in separate grains. The deformation of grains by basal slip in a favorable orientation is accommodated by mechanisms like shear banding in non-basal oriented grains. Fig.6.10.f shows the interaction of dislocations. The main creep mechanism can be concluded as the dislocation creep with deformation accommodating phenomena in non-basal orientated grains with respect to the compression axis in creep. The LAGB can be seen as a kink boundary which is formed during the creep due to the dislocation glide along the basal plane. Further extensive microscopy at high resolution is required to understand the creep process of textured Ti_3SiC_2 in more detail.

6.2. CREEP OF SHORT SiC_F / Ti_3SiC_2 COMPOSITES

6.2.1. STEADY STATE CREEP OF FINE GRAINED SiC_F / Ti_3SiC_2 CMC

As TSCFxy had the least deformation in creep and had the highest creep resistance. This configuration was used for further CMC fabrication and comparison as a reference material for creep resistance. TSCDxy was also used for comparison with SiC_F reinforced Ti_3SiC_2 composites with duplex microstructure. Henceforth, TSCFxy and TSCDxy will be just referred as TSCF and TSCD respectively. Ti_3SiC_2 reinforced with 10 and 20 vol.% of chopped SiC fiber of 1 mm length was fabricated for creep investigations. TSCF-20 SiC_F was not used for creep testing because of the presence of macroscopic pores and the inhomogeneity in the dispersion, see Fig.5.19. TSCF-10 SiC_F and TSCD-10 SiC_F were subjected to creep testing from 1100-1300 °C under stress levels of 20-120 MPa. Fig.6.11 presents the strain vs. time graph for creep at 1100 °C. The addition of 10 vol.% of SiC_F did not result in any significant increase in the creep resistance of TSCF at 1100 °C, 40 MPa (Fig.6.11.a). The red curves in Fig.6.11.a are almost superimposable. This can be an indication that at this temperature-pressure combination, dislocation creep is the only contributing factor. This is not to misunderstand that there is a transition in creep mechanisms beyond this point. It is only that other deformation mechanisms apart from dislocation-based deformation are activated with the increase in temperature and pressure. The addition of similar content of SiC_F in TSCD resulted in a significant reduction of the deformation during creep. The duplex microstructure might have facilitated effi-

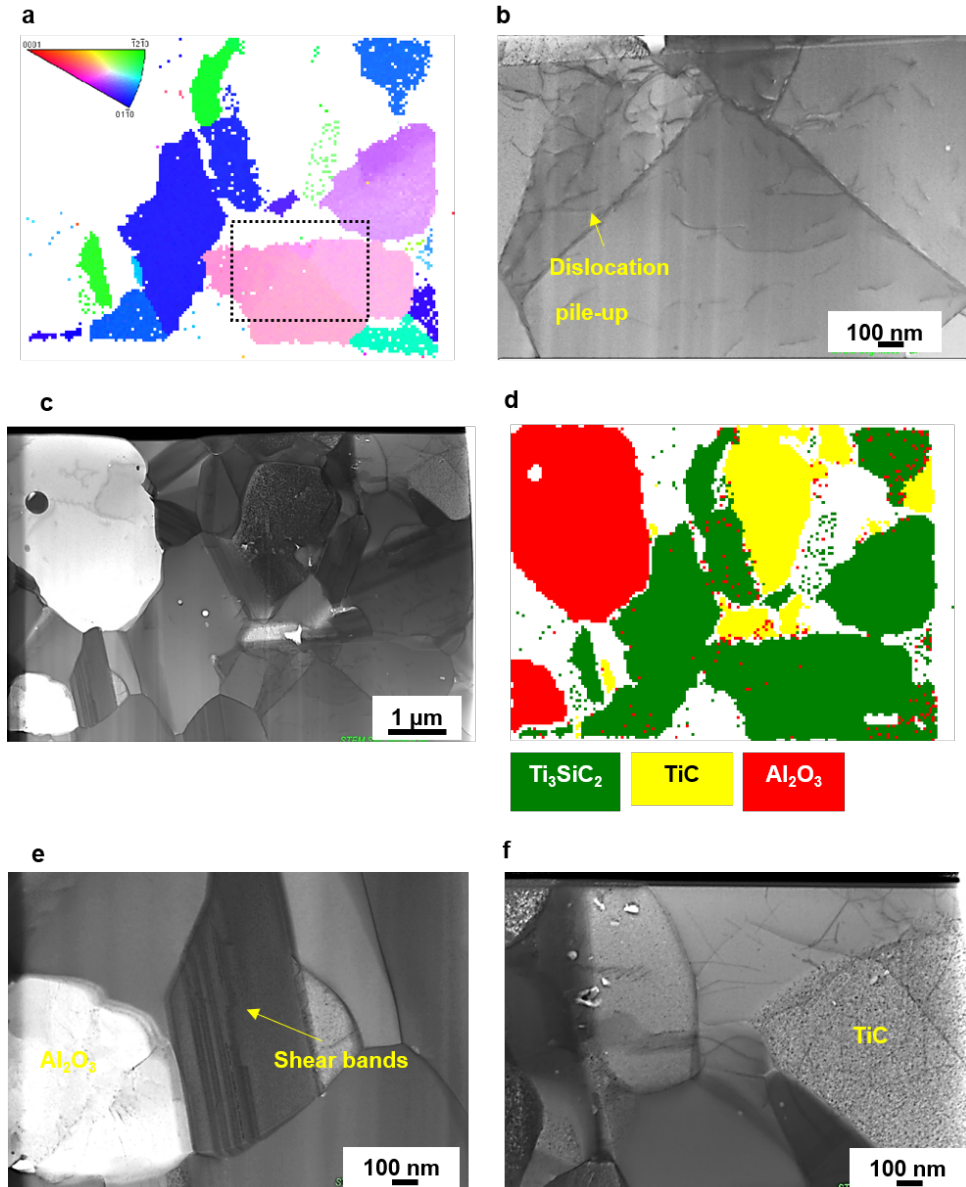


Figure 6.10: Transmission electron microscopy of post creep TSCFxy, **a** overview of the lamella, **b** phase map, **c** TKD, **d** showing dislocation arrays and pileups, **e** shear bands and **f** dislocation interaction.

cient load transfer to the SiC_f due to the presence of coarse grains which are more prone to bending. However, at a higher stress $1100\text{ }^\circ\text{C}$, 80 MPa , the effect of addition of SiC_f to TSCF is more pronounced. TSCF enters the steady state creep later as compared to

TSCF-10 SiC_f which enters the steady state creep regime much sooner.

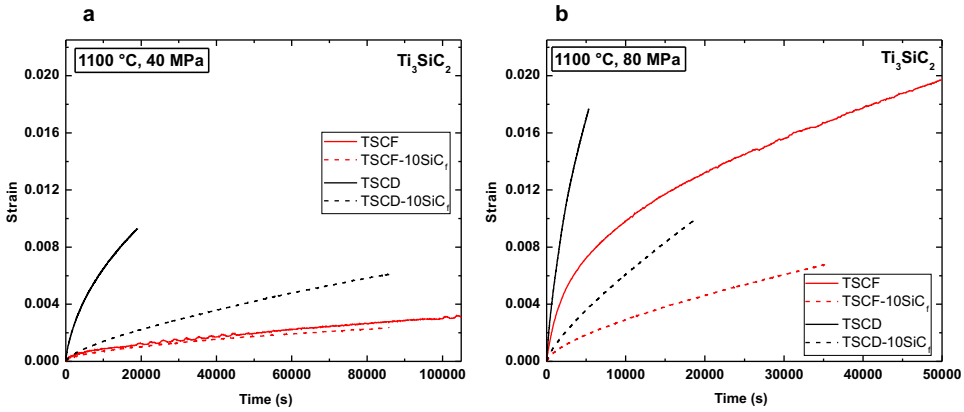


Figure 6.11: Compressive creep curves of SiC_f reinforced Ti_3SiC_2 at **a** 1100 °C, 40 MPa and **b** 80 MPa.

The deformation of TSCD-10 SiC_f is higher than TSCF at 1100 °C, 40 MPa whereas at 1100 °C, 80 MPa it is vice versa. It can be assumed that under a higher stress the deformation mechanism in TSCD-10 SiC_f is like that of TSCF and is not accompanied by delamination of grains or kinking of grains that may have taken place in TSCD. The presence of SiC_f may be responsible for ceasing of mechanism by which coarse grains of Ti_3SiC_2 are known to deform.[10–12]

6

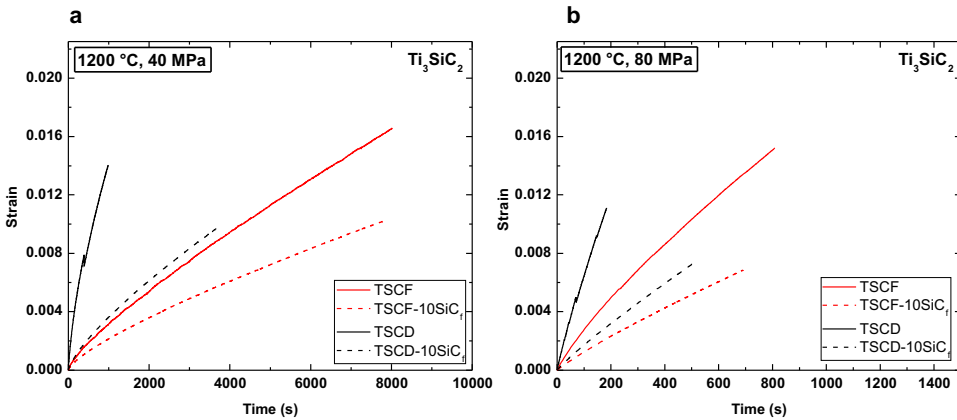


Figure 6.12: Compressive creep curves of SiC_f reinforced Ti_3SiC_2 at **a** 1200 °C, 40 MPa and **b** 80 MPa.

Fig. 6.12 shows the creep deformation curves of monolithic and SiC_f reinforced Ti_3SiC_2 at 1200 °C. The trend of deformation of monolithic fine grained and coarse grained Ti_3SiC_2 along with SiC_f reinforced composites are same as that at 1100 °C. At 1200 °C, the primary creep regime is not visible anymore. The effect of SiC_f addition in TSCF can be clearly seen at 1200 °C, 40 MPa (Fig. 6.12.a).

6.2.2. CREEP ACTIVATION ENERGY AND STRESS EXPONENT

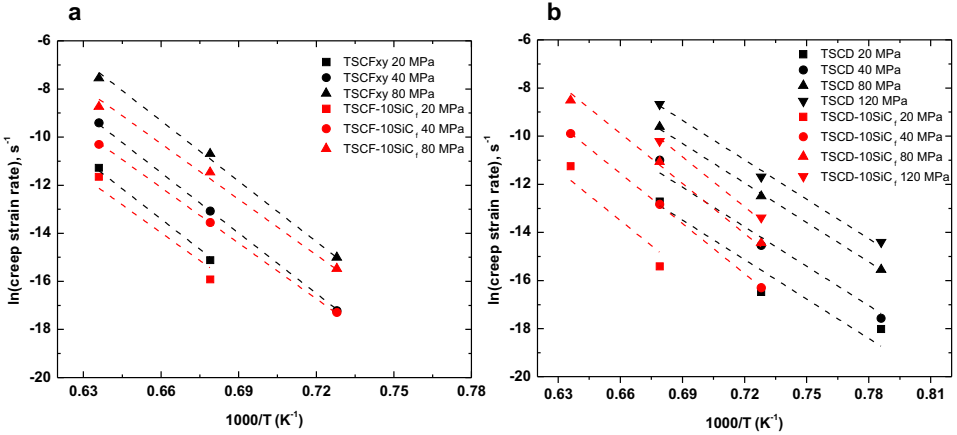


Figure 6.13: Ln-ln plot of min strain rate as a function of temperature for SiC_f reinforced **a** fine and **b** coarse Ti_3SiC_2 .

6

The effect of the addition of SiC_f makes the creep response of the composite near independent of the grain size of Ti_3SiC_2 suggesting the creep can be controlled with the addition of fibers. This shows that the presence of SiC_f in TSCD restricts the delamination of the coarse Ti_3SiC_2 grains which might have taken place in the specimen without any fiber. The activation energies and stress exponents for creep of SiC_f reinforced Ti_3SiC_2 as compared to monolithic Ti_3SiC_2 is shown in Table 6.3. The activation energy of TSCF-10 SiC_f is in the same range as that of TSCF. The rate controlling mechanism for creep is also assumed to be similar throughout the temperature range. TSCD-10 SiC_f has a visible increase in activation energy due to the presence of SiC_f . This can be the evidence of the effective suppression of creep deformation of TSCD as compared to TSCF with the addition of SiC_f . Fig.6.13.a shows that the creep rates of TSCF-10 SiC_f is nearly one order of magnitude lower than that of TSCF at 20 MPa whereas at higher stress the creep rates of both TSCF and TSCF-10 SiC_f seems to converge. Fig.6.13.b shows that the creep rate of TSCD-10 SiC_f is two orders of magnitude lower than that of TSCD. The slope of fitted straight lines are different for TSCD and TSCD-10 SiC_f and hence different corresponding activation energies. Fig.6.14 shows the ln-ln plot creep rates vs. the applied stress. The Ti_3SiC_2 grades irrespective of the grain size and the presence of SiC_f , have similar stress exponents over the whole temperature and stress range.

The creep rates as shown in Fig.6.14.a for TSCF and TSCF-10 SiC_f are similar over the temperature range. The addition of SiC_f resulted in a slight decrease of the creep rates. The decrease in creep rate is more pronounced at 1300 °C as compared to 1100 °C. Fig.6.14.b shows that the creep rates of TSCD-10 SiC_f is reduced by the addition of SiC_f even at a temperature of 1100 °C. This may be related to the plastic deformation of coarse grained Ti_3SiC_2 by kinking however fine grained Ti_3SiC_2 needs to be beyond the

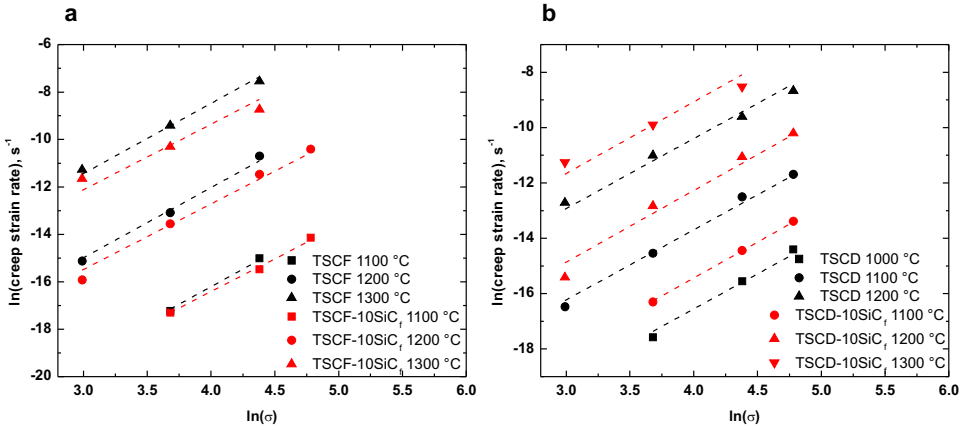


Figure 6.14: Ln-ln plot of min. strain rate as a function of applied compressive stress during the creep test of SiC_f reinforced **a** fine grained and **b** coarse grained Ti₃SiC₂.

Table 6.3: Summary of creep activation energy and stress exponents of SiC_f reinforced Ti₃SiC₂

Sample	Q (kJ/mol)	n
TSCF	696 ± 16	2.95 ± 0.13
TSCF-10SiC _f	641 ± 33	2.76 ± 0.18
TSCD	454 ± 29	2.53 ± 0.11
TSCD-10SiC _f	576 ± 33	2.59 ± 0.21

BPT temperature to demonstrate substantial plasticity.[11, 13] The creep of Hi-Nicalon SiC_f alone also has a contribution to the creep of the composite. The stress exponent of the creep of only Hi-Nicalon fibers lies in the range of 1.9-3 which is also the range for the fabricated composites in the present work.[14] The primary creep of Hi-Nicalon fiber is due to the grain boundary sliding of SiC grains and straightening of folded carbon crystals between SiC grains.[14] Since discontinuous SiC_f were added the creep in fibers may have been induced by shear stress from the matrix. A post-microstructural investigation after creep was done to better understand deformation mechanisms of the composites.

6.2.3. POST CREEP MICROSTRUCTURAL INVESTIGATION

The specimens under creep testing at 1300 °C, 80 MPa were polished to observe the deformation during creep. Fig.6.15.a and b shows the surface perpendicular and parallel to the applied stress respectively.

Fig.6.15.a shows multiple fractures in SiC_f perpendicular to the axis of the fiber which might be indication of load transfer from the matrix to the fiber. Since the fibers are a reinforcement in the microscale, the mechanisms leading to the increased creep resistance can also be in a microscale. Considering a homogenous composite, the critical percola-

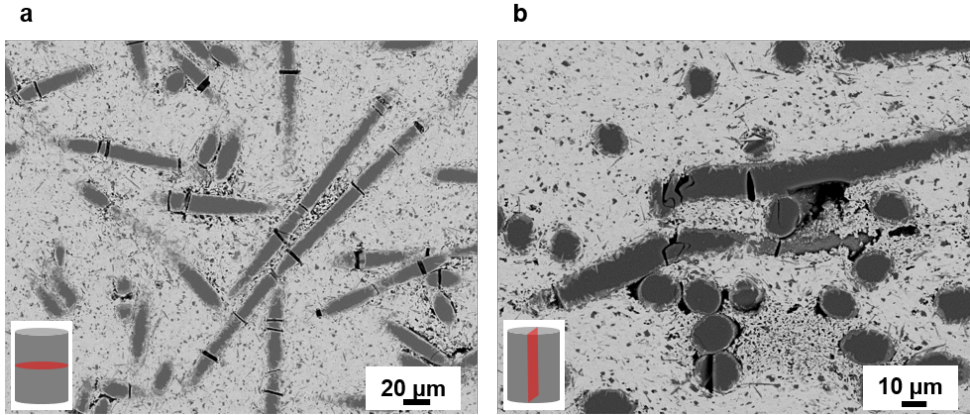


Figure 6.15: Post-creep (1300 °C, 80 MPa) microstructure of 10 vol.% SiC_f reinforced fine Ti₃SiC₂ showing the **a** perpendicular face and **b** parallel face.

tion limit volume fraction (Φ_{pcp}) of SiC_f can be calculated by the following relation:

$$\Phi_{pcp} = \frac{0.7}{(\text{aspectratio})} \quad (6.2)$$

Φ_{pcp} is the limit above which the whiskers can form an interconnected network. Since the materials are sintered under uniaxial pressure, there is a lack of three-dimensional connectivity (percolation) of SiC_f rather there are two dimensional arrays of SiC_f perpendicular to the uniaxial stress during sintering. Φ_{pcp} for such materials can be larger by a factor of two because expression (6.2) holds true for only randomly oriented whiskers.[15] Since the length and diameter of the SiC_f used is 1 mm and 10 μm respectively the aspect ratio can be considered as 100. Hence a volume fraction of 1.4 vol.% can result in the formation of a continuous percolated network. The point contacts of fibers are shown in Fig.6.15.b. Moreover, the fiber cracking due to other fibers compressing against each other is also visible. At high temperature (>1200 °C), the Ti₃SiC₂ matrix behaves like a plastic material and the rigid SiC_f act like a framework to resist any deformation due to the plasticity of Ti₃SiC₂ at high temperature.[13, 16]

Fig.6.16 shows the post-creep microstructure of TSCD-10SiC_f. As compared to TSCF-10SiC_f, the cracks in SiC_f are filled with matrix material in the case of TSCD-10SiC_f (Fig. 6.16.a). This confirms the visco-plastic creep of the matrix material (Ti₃SiC₂) into the cracks of SiC_f formed during the creep. Both Fig.6.16.a and b shows higher amount of porosity as compared to post-creep TSCF-10SiC_f microstructure in Fig.6.15. The porosity may arise due to the viscoplastic creep of the Ti₃SiC₂ matrix phase followed by viscoelastic creep of the SiC_f network.[17] The surrounding matrix accommodates the viscoelastic creep of SiC_f by plastic deformation. However, during the release of the stress the SiC_f inter-connected structure tries to re-gain its original configuration which is not possible in the case of Ti₃SiC₂ matrix. This unaccommodated partial reversal of creep deformation is manifested as pores which can be seen in Fig.6.16. Circular cracks are visible around the SiC_f in Fig.6.13.b, this maybe an indication of toughening by crack

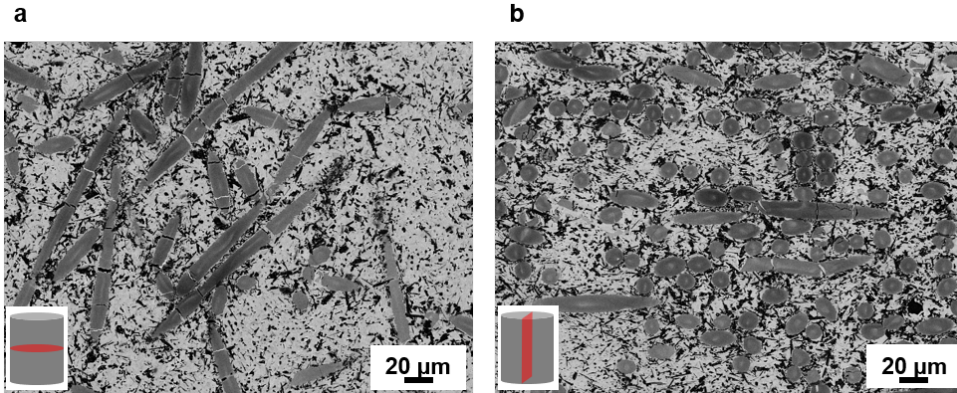


Figure 6.16: Post-creep (1300 °C, 80 MPa) microstructure of 10 vol.% SiC_f reinforced coarse Ti_3SiC_2 showing the **a** perpendicular face and **b** parallel face.

deviation and fiber debonding for TSCD-10 SiC_f . Further in-depth study is required to conclude the effect of the presence of SiC_f in coarse grained Ti_3SiC_2 on the strength of the composite. The number of iterations of the series is unknown because of multiple crack in a single fiber and the transition from viscoplastic to viscoelastic creep is not reflected in the strain vs time plot.

The lamella for TEM investigation was cut from an interface of a SiC_f and matrix to visualize the dislocations getting arrested at the interface. Surprisingly, dislocations could not be viewed in the Ti_3SiC_2 grains in the vicinity of the SiC_f . This can give an indication that the creep in TSC-10 SiC_f is not dislocation dominated rather the grain boundary sliding of β - SiC grains in the SiC_f . [18] It can be seen in Fig.6.17.a that the SiC grains grow in the interface and the Ti_3SiC_2 grains are arranged in a radial manner around the SiC_f . There are fragments of SiC which is shaved off the surface of SiC_f during creep and is visible as a very thin needle in Fig.6.17.b. The TKD of the Ti_3SiC_2 grains around the SiC_f shows that there is no preferential orientation. This may be due to the presence of SiC_f which absorbs all the stress and does not transmit it to the matrix as in the monolithic material during sintering. The deformed Ti_3SiC_2 grains are not being indexed for stress accumulation. The phase map is shown in Fig.6.17.d. The SiC_f was not indexed because of very small grains (5 nm) which is beyond the limit of the EBSD detector. An investigation far from the SiC_f vicinity might show dislocations but has not been done in the present case.

6.3. CREEP OF $\text{SiC}_w / \text{Ti}_3\text{SiC}_2$ COMPOSITES

6.3.1. STEADY STATE CREEP OF FINE GRAINED $\text{SiC}_w / \text{Ti}_3\text{SiC}_2$ CMC

The composites with fine grained Ti_3SiC_2 matrix and with reinforcement of SiC whiskers were considered for high temperature creep investigations. The creep curves of SiC_w reinforced Ti_3SiC_2 based CMCs for temperatures of 1200 and 1300 °C under 20 MPa are shown in Fig.6.18.a and b respectively. The creep curves [6] can be separated into two stages being representative of (i) primary creep regime with a rapidly decreasing creep

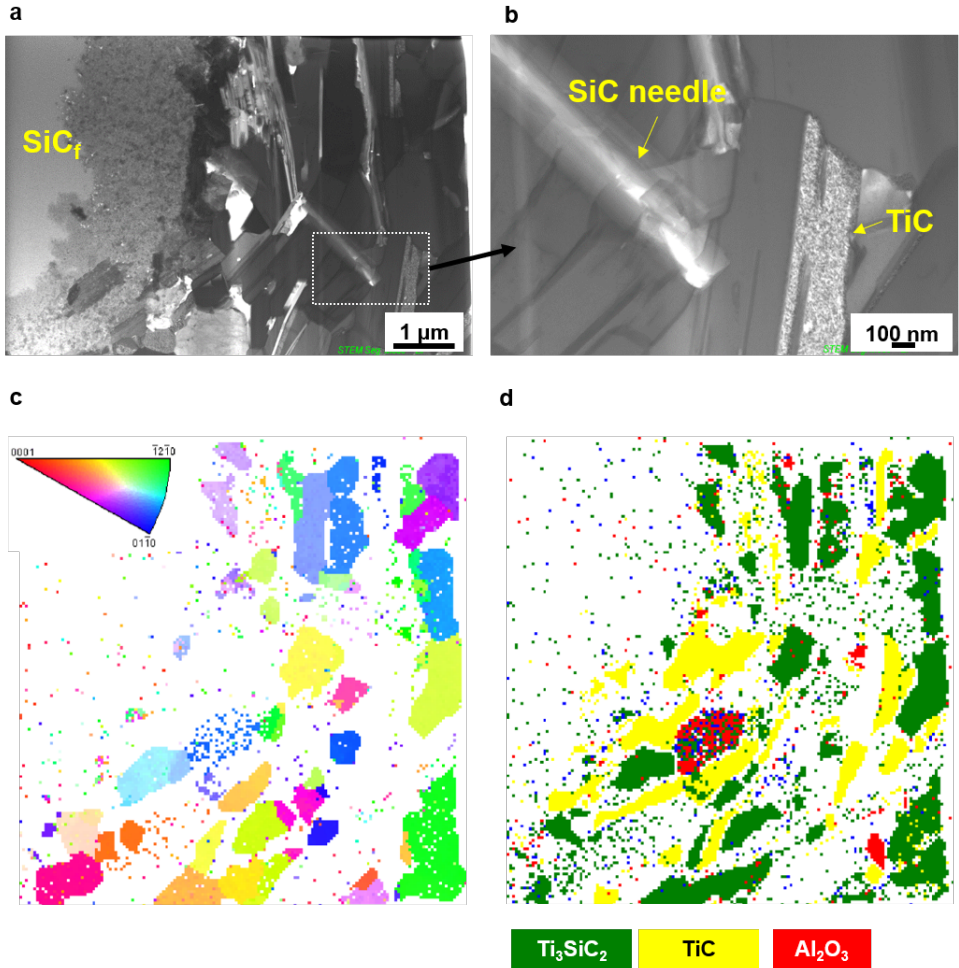


Figure 6.17: Transmission electron microscopy of post creep TSCFxy, **a** overview of the lamella, **b** region with curved basal planes, **c** TKD and **d** phase map.

rate also known as transient creep stage, (ii) secondary creep regime (steady state creep) with a constant creep rate, it is this regime which is of interest and is considered for evaluation of the creep properties of the CMCs fabricated in this work. The tests were aborted before reaching the tertiary creep regime. Fig.6.18.c and d show the creep of the the composites at 1200 and 1300 °C, 40 MPa. At a higher stress level, the primary creep regime of TSC and TSC-10SiC_w is not so clear whereas TSC-20SiC_w always has a primary creep regime before attaining the steady creep state.

Since the creep testing was performed in air, the surface was oxidized because of very long dwell time at high temperature (>1000 °C). However, the reduction in cross-section area is not significant and is same for all the CMC with different SiC_w content. Hence,

the effect of oxide scale ($\approx 200 \mu\text{m}$) on the evaluation of creep data have been neglected. Moreover, the CMCs with different SiC_w content being tested for compressive creep undergo similar oxidation and hence the effect of oxidation on creep can be ignored.[3, 6] To prove the effect of oxide scale on creep, a creep test was conducted in the cooling cycle for the sake of comparison. For example, the creep rate of TSC-10 SiC_w at 1200 °C and 40 MPa during heating from room temperature to 1300 °C was compared with the same creep conditions but during cooling from 1300 °C to room temperature. At 1300 °C the oxidation of the sample is more imminent and might influence the creep but the creep rates during heating and cooling were approximately the same. Moreover, the creep rate at 1300 °C is so high that the dwell time is very low, hence the oxidation of the surface of the sample is not severe.

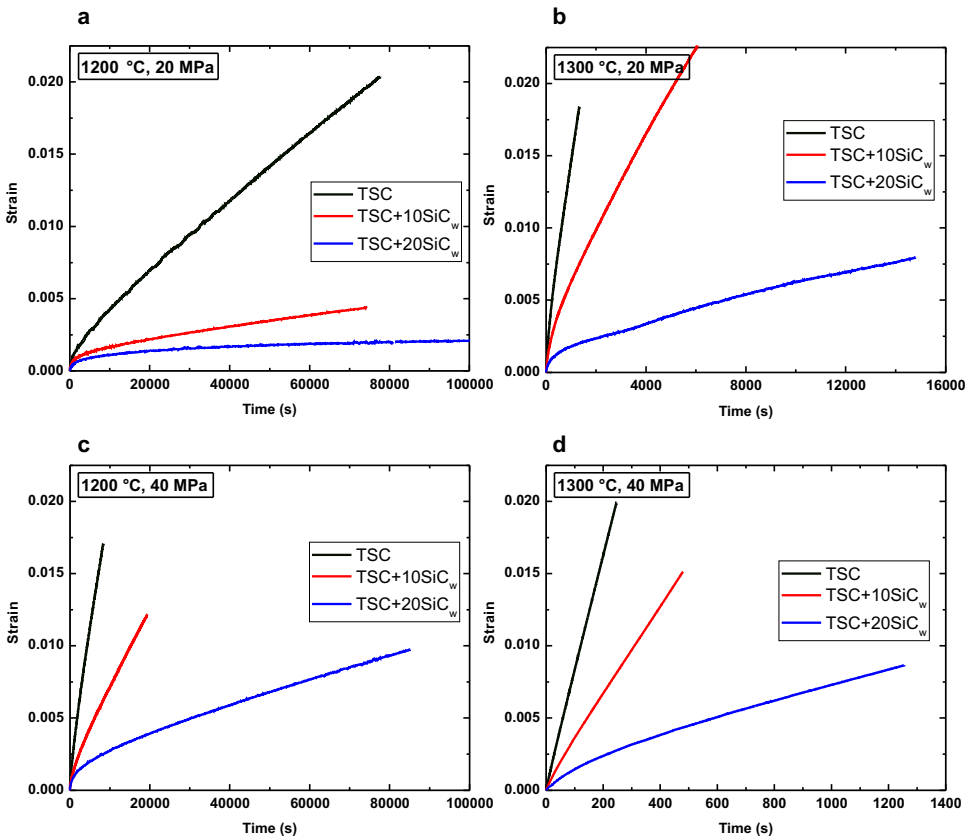


Figure 6.18: Compressive creep curves of $\text{SiC}_w / \text{Ti}_3\text{SiC}_2$ based CMCs at **a** 1200 °C, 20 MPa **b** 1300 °C, 20 MPa, **c** 1200 °C, 40 MPa and **d** 1300 °C, 40 MPa.

The addition of SiC_w has a profound effect on the creep resistance of Ti_3SiC_2 . TSC-20 SiC_w is much more resistant to deformation as compared to monolithic Ti_3SiC_2 or TSC-10 SiC_w . SiC_w reinforced Ti_3SiC_2 appears to enter the steady state creep regime much earlier than pure Ti_3SiC_2 . TSC-10 SiC_w and TSC-20 SiC_w have similar deformation

at 1200 and 20 MPa whereas TSC and TSC-10SiC_w have their creep curves close to each other at 1300 °C and 20 MPa. The deformation of TSC-10SiC_w is not intermediate to that of TSC and TSC-20SiC_w and hence the addition of SiC_w leads to a non-linear effect on the increase of creep resistance, being an indication of different activation energies and/or stress exponents as will be discussed further.

6.3.2. CREEP ACTIVATION ENERGY AND STRESS EXPONENT

Fig.6.19 presents Arrhenius plots of the steady state creep rate versus the reciprocal absolute temperature for different applied stresses. Regression analysis of the data was carried out via a global fit of all data using the software Origin to obtain the activation energies for the considered temperature range of 1100-1300 °C. A boot strap analysis was done by deleting individual data points and performing a fit of the rest of the data points to identify the specific data point which causes the increase in scatter of the activation energy.

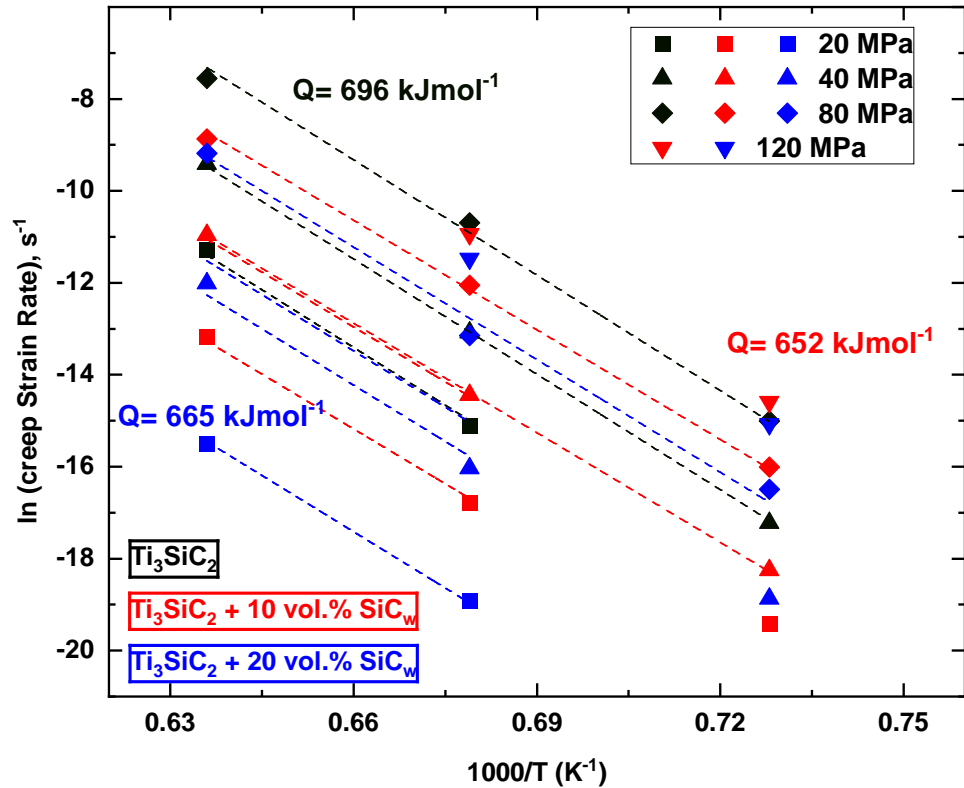


Figure 6.19: Ln plot of min strain rate as a function of temperature for Ti_3SiC_2 MAX phase-based CMCs with varying content of SiC_w for compressive creep measured at stress levels of 20-120 MPa.

It was found that the data points for TSC-10SiC_w at 1100 °C and 20 MPa corresponded to a creep of 1 μm/day and is probably still in primary creep regime, hence it was ex-

cluded for the calculation of activation energy, the same was done for TSC-20SiC_w at 1100 °C and 40 MPa. The calculated activation energies for the CMCs are summarized in Table 6.4. Upon the addition of SiC_w there is reduction in activation energy from 696 ± 16 kJ/mol for monolithic Ti₃SiC₂ to 665 ± 31 kJ/mol for TSC-20SiC_w with a similar value for the material with 10 vol.% whisker, so the addition of SiC_w results in ≈10% lower activation energy. A lower activation energy simply means a change in creep rate controlling process and has no strict implication towards the resistance to creep of a material, more indications to the creep mechanism is provided by the stress exponent values. However, the overall activation energies of three composition measured are similar and the rate controlling factor can be assumed to be almost the same as well.

Table 6.4: Summary of activation energies for creep of SiC_w reinforced Ti₃SiC₂ composites in compression

Sample ID	Q (kJ/mol)	Stress exponents		
		1100 °C	1200 °C	1300 °C
TSC	696 ± 16	3.0 ± 0.1		
TSC -10SiC _w	652 ± 10			
TSC-20SiC _w	665 ± 32	3.4	4.1	4.6 ± 0.3

Ln-ln plots of steady state creep as a function of applied stress for different temperatures are given in Fig.6.20. The stress exponents (n) were calculated by a linear regression analysis of the data. A global fit of the creep rates of TSC and TSC-10SiC_w was performed whereas for TSC-20SiC_w, individual fits were performed since the global fit with TSC-20SiC_w resulted in large scatter. The stress exponents of every composition are compared in Table 6.4 for the different temperatures. The increasing values of stress exponents of TSC-20SiC_w clearly indicate a transition of the creep mechanism for TSC-20SiC_w at different temperatures. With the addition of 10 vol.% of SiC_w addition there is a reduction in the creep rate by two orders of magnitude. There is no temperature dependency of the stress exponent for TSC and TSC-10SiC_w, hence the creep mechanism is expected to be same over the whole temperature range. On the other hand, TSC-20SiC_w has a strong temperature dependency and the stress exponent increases from 3.4 at 1100 °C to 4.6 at 1300 °C. Stress exponents of 3-5 indicate dislocation climb as the rate controlling mechanism. In addition, the deformation process also involves dislocation glide due to shear stress acting normal to the applied uniaxial stress during creep test.[19] The rate control mechanism of both monolithic and reinforced Ti₃SiC₂ MAX phases is similar due to similar activation energies but the exact rate controlling mechanism of the CMCs are not clear.

The addition of SiC_w appears to have a strong effect leading to a reduction of the high temperature creep deformation of Ti₃SiC₂. Since Ti₃SiC₂ is a pseudo ductile material where not all five slip systems are active for ductile deformation, the plastic deformation during creep might be attributed to the combination of basal slip and other phenomena like kink banding, delamination and shear band formation.[3, 10] As fine grains are not prone to delamination or kink banding, it can be assumed that dislocation creep maybe the only contributing factor to the creep deformation in the present case.[6] For temperatures < 1300 °C and low stresses (< 40 MPa), the presence of SiC_w reduces the creep, whereas the increase in the content of SiC_w (from 10 to 20 vol.%) has only a subtle de-

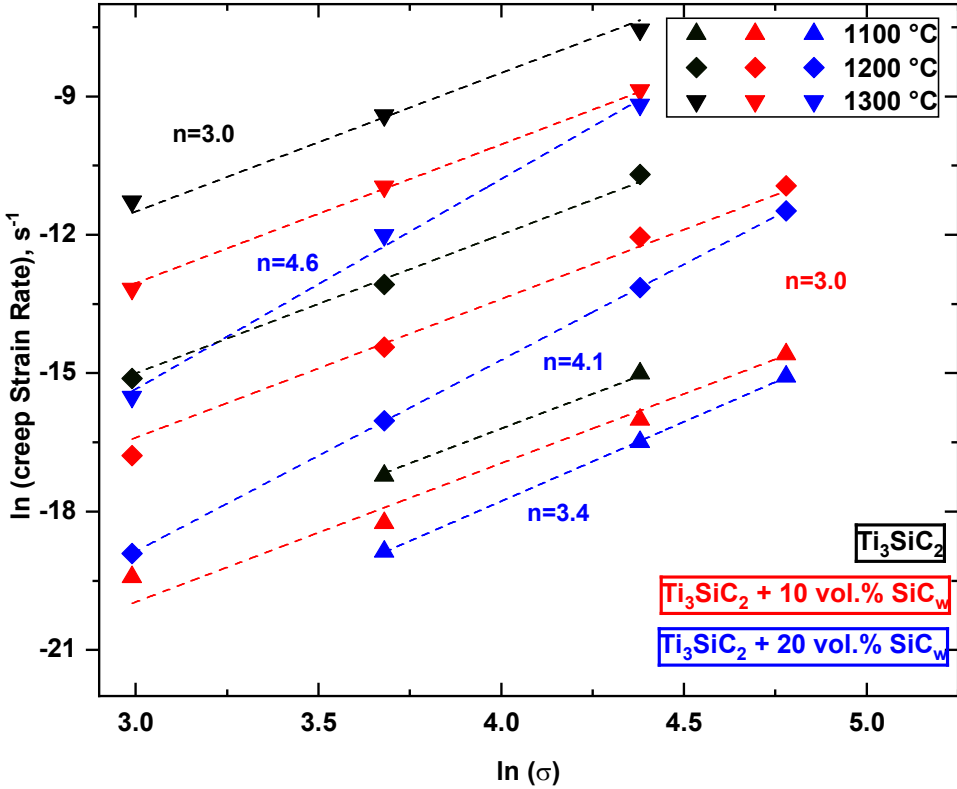


Figure 6.20: Ln-ln plot of min. strain rate as a function of applied compressive stress during the creep test for SiC_w reinforced Ti_3SiC_2 in the temperature range of 1100-1300 °C.

crease in the creep rates (Fig.6.20) suggesting the extra 10 vol.% SiC_w does not efficiently inhibit grain boundary sliding (GBS) rather, this might imply dislocation creep as one of the mechanisms in case of SiC_w reinforced Ti_3SiC_2 . The presence of rigid SiC_w may have restricted GBS of Ti_3SiC_2 partially or completely and hence resulted in a smaller deformation and creep rate.[20]

6.3.3. POST CREEP MICROSTRUCTURAL INVESTIGATION

Since the aspect ratio of the SiC_w is ≈ 10 , the critical percolation limit volume fraction (Φ_{pcp}) is around 7% as calculated by the relation 6.2. Φ_{pcp} is the limit above which the whiskers can form an interconnected network. Since there is a lack of three-dimensional connectivity (percolation) of SiC_w , Φ_{pcp} for such materials can be larger by a factor of two. Considering a Φ_{pcp} of 14%, the content of SiC_w used in the present study is both below (TSC-10 SiC_w) and above (TSC-20 SiC_w) percolation limit. The fact that the stress exponent of TSC-20 SiC_w becomes larger at high temperature indicates that the property for this material under this condition is not a general material representative rather representative for material under specific conditions only. The increasing stress expo-

nents of TSC-20 SiC_w provides the evidence of a change in creep mechanism over the temperature range of 1100-1300 °C, whereas for TSC and TSC-10 SiC_w the creep mechanism is same across the entire temperature range. At 1200 °C, 20 MPa, the addition of SiC_w may have restricted grain boundary sliding (GBS) and hence the lower deformation and creep rates of TSC-10 SiC_w and TSC-20 SiC_w . Although fine grained Ti_3SiC_2 has a brittle to plastic (BTP) transition at ≈ 1200 °C, the creep resistance is enhanced by the addition of SiC_w . [3] Since the addition of SiC_w has an increase in the creep resistance of Ti_3SiC_2 , grain boundary diffusion may have been hindered. At a temperature of >1200 °C, both lattice and grain boundary diffusion may have become significant as indicated by the BTP transition of Ti_3SiC_2 and hence pile-up of dislocations can be reduced efficiently and so the addition of SiC_w did not reduce the creep rates considerably at 1300 °C. At temperature above 1200 °C, where the Ti_3SiC_2 has a brittle to plastic transition, the creep of CMCs (specifically TSC-20 SiC_w) can be viewed as a sequential viscoplastic and viscoelastic deformation. The viscoplastic creep refers to the approach of SiC_w randomly oriented perpendicular to the creep direction. The matrix phase (Ti_3SiC_2) is squeezed out from between the in-plane SiC_w network. The hard SiC_w act as lines of stress concentration which cuts through the soft Ti_3SiC_2 grains. Fig.6.21 shows the perpendicular surface of post-creep microstructure of TSC-10 SiC_w . The large arrows in Fig.6.21.a show a grain with straight edge grain boundary because of SiC_w sinking into it and a cut Ti_3SiC_2 grain with SiC_w in the grain boundary. The distance between the randomly SiC_w is stochastic and the lack of three dimensional SiC_w network is due to the perpendicular alignment of SiC_w to the stress during sintering.

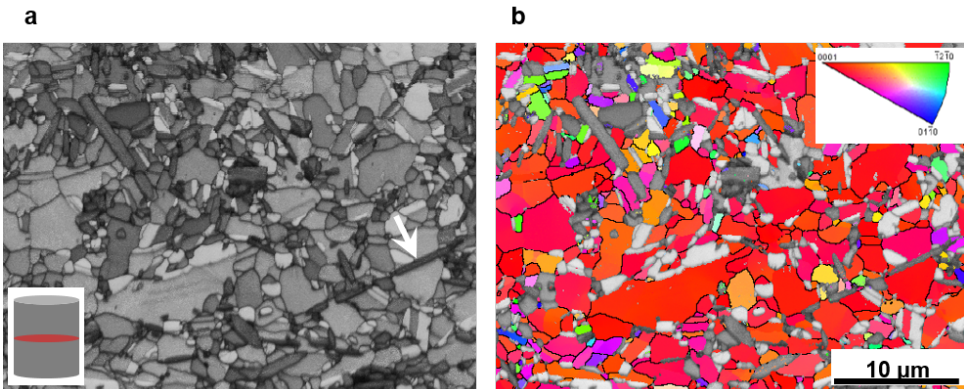


Figure 6.21: **a** Microstructure and **b** orientation map of post creep TSC-10 SiC_w . Note the SiC_w is cutting through Ti_3SiC_2 grain during creep at 1300 °C, 80 MPa.

For inter-connectivity there should be a random angular distribution of SiC_w whereas it is not in the present case. The viscoplastic deformation ceases once the SiC_w have point contacts within the perpendicularly oriented planes. The elastic bending of SiC_w with the deformation of Ti_3SiC_2 in the immediate vicinity of the SiC_w to accommodate the elastic deformation of SiC_w is referred to as viscoelastic creep. The viscoplastic deformation is only if $\Phi \leq \Phi_{pcp}$, hence this is valid for TSC-10 SiC_w , whereas in the case of

TSC-20SiC_w the SiC_w network is responsible for decreased creep rate. The probable absence of any viscoplastic creep above 1200 °C results in an increase in creep resistance of TSC-20SiC_w. Since TSC-20SiC_w has a SiC_w content higher than Φ_{pcp} , the SiC_w network inhibits GBS and the creep is governed by only diffusion, hence it has lower creep rates as compared to TSC and TSC-10SiC_w. However, beyond a certain stress (1300 °C, 80 MPa) the SiC_w network can no more oppose any resistance to GBS, hence both TSC-10SiC_w and TSC-20SiC_w have similar creep rates (Fig.6.20). In case of TSC-10SiC_w, GBS is evident by the change in the grain morphology and alignment of basal plane normal to the applied stress during creep (compare Fig.6.22.a and b).

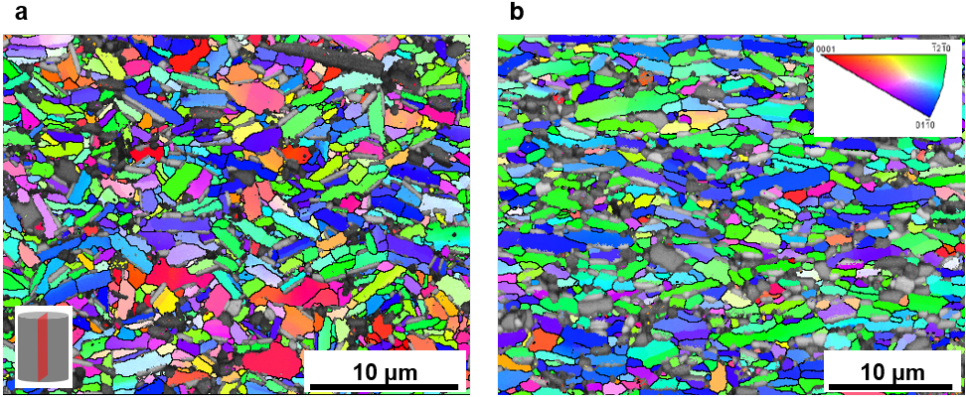


Figure 6.22: Orientation map of **a** as-sintered and **b** post-creep (1300 °C, 80 MPa) Ti₃SiC₂-10SiC_w.

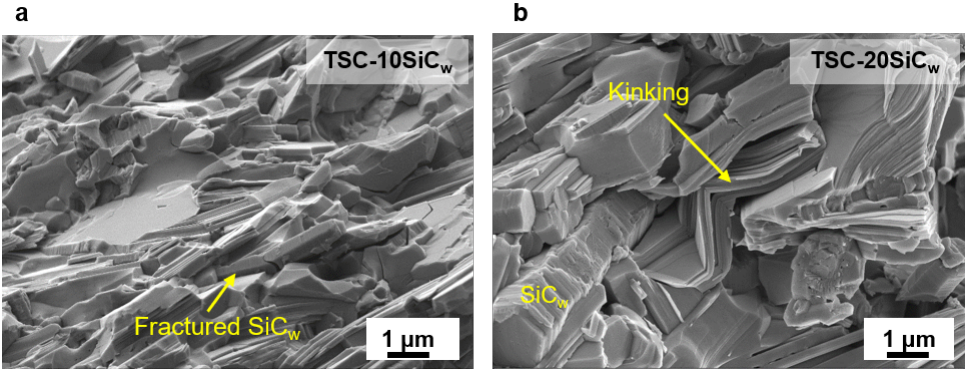


Figure 6.23: SEM micrographs of fracture surface of crept samples of **a** TSC-10SiC_w and **b** TSC-20SiC_w. Note that the crept samples were broken in the direction parallel to the creep stress.

The fractured surface of crept samples is shown in Fig.6.23. The TSC-10SiC_w sample shows fracture of SiC_w whereas CMC with higher SiC_w shows rather kinking and bending of grains (Fig.6.23.a and b). This may be due to the local constraints created by the presence of SiC_w which leads to the kinking of Ti₃SiC₂ grains. Transmission electron

microscopy of TSC-20 SiC_w reveals how the SiC_w increases the creep resistance of the composite.

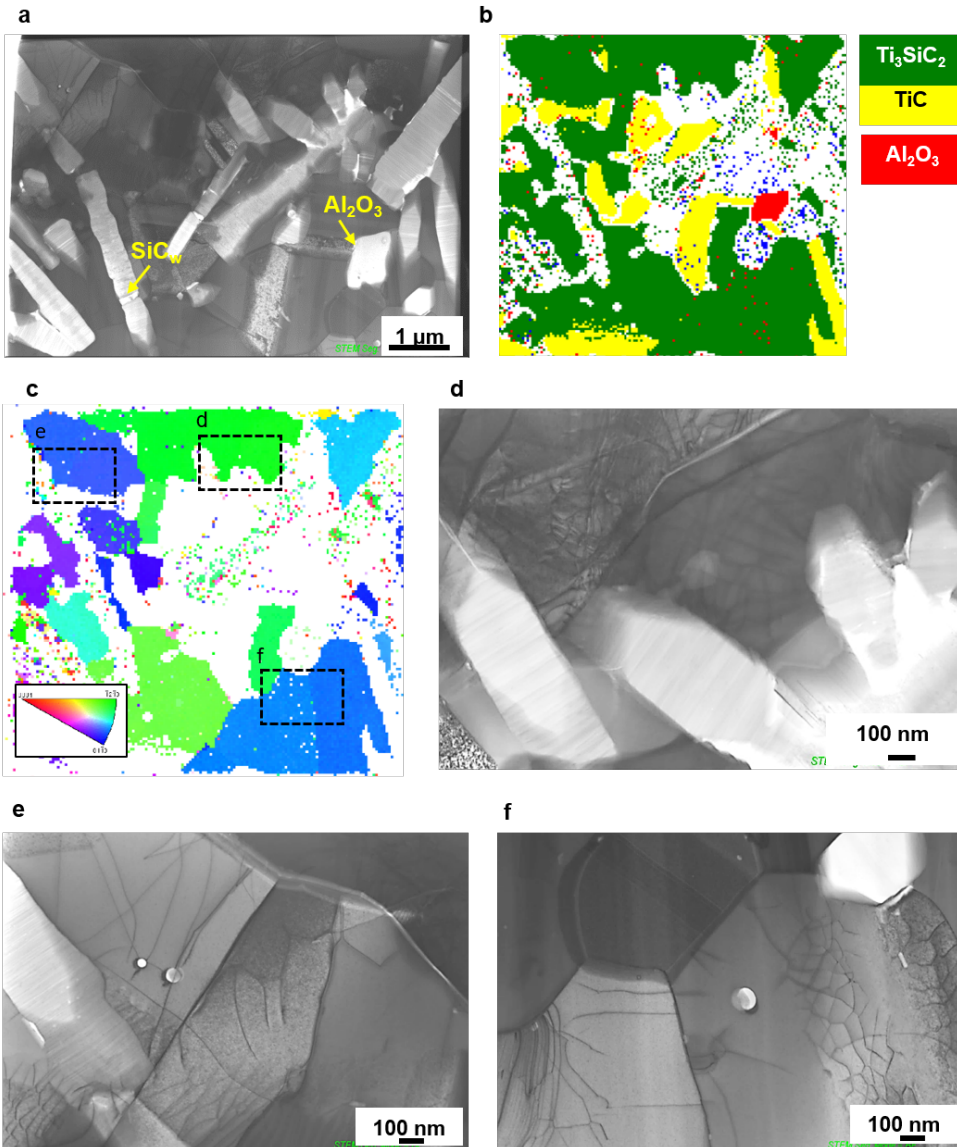


Figure 6.24: Transmission electron microscopy of post creep TSC-20 SiC_w , **a** overview of the lamella, **b** phase map, **c** TKD, **d** showing dislocation pileups, **e** shear bands and **f** dislocation interaction.

Fig.6.24.a shows the overview of the lamella obtained from post creep TSC-20 SiC_w . The phase with light contrast and high aspect ratio is SiC_w . The phase map in Fig.6.24.b

shows the presence of very small alumina grains. Fig.6.24.c shows the transmission kikuchi diffraction of Ti₃SiC₂ phase. There are no grains with basal orientation, however there are dislocations seen in the grains due to the deformation during creep. Fig.6.24.d shows a high density of dislocation in the vicinity of SiC_w. Fig.6.24.e shows that the dislocations are pinned at the interface of Ti₃SiC₂-SiC_w. Fig.6.24.f shows a network of dislocation which has resulted in the formation of dislocation cells indicating a dynamic recovery process during the creep at high temperature. Self-arrangement of the dislocations to the cell walls happen to obtain a high angle grain boundary which is more stable.

6.4. SUMMARY OF DIFFERENT REINFORCEMENTS ON THE CREEP OF Ti₃SiC₂

Fig.6.25 shows the comparison of the strain vs. time for monolithic Ti₃SiC₂, SiC_f and SiC_w reinforced Ti₃SiC₂ composites at 1200 and 1300 °C, 20 MPa. A similar level of reinforcement (10 vol.%) for both SiC_f and SiC_w was compared. The highest creep resistance was offered by the composite with SiC_w. The composite with SiC_f has a creep resistance intermediate to that of monolithic Ti₃SiC₂ and SiC_w reinforced Ti₃SiC₂. Table 6.5 summarizes the creep results of all the composites investigated in the present work.

Table 6.5: Summary of creep activation energy and stress exponents for Ti₃SiC₂ in compression with comparison to the previously investigated results

Material	Q (kJ.mol ⁻¹)	n	Proposed mechanism	Reference
TSC (compression)	537 ± 31	1.9	Dislocation	[6]
TSC (tension)	445 ± 10	1.5	Plastic deformation	[21]
TSCF _{xy}	696 ± 16	3	Dislocation	This work
TSCD _{xy}	454 ± 29	2.53	Dislocation, delamination	This work
TSC-10SiC _f	641 ± 33	2.8	Dislocation, viscoplastic - viscoelastic	This work
TSCD-10SiC _f	576 ± 33	2.6	viscoplastic-viscoelastic-viscoplastic	This work
TSC-10SiC _w	652 ± 10	3	Dislocation, GBS & viscoplastic	This work
TSC-20SiC _w	665 ± 32	3.4 - 4.6	Dislocation, GBS, viscoplastic & viscoelastic	This work

The SiC_f reinforced composite has a higher creep resistance than the pure material but a lower creep resistance as compared to SiC_w reinforced composites. This may be due to the high aspect ratio of SiC_f which allows for higher flexibility resulting in a higher deformation during creep. SiC_w on the other hand are single crystal entities which when forms a network is more rigid as compared to chopped SiC_f networks. At higher temperature (1300 °C) and pressure (80 MPa), the CMC with SiC_f resists deformation and is more resistant to creep as compared to the CMC with SiC_w. The transition of the trend between SiC_w and SiC_f containing Ti₃SiC₂ CMCs can be seen in Fig.6.25.e where the strain

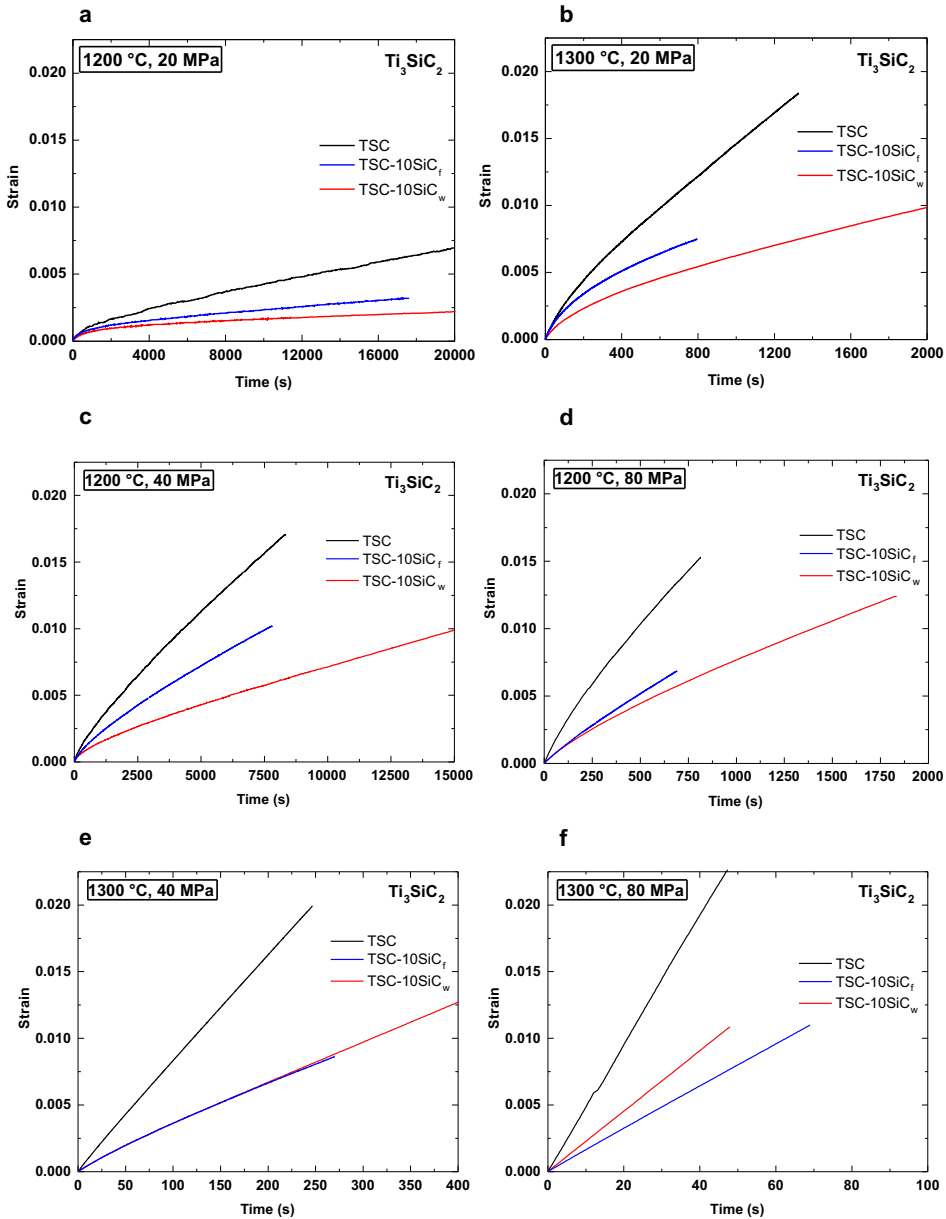


Figure 6.25: Compressive creep curves of SiC_f and SiC_w reinforced Ti_3SiC_2 based CMCs at **a** 1200 °C, 20 MPa, **b** 1300 °C, 20 MPa, **c** 1200 °C, 40 MPa, **d** 1200 °C, 80 MPa, **e** 1300 °C, 40 MPa and **f** 1300 °C, 80 MPa.

over time for both the CMCs are identical. This may be due to the extended network of SiC_f formed in the composite due to high aspect ratio resulting in an elastic bounce-back

resisting the deformation.

REFERENCES

- [1] A. Dash, J. Malzbender, K. Dash, M. Rasinski, R. Vaßen, O. Guillon, and J. Gonzalez-Julian, *Compressive creep of SiC whisker/Ti₃SiC₂ composites at high temperature in air*, Journal of the American Ceramic Society **103**, 5952 (2020).
- [2] A. Dash, J. Malzbender, R. Vaßen, O. Guillon, and J. Gonzalez-Julian, *Short SiC fiber/Ti₃SiC₂ MAX phase composites: Fabrication and creep evaluation*, Journal of the American Ceramic Society **103**, 7072 (2020).
- [3] M. Radovic, M. Barsoum, T. El-Raghy, J. Seidensticker, and S. Wiederhorn, *Tensile properties of Ti₃SiC₂ in the 25–1300 °C temperature range*, Acta materialia **48**, 453 (2000).
- [4] M. W. Barsoum, *MAX phases: properties of machinable ternary carbides and nitrides* (John Wiley & Sons, 2013).
- [5] M. Barsoum, L. Farber, and T. El-Raghy, *Dislocations, kink bands, and room-temperature plasticity of Ti₃SiC₂*, Metallurgical and Materials Transactions A **30**, 1727 (1999).
- [6] T. Zhen, M. Barsoum, S. Kalidindi, M. Radovic, Z. Sun, and T. El-Raghy, *Compressive creep of fine and coarse-grained Ti₃SiC₂ in air in the 1100–1300 °C temperature range*, Acta materialia **53**, 4963 (2005).
- [7] J. Pelleg, *Creep in ceramics*, in *Creep in Ceramics* (Springer, 2017) pp. 41–61.
- [8] B. Kooi, R. Poppen, N. Carvalho, J. T. M. De Hosson, and M. Barsoum, *Ti₃SiC₂: A damage tolerant ceramic studied with nano-indentations and transmission electron microscopy*, Acta Materialia **51**, 2859 (2003).
- [9] F. Barcelo, S. Doriot, T. Cozzika, M. Le Flem, J. Béchade, M. Radovic, and M. Barsoum, *Electron-backscattered diffraction and transmission electron microscopy study of post-creep Ti₃SiC₂*, Journal of alloys and compounds **488**, 181 (2009).
- [10] M. Radovic, M. Barsoum, T. El-Raghy, and S. Wiederhorn, *Tensile creep of coarse-grained Ti₃SiC₂ in the 1000–1200 °C temperature range*, Journal of Alloys and compounds **361**, 299 (2003).
- [11] T. El-Raghy, M. W. Barsoum, A. Zavaliangos, and S. R. Kalidindi, *Processing and mechanical properties of Ti₃SiC₂: II, effect of grain size and deformation temperature*, Journal of the American ceramic society **82**, 2855 (1999).
- [12] M. Barsoum, T. Zhen, S. Kalidindi, M. Radovic, and A. Murugaiah, *Fully reversible, dislocation-based compressive deformation of Ti₃SiC₂ to 1 GPa*, Nature Materials **2**, 107 (2003).
- [13] M. W. Barsoum and M. Radovic, *Elastic and mechanical properties of the MAX phases*, Annual review of materials research **41**, 195 (2011).

- [14] R. Bodet, X. Bourrat, J. Lamon, and R. Naslain, *Tensile creep behaviour of a silicon carbide-based fibre with a low oxygen content*, *Journal of materials science* **30**, 661 (1995).
- [15] D. Wilkinson and W. Pompe, *Creep and anelastic recovery of whisker-and platelet-reinforced ceramics*, *Acta materialia* **46**, 1357 (1998).
- [16] J.-F. Li, W. Pan, F. Sato, and R. Watanabe, *Mechanical properties of polycrystalline Ti_3SiC_2 at ambient and elevated temperatures*, *Acta Materialia* **49**, 937 (2001).
- [17] A. Kelly and K. Street, *Creep of discontinuous fibre composites II. Theory for the steady-state*, *Proceedings of the Royal Society of London. A. Mathematical and Physical Sciences* **328**, 283 (1972).
- [18] S. Zhu, M. Mizuno, Y. Nagano, Y. Kagawa, and H. Kaya, *Tensile creep behavior of a SiC-fiber/SiC composite at elevated temperatures*, *Composites science and technology* **57**, 1629 (1998).
- [19] W. R. Cannon and T. G. Langdon, *Creep of ceramics*, *Journal of materials science* **23**, 1 (1988).
- [20] A. De Arellano-Lopez, A. Dominguez-Rodriguez, and J. Routbort, *Microstructural constraints for creep in SiC-whisker-reinforced Al_2O_3* , *Acta materialia* **46**, 6361 (1998).
- [21] M. Radovic, M. Barsoum, T. El-Raghy, and S. Wiederhorn, *Tensile creep of fine grained (3–5 μm) Ti_3SiC_2 in the 1000–1200 °C temperature range*, *Acta materialia* **49**, 4103 (2001).

7

CONCLUSION

A novel method for the synthesis of MAX phases and other non-oxide ceramics was developed. The process was based on molten salt which enabled the reduction of the synthesis temperature also allowed the process to be carried out in an air furnace. The process was named as Molten Salt Shielded Synthesis/Sintering (MS³). KBr was used as the molten salt medium for enhanced diffusion of elements at high temperature. In addition, KBr was also used to create a gas tight cladding around the specimen which protects the sample from oxidation at a temperature below the melting point of the salt. Further, the sample was protected from oxidation due to the barrier of molten salt pool which cuts off the oxygen supply between the ambient atmosphere inside the air furnace and the material being processed. The property of KBr to be pressed to very high density at room temperature was exploited to protect the material from oxidation with dense encapsulation of KBr around it. Various non-oxide ceramic powders like TiC, Ti₃SiC₂, Ti₂AlN, Ti₂AlC, Cr₂AlC, MoAlB and Cr₂AlB₂ were synthesized in air with this process for the proof of concept. The advantage of using the MS³ is that there is no requirement of grinding or milling step after the synthesis step. Loose micrometric powders were obtained by just washing the salt content with water. In addition, oxidation prone metals like titanium was also processed with the MS³ process. Dense and porous titanium were fabricated in air for the first time. Thermal analysis of the encapsulated specimen-salt bath assembly revealed the inhibition of oxidation after the melting point of the salt. Oxygen analysis of the processed products yielded comparable oxygen wt.% as to when the material is processed in argon or vacuum.

Ti₃SiC₂ was synthesized by the MS³ process at 1250 °C for 1 h. The addition of 0.1 mol.% of Al to the reaction mixture of Ti/Si/C results in the increase of the phase purity of Ti₃SiC₂ to 97 wt.%. The addition of Al was necessary for enhancing the purity of Ti₃SiC₂. A reaction mechanism leading to the formation of Ti₃SiC₂ phase was proposed. XRD analysis reveals that there was no Al in the crystal lattice of Ti₃SiC₂ and the lattice parameter of Ti₃SiC₂ is the same irrespective of the content of Al. The addition of Al assisted the reaction by forming TiAl₃ as intermediate compound by reducing TiO₂ which might have formed due to oxidation at low temperatures. The formation of alumina in

the interface of Ti_3SiC_2 and KBr also impedes the out-diffusion of Si into the KBr salt thereby maintaining the stoichiometric ratios of the constituent reactants. Clusters of Si were seen in the molten salt bath when Al was not used. Nano-metric Ti_3SiC_2 particles were prepared by milling the synthesized powders.

Monolithic Ti_3SiC_2 and its composites were sintered in spark plasma sintering furnace at 1250 °C with a pressure of 80 MPa in a graphite die and vacuum. The sintered Ti_3SiC_2 had a higher content of TiC as compared to the starting powder. This can be due to the de-intercalation of Si from the MAX phase structure due to high vacuum during sintering. The wt.% of TiC and Al_2O_3 is 8.8 wt.% and 4.6 wt.% by Rietveld analysis, respectively, in the SPS sintered Ti_3SiC_2 . The presence of Al_2O_3 is due to the use of Al as a reaction additive during the molten salt synthesis of Ti_3SiC_2 . The average grain size of the SPS sintered Ti_3SiC_2 was nearly 1 μm . In addition, the sintered Ti_3SiC_2 had a high basal texture which suggests that the basal plane is aligned perpendicular to the applied external stress for sintering. A grain growth study by annealing the already sintered Ti_3SiC_2 showed that the grains do not prefer to grow in the 0001 direction rather in other directions. A duplex microstructure of Ti_3SiC_2 was obtained with very large grains of the size of 500 μm in the matrix of fine grains (1 μm). As the material was textured, the large grains also grew in an oriented manner. The CMCs were sintered by mixing 0, 10, 20 vol.% of SiC fibers and SiC whiskers separately for two set of experiments. The grain size of the matrix was not affected by the presence of SiC_f or SiC_w . The composites with reinforcement were fully dense with the grain size equivalent to the monolithic sintered material. SiC_f and SiC_w were aligned in a plane perpendicular to the applied load. The effect of macro-scale and micro-scale reinforcement on the high temperature creep response was studied.

The creep response of textured monolithic Ti_3SiC_2 was investigated in the temperature range of 1000-1300 °C with a constant load of 20-120 MPa. Since the sintered Ti_3SiC_2 was textured, different configurations of specimen were cut out from the sintered block creep testing. In one set of experiments, the basal plane was loaded edge-on and in other set of experiment, the basal plane was loaded face-on. Similar experiments were done for Ti_3SiC_2 with duplex microstructure. The activation energy for the specimens loaded with basal plane face-on and fine microstructure was found to be highest with a value of 696 ± 16 kJ/mol. The specimen with duplex microstructure had a lower creep activation energy of 454 ± 29 kJ/mol. This is contradiction to the activation energy trend reported for fine and coarse grained Ti_3SiC_2 in the literature. The discrepancy might be due to the high degree of texture in the specimen fabricated in the current work. Similar stress exponents of 2.5-3 for all configuration of textured Ti_3SiC_2 suggested the same creep mechanism. TEM results reveal the presence of dislocations and shear banding for fine grained texture Ti_3SiC_2 . SiC_f reinforced Ti_3SiC_2 had a creep rate which is one order of magnitude lower than that of pure Ti_3SiC_2 . $\text{SiC}_f / \text{Ti}_3\text{SiC}_2$ with duplex microstructure had a creep resistance of two magnitude lower than that of monolithic Ti_3SiC_2 counterpart. SiC_f absorbed the mechanical stress and fragmented into smaller segments during the creep. The creep rates were a function of the SiC_w content and decreased with increasing SiC_w . The stress exponent of TSC and TSC-10 SiC_w were constant over the range of temperatures but that of TSC-20 SiC_w increased with increasing temperature from 3.4 at 1100 °C to 4.6 at 1300 °C. SiC_w may have inhibited the grain boundary sliding by anchoring grains together, a higher content of SiC_w in Ti_3SiC_2 might be responsible for creating

a network of particles resulting in higher creep resistance. A combination of viscoplastic and viscoelastic creep can be operating during the creep of TSC-20SiC_w. The highest creep resistance was offered by the composite with SiC_w. The composite with SiC_f has a creep resistance intermediate to that of monolithic Ti₃SiC₂ and SiC_w reinforced Ti₃SiC₂.

CURRICULUM VITÆ

Apurv DASH

25-02-1991 Born in Rourkela, India.

EDUCATION

- 1996–2009 Primary-Secondary School
Ispat English Medium School, Rourkela, India
- 2009–2013 Bachelors of Technology in Ceramic Engineering
National Institute of Technology (NIT), Rourkela, India
Thesis: Synthesis of Yttrium Aluminium Garnet (YAG) nanopowders for transparent ceramic applications
Promotor: Prof. dr. D. Sarkar
- 2014–2016 Master of Science in Materials Engineering
Katholieke Universiteit Leuven (KU Leuven), Belgium
Thesis: Processing and properties of transparent zirconia ceramics
Promotor: Prof. dr. J. Vleugels
- 2016–2019 Ph.D. in Material Science
Forschungszentrum Jülich GmbH
Rheinisch-Westfälische Technische Hochschule (RWTH), Aachen, Germany
Thesis: Processing and creep resistance of short SiC fiber containing Ti_3SiC_2 MAX phase composites
Promotor: Prof. dr. J. Gonzalez-Julian

LIST OF PUBLICATIONS

5. **A. Dash**, J. Malzbender, M. Rasinski, R. Vaßen, O. Guillon, J. Gonzalez-Julian, *Effect of texture and grain size on the creep of Ti_3SiC_2 MAX phase ceramics*, submitted to Acta Materialia.
4. **A. Dash**, J. Malzbender, R. Vaßen, O. Guillon, J. Gonzalez-Julian, *Short SiC fiber/ Ti_3SiC_2 MAX phase composites: Fabrication and creep evaluation*, *Journal of the American Ceramic Society* **103**, 7072 (2020).
3. **A. Dash**, J. Malzbender, R. Vaßen, O. Guillon, J. Gonzalez-Julian, *Compressive creep of SiC whisker/ Ti_3SiC_2 composites at high temperature in air*, *Journal of the American Ceramic Society* **103**, 5952 (2020).
2. **A. Dash**, Y. J. Sohn, R. Vaßen, O. Guillon, J. Gonzalez-Julian, *Synthesis of Ti_3SiC_2 MAX phase powder by a molten salt shielded synthesis (MS^3) method in air*, *Journal of the European Ceramic Society* **39**, 3651 (2019).
1. **A. Dash**, R. Vaßen, O. Guillon, J. Gonzalez-Julian, *Molten salt shielded synthesis of oxidation prone materials in air*, *Nature Materials* **18**, 465 (2019).

Band / Volume 531

Einflüsse von Klimavariabilität und -wandel auf Ausbau und Erzeugung im Europäischen Stromsystem

F. P. Gotzens (2021), XXIII, 231 pp

ISBN: 978-3-95806-530-7

Band / Volume 532

Weltweite Infrastruktur zur Wasserstoffbereitstellung auf Basis erneuerbarer Energien

P.-M. Heuser (2021), VII, 231 pp

ISBN: 978-3-95806-531-4

Band / Volume 533

Mechanische Eigenschaften von katalysatorbeschichteten Membranen für die Polymer-Elektrolyt-Membran Elektrolyse

E. Borgardt (2021), viii, 181 pp

ISBN: 978-3-95806-533-8

Band / Volume 534

Techno-economic Assessment of Hybrid Post-combustion Carbon Capture Systems in Coal-fired Power Plants and Steel Plants

Y. Wang (2021), IV, xx, 230 pp

ISBN: 978-3-95806-545-1

Band / Volume 535

Wissenschaftliche Begleitstudie der Wasserstoff Roadmap Nordrhein-Westfalen

S. Cerniauskas, P. Markewitz, J. Linßen, F. Kullmann, T. Groß, P. Lopion, P.-M. Heuser, T. Grube, M. Robinius und D. Stolten (2021), IV, 89 pp

ISBN: 978-3-95806-547-5

Band / Volume 536

High-Resolution Photocurrent Mapping of Thin-Film Silicon Solar Cells Using Scanning Near-Field Optical Microscopy

Z. Cao (2021), xiii, 148 pp

ISBN: 978-3-95806-548-2

Band / Volume 537

Kompressionseigenschaften der Gasdiffusionslage einer Hochtemperatur-Polymerelektrolyt-Brennstoffzelle

E. Hoppe (2021), viii, 153 pp

ISBN: 978-3-95806-549-9

Band / Volume 538

Transparent Passivating Contact for Crystalline Silicon Solar Cells

M. Köhler (2021), 186 pp

ISBN: 978-3-95806-550-5

Band / Volume 539

Distribution of trace gases with adverse effects on fuel cells

D. Klemp, R. Wegener, R. Dubus, L. Karadurmus, N. Kille, Z. Tan (2021),
160 pp

ISBN: 978-3-95806-551-2

Band / Volume 540

**Cyclotron Irradiation on Tungsten & Co-relation of Thermo-Mechanical
Properties to Displacement and Transmutation Damage**

R. Rayaprolu (2021), xiv, 211 pp

ISBN: 978-3-95806-552-9

Band / Volume 541

**Smart Energy in Haushalten:
Technologien, Geschäftsmodelle, Akzeptanz und Wirtschaftlichkeit**

H. Shamon, T. Rehm, B. Helgeson, F. Große-Kreul, M. Gleue, U. Paukstadt,
G. Aniello, T. Schneiders, C. Frings, A. Reichmann, A. Löschel, T. Gollhardt,
W. Kuckshinrichs, K. Gruber, P. Overath, C. Baedeker, F. Chasin, K. Witte,
J. Becker

(2021), VI, 142 pp

ISBN: 978-3-95806-554-3

Band / Volume 542

Deployment Status of Fuel Cells in Road Transport: 2021 Update

R. C. Samsun, L. Antoni, M. Rex, D. Stolten (2021), 37 pp

ISBN: 978-3-95806-556-7

Band / Volume 543

**Processing and creep resistance of short SiC fiber
containing Ti_3SiC_2 MAX phase composites**

A. Dash (2021), vii, 125 pp

ISBN: 978-3-95806-558-1

Weitere **Schriften des Verlags im Forschungszentrum Jülich** unter
<http://www.zwb1.fz-juelich.de/verlagextern1/index.asp>

Energie & Umwelt / Energy & Environment
Band / Volume 543
ISBN 978-3-95806-558-1